9-5-2013

Mid-Wave and Long-Wave Single Uni-polar Barrier Infrared Detectors Based on Antimonide Material Systems

Stephen Myers

Stephen Myers

Candidate

Nanoscience and Microsystems

Department

This dissertation is approved, and it is acceptable in quality and form for publication:

Approved by the Dissertation Committee:

Sanjay Krishna, Ph.D. , UNM, ECE/NSMS , Chairperson

Luke Lester, Ph.D., UNM, ECE

Sang Han, Ph.D., UNM, ChNE/NSMS

John Klem, Ph.D., SNL

Mid-Wave and Long-Wave Single Uni-polar Barrier Infrared Detectors Based on Antimonide Material Systems

by

Stephen A. Myers

B.S., Engineering Physics, Tarleton State University, 2007
M.S., Electrical and Computer Engineering, University of New Mexico, 2012

DISSERTATION

Submitted in Partial Fulfillment of the
Requirements for the Degree of

Doctor of Philosophy
Nanoscience and Microsystems

The University of New Mexico

Albuquerque, New Mexico

July, 2013

Dedication

To my parents, Richard and Patsy Myers, the teachers who commenced my adventure in education.

"The more I learn, the more I realize how little I know (paraphrased)."

– Socrates et. al.

Acknowledgments

First and foremost I would like to thank my parents for all of their love and encouragement throughout this endeavor. Finally I can answer their question "Hey Son, when do you think you will be finished?" My Siblings David, Joshua, Jessica, Rebekah and the recent additions of Bonne, Matt, and Colton also have inspired me in numerous ways.

My fellow graduate and undergraduate students, past and present have also had a tremendous impact on my life, without them, this degree would have been much less fun. Greg Bishop, thanks for showing me around the labs and getting me started. Nutan and Ajit, thanks for the help with processing, characterization and MBE. Also, thanks for all the coffee breaks and conversations, you two have taught me a lot about both technical subjects and life. Freddie and Clark, the Caribbean guys, thanks for snowboarding trips, the times studying for class, and for teaching me not to take life too seriously. Montoya, thanks for all the off the wall science conversations. Marzi, Ali, and Arezou, thanks for all the office shenanigans and for teaching me Farsi. Brianna, thanks for help with processing, MBE and the tea times. Ted, "Hey, what's up?". I would like to acknowledge the rest of the office in no particular order including PJ, Lilian, Yi, Orlando, Emma, Sadvikas aka "Happy", Gunny and Chris (wait a second, Gunny and Chris aren't in the office).

The post-doctoral researchers that helped me get started, Yagya and especially Elena, I greatly appreciate your help and encouragement during my young immature graduate days. The new post-doctoral researchers, Zhaobing, Greg, and Jun Oh, thanks for the enlightening discussions and help in the labs.

I have tremendous gratitude for the people that make CHTM run day in and day out. Dan, its been great getting to know, I appreciate being there and answering your phone all those times the chiller stopped or their were kids on the roof. The custodial staff, Olivia, thanks for the spanish discussion practice. The front office staff, for getting orders through, arranging for conferences, and especially the parties. The cleanroom staff, Douglas and Big Steve, thank you so much for keeping things in working order in the cleanroom.

I also would like to thank my dissertation committee: Professor Luke Lester, Professor Sang Han, Aaron Gin, and John Klem. Professor Lester taught my first optoelectronis class and in later years let me TA for the same class. Professor Han has been present for nearly every major exam during my graduate education. Aaron Gin helped me in beginning with some initial studies but unfortunately was available to

continue in my Committee which brings me to John Klem whom I greatly appreciate for stepping in to help.

Finally I have to thank two people who are most responsible for me completing this degree. Heather Armstrong encouraged me from the very beginning and has been there every step of the way. Heather, thank you so much for all your help, all the paper work, and for all the conversations through the years. And finally, Professor Krishna, who took me into his group, taught me about grad life, and has become a good friend. Alright, is there anything else? Any other, this thing?

Mid-Wave and Long-Wave Single Uni-polar Barrier Infrared Detectors Based on Antimonide Material Systems

by

Stephen A. Myers

B.S., Engineering Physics, Tarleton State University, 2007
M.S., Electrical and Computer Engineering, University of New Mexico, 2012

Ph.D., Nanoscience and Microsystems, University of New Mexico, 2013

Abstract

Infrared detectors are very important technological tools for many different applications. Infrared detectors have existed as far back as the late 1700s but received a tremendous push 200 years later during World War II. Both thermal and photon based infrared detectors have had significant advancements with many different varieties becoming available with varying degrees of sensitivity, speed, and wavelength sensitivity. One of the best performing technologies is based on Mercury Cadmium Telluride. However, it still has limitations with regard to low operating temperature, material yield and processing difficulties. A newer material technology known as type-II indium arsenide/gallium antimonide strain-layered superlattice has received much attention for its potential superior performance from lower dark current, mature III-V material fabrication techniques, and design versatility. However, superior

dark current performance has yet to be realized due to large Shockley-Read-Hall generation-recombination current. To overcome this, researchers have taken advantage of the versatile bandstructure of the superlattice material and have created heterostructure designs to reduce dark current. These designs include the nBn, CBIRD, pMp, and pBiBn. These designs have enabled detectors have dark current behavior to be within a factor of 2 of HgCdTe based detectors. The more basic of these designs, the nBn, has been utilized in InAs detectors, InAsSb detectors, HgCdTe detectors, and both mid and long-wave superlattice detectors with success. However, questions and optimization remain regarding dark current and photocurrent behavior, band alignment, and photoconductive gain. Mid-wave InAsSb nBn detector designs with different barrier composition and doping conditions have been investigated to help elucidate effects on dark current and photoresponse. Mid-wave superlattice nBn detectors with different absorber doping conditions have been studied as well. Dark current was found to be decreased by lightly doping the barrier layer n-type. variations of the nBn design, such as the pBn and pBp have been implemented with long-wave superlattice detectors and their bias and temperature dependent dark current and photoresponse have been studied. Also, the photoconductive gain of a long-wave pBp detector have been measured and found to be slightly less than unity.

Contents

List of Figures

List of Figures

List of Tables

Glossary

$BLIP$	Background Limited Performance
BTB	Band-To-Band Tunneling
$D*$	Specific Detectivity
DH	Double Heterostructure
DUT	Detector Under Test
FOV	Field of View
FPA	Focal Plane Array
$FTIR$	Fourier Transform Infrared Spectrometer
$G-R$	Generation-Recombination
$HgCdTe$	Mercury Cadmium Telluride
HOT	High Operating Temperature
$InSb$	Indium Antimonide
IR	Infrared
$I-V$	Current-Voltage

LPE	Liquid Phase Epitaxy
$LWIR$	Long-Wave Infrared
MBE	Molecular Beam Epitaxy
$MOCVD$	Metal Organic Chemical Vapor Deposition
$MWIR$	Mid-Wave Infrared
PC	Photoconductive
PV	Photovoltaic
$QDIP$	Quantum Dot Infrared Photodetector
QE	Quantum Efficiency
$QWIP$	Quantum Well Infrared Photodetector
$RHEED$	Reflection High-Energy Electron Diffraction
SRH	Shockley-Read-Hall
$SWIR$	Short-Wave Infrared
$T2SL$	Type-II Superlattice
TAT	Trap-Assisted Tunneling
TE	Thermoelectric
$VLWIR$	Very Long-Wave Infrared

Chapter 1

Introduction

Technology that utilizes infrared radiation has garnered an immense amount of applications and consequently the research to develop and improve infrared detection technologies is very strong. Discussions behind the physics of the causes and detection of infrared radiation are quite numerous including several texts from respected authors in the field [13, 14, 15] and many Ph.D. dissertations [16, 17, 18, 19]. The thrust of much infrared research today is developing high performing imaging technology operating at high temperatures [20, 21, 22]. Technologies at the forefront of infrared imaging are Mercury Cadmium Telluride (HgCdTe), Indium Antimonide (InSb), GaAs/AlGaAs based Quantum Well Infrared Photodetectors (QWIPs) and microbolometers. Upcoming technologies include InAs/GaSb Type-II strain layered superlattice (T2SL) and InGaAs/GaAs/AlGaAs Quantum Dot Infrared Photodetectors (QDIPs). In this chapter I will outline the history of infrared detectors and infrared imaging technology, describe modern infrared applications, describe modern detector technology and its limitations, present a motivation for development of new technology and outline the research of this dissertation.

1.1 Historical Perspective of Infrared Detectors

Infrared detection has arguably been around as long as living creatures have been able to determine the difference between hot and cold. In a more quantitative sense, a thermometer could count as an early infrared detector, which started to appear during the 16th and 17th centuries and was developed by many scientist at the time, one of the most notable ones being Galileo Galilei (1564-1642) [23] in 1592. It received many improvements through time including being fitted with a scale and being sealed as to prevent effects from barometric pressure. But the first instance of using a thermometer to detect "invisible light" was by Sir William Herschel (1738-1822), the Royal astronomer to King George III, in 1800 [24]. He came about the discovery while he was working with different colored optical filters to reduce the intensity of light while observing the sun. He noticed that the various filters produced different amounts of heat and decided that the amount of heat transmitted through a filter depends on the color of the filter. His original experiment to test this idea consisted of a prism to disperse sun light to its component colors of light and use a thermometer to measure the temperature under each color. An illustration from the original paper he published is shown in figure 1.1. He assumed there must be a maximum point for the heating property of the light and progressed through each color looking for it. However, the measured temperature continued to increase at the end of the spectrum on the color red. So he continued to move the thermometer beyond the red region of the spectrum to where no apparent light was observed but still measured an increase in temperature. Thus infrared radiation was discovered.

Herschel was not actually the first to measure the temperature, Marsilio Landriani (1746−1815) from Italy conducted a similar experiment in 1777 investigating the temperature measured under different colors of illumination. However, Herschel was the first to determine that heat transmitted through the prism continues to increase in intensity, and have a maximum, well beyond the visible spectrum. Having made

this discovery, he set about measuring the radiation from various light sources like candle light and kitchen stoves as well as obtaining crude transmission measurements from different materials; anything from wine and brandy to glass and natural crystals, to determine suitable optical filters for his work. Herschel thus laid a foundation for infrared research by discovering that there is some source of energy conveyed by heat that behaved similarly to light, by identifying a detector (a thermometer) to use, and by showing that various materials transmit light and heat differently.

There were, however, limitations with Herschel's detectors. For instance, the time required for a single measurement was sixteen minutes and the minimum resolvable temperature was 0.5. As time progressed more sensitive detectors were developed. The thermoelectric effect discovered by Seebeck in 1821 led Nobili to create the first thermocouple in 1829. Melloni, in 1833, created a thermopile by placing several thermocouples in series which created a detector with a sensitivity forty times greater than the best available thermometers at the time [13].

Melloni continued Herschel's spectroscopic study of optical materials for their transmission properties. He made the important contribution of discovering that typical glass has a limited infrared transmission spectrum but rock salts, on the other hand, have rather extensive infrared transmission spectrums. Thus began the use of optical materials that slowly dissolve with humidity; at least the dry New Mexico weather is less cruel in this regard. He went on to measure the solar radiation spectrum and originate the technique for measuring the transmission spectrum of the atmosphere using the sun as a source. He even identified variations in the transmission spectrum as effects from water vapor absorption. Research into atmospheric transmission in the infrared by others led to the creation of figure 1.2 which inspired the convention of classifying different portions of the spectrum into near-IR (NIR), short-wave-IR (SWIR), mid-wave-IR (MWIR), and long-wave-IR (LWIR) based on the the different high transmission windows in the spectrum as outlined in table 1.1.

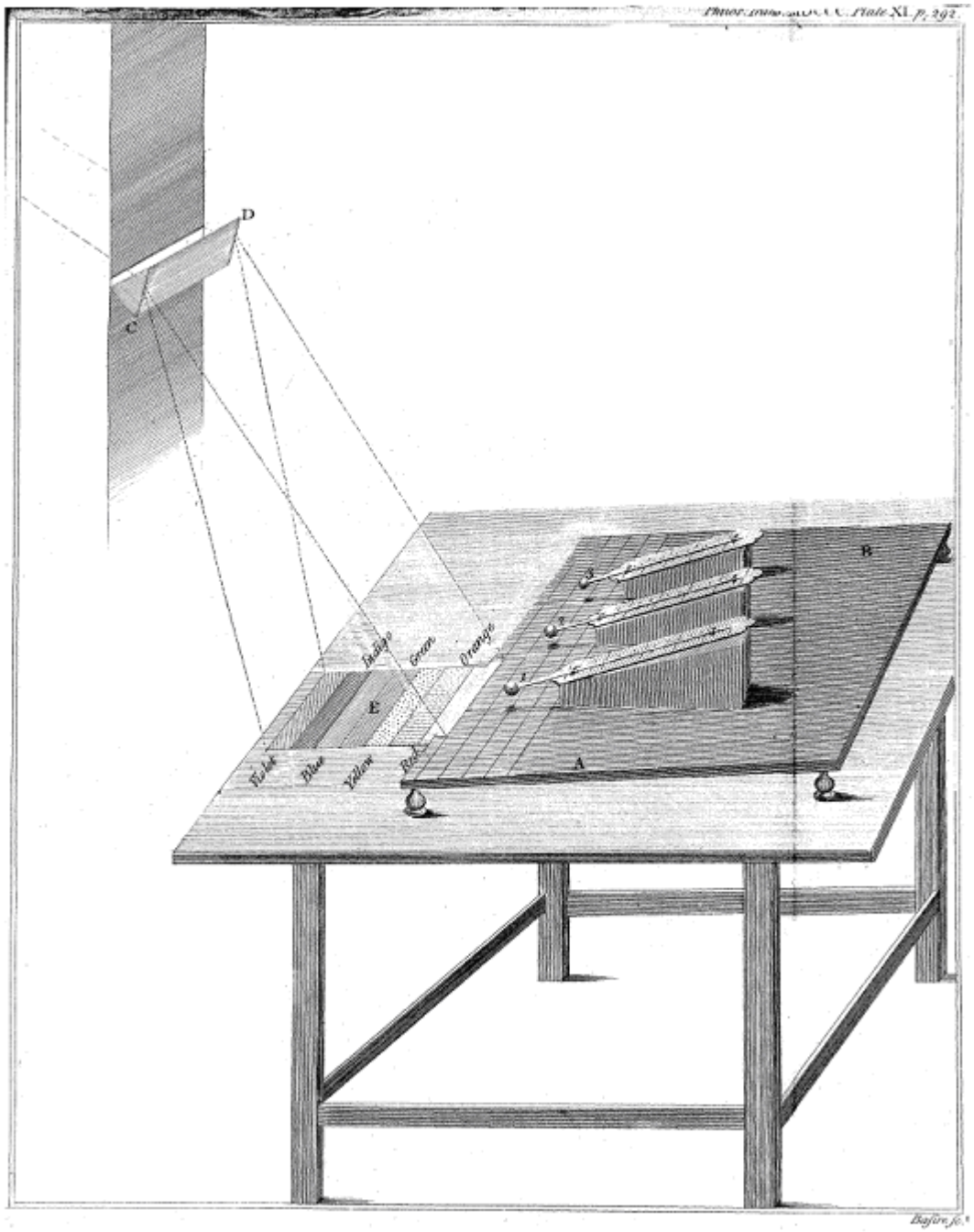

Figure 1.1: The apparatus used by William Herschel to detect infrared radiation. Light shines through a slit which is covered with a prism to disperse the different wavelengths of light on the table. Thermometers are arranged on a moving platform on the table to measure the temperature at each color or wavelength.

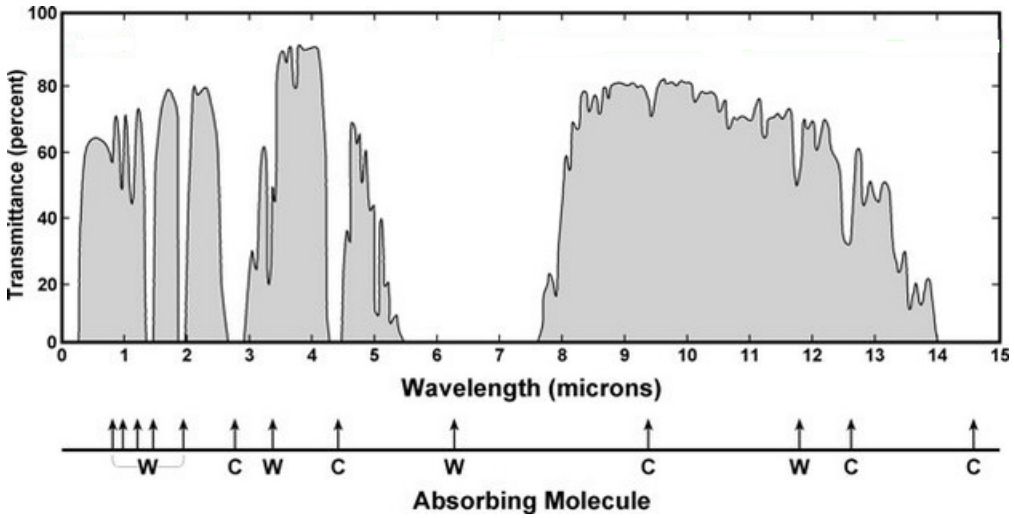

Figure 1.2: Infrared transmission spectrum of the atmosphere with absorption valleys labeled with W (water) and C (carbon dioxide).

Table 1.1: Infrared range classification

Label	Abbreviation	Range (μm)
Near Infrared	NIR	$0.7 - 1.5$
Short-Wave Infrared	SWIR	$1.5 - 2.5$
Mid-Wave Infrared	MWIR	$3 - 5.5$
Long-Wave Infrared	LWIR	$8 - 14$

In 1840 one of the first thermal imagers was created by non other than William Herschel's son John Herschel. It utilized a thin film of oil and created a "heat picture" based on a heat induced differential evaporation rate across the film surface. This was a precursor to the evapograph [25].

By 1880 the thermometer, thermocouple and thermopile had not been improved upon so a new technology was born; the bolometer. Details of the operation of a bolometer are described in a later section. Professor S. P. Langley of the Allegheny

Observatory at the University of Pittsburgh, Pittsburgh Pennsylvania, developed the bolometer [26] which was 30 times more sensitive than the thermopile.

In 1894 Max Planck (1854 - 1947) had been assigned the task of theoretically working with black body radiation to determine how to achieve the maximum amount of light out of light bulbs with minimal energy requirements. Wilhelm Wien had developed an empirical model that worked well describing short wavelength black body emission but failed with long wavelengths. By 1900 Planck had developed a law describing black body radiation for the whole spectrum by using the idea that light is composed of quantized amounts of energy. The formula for Planck's law as a function temperature and wavelength is shown here:

$$B_\lambda(T) = \frac{2hc^2}{\lambda^5} \frac{1}{e^{hc}/(\lambda k_B T) - 1} \tag{1.1}$$

The black body radiation spectrum as a function of wavelength for several source temperatures is shown in figure

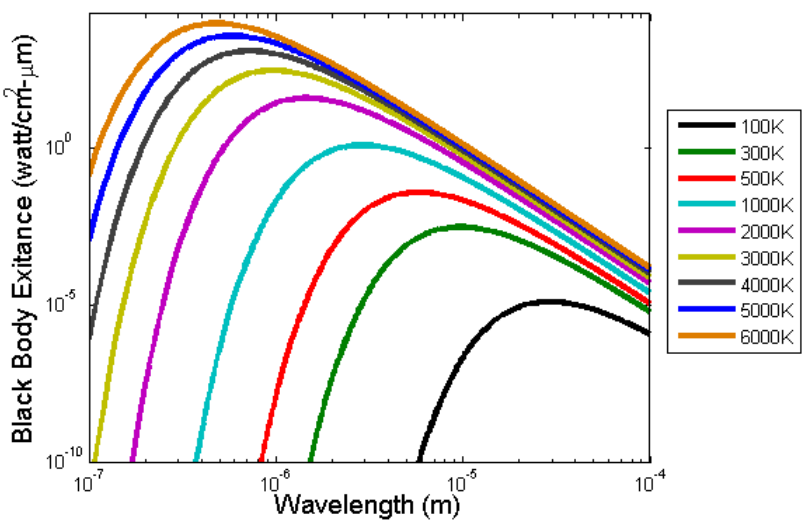

Figure 1.3: Black body spectrum as a function of wavelength for several temperature from 100K to 6000K. Note that the visible spectrum has a range of 400nm – 700nm ($4 \times 10^{-7} - -7 \times 10^{-7}$) and the infrared spectrum spans from 700nm – 1mm ($7 \times 10^{-7} - -1 \times 10^{-3}$).

Then in 1905, Albert Einstein (1879-1955) experimentally confirmed the idea of quantized energy levels of light or photons with the discovery of the photoelectric effect. This lead to the development of photon detectors or photodetectors, as opposed to the previously discussed thermal detectors which were much slower and less sensitive. In 1917, Theodore Case (1888-1944) created the first of such detectors from thallus sulfide which operated as a photoconductive detector. During the time of world war II, significant research by several countries was devoted to infrared research in which detection systems based on lead salts were developed. In the following decades, newer technologies arose including indium antimonide (InSb) detectors in the early 1950s [27, 28, 29]. However, InSb could only detect MWIR; research into LWIR detectors lead to the development of HgCdTe detectors in the late 1950s [30, 31]. With the increasing amount of research with different detector technologies, a consistent and standard method of comparing them needed to be established. Work with developing such figure of merits as detectivity was carried out by Jones in the 1950s [32, 33, 34, 35]. In recent decades, with the improvement of material and manufacturing technology, imaging systems became more prevalent and reliable leading to many practical applications some of which will be discussed in the next section. Common modern technologies will be discussed in a later section.

1.2 Infrared Imaging Applications

Infrared detection technologies serves many applications. A large push for modern infrared research is in imaging applications which itself has a variety of applications with interests from defense, security, surveillance, astronomy, medical, energy monitoring, and industrial. Probably the most common application for IR thermal imaging is night vision which is valuable because it relies solely on the objects as a source signal and not low levels of ambient light like image intensifiers. This section

will explore a couple less common applications of IR imaging.

Medical applications of infrared detection has actually followed relatively close to the history of infrared detection in itself. For instance, it is well known that a person's body temperature is a function of their health and thermometers have been used since the 1860s to aid medical practice. Likewise, when infrared detection technology saw vast improvement during WWII, medical applications were quickly sought. Medical thermal imaging has been around since the 1950s and has been used to study breast cancer, skin thermography, tissue characterization, imaging during surgery, dentistry, and veterinary medicine [36]. It is even used to monitor temperature of patrons at airports to check for illness [37].

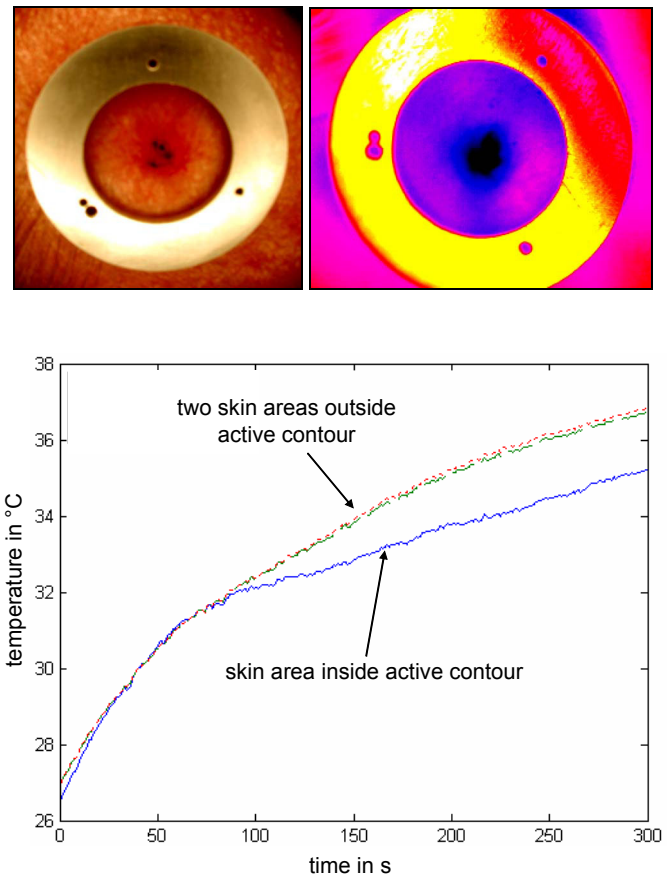

Figure 1.4: Skin lesion in visible and infrared. The accompanying graph shows the change in temperature over time following an initial cold state for both the lesion and normal skin [1].

Diagnosing skin cancer is a medical application that has received attention in the past decade from multiple groups including researchers at the Institute of Medical Engineering at the University of Lbeck [1], John Hopkins University [38], and SK Infrared^{TM} [39]. Early results taken from ref [1] are shown in figure 1.4. In the study a lesion on a patient is uniformly cooled along with some normal skin surrounding the lesion. An infrared camera is used to monitor the lesion and surrounding skin as it warms to normal body temperature. The temporal and spatial temperature variation of the skin and lesion can be extracted from the infrared video and plotted as shown.

The difference in the rate of change in temperature of the lesion as compared to normal skin offers a clue as to the state of health of the lesion. This particular lesion is basal cell carcinoma which is malignant; in the study they also looked at a displastic nevus, a much less threatening condition, which had a very similar rate of temperature change as compared to normal skin. With continued work with studies like these, researchers hope to develop a non-invasive tool for diagnosing skin cancer.

Like medical imaging and other applications, industrial applications have existed for infrared from the beginning. For instance, Herschel's first use for infrared detection after discovering it was to use it to test optical filters for his telescope. More modern applications include chemical sensing, circuit trouble shooting, and mechanical stress monitoring amongst others. For instance, IR imaging can be used to find microscopic cracks in materials with the help of an ultrasonic transducer [40]. By applying short pulses of sound waves to some material with the low frequency transducer, localized heating will ensue in the area of the crack due to the friction of the surfaces within the crack rubbing against each other. An IR imager is then used to monitor the heat and locate the crack.

1.3 Modern Detection Methods/Materials

Infrared detector technology includes two primary types, which are photon detectors and thermal detectors. Thermal detectors include Golay cells, thermopiles, and bolometers. Photon detectors are further divided into two categories namely photoconductors and photovoltaics. Each of these can be made of semiconductor materials, the most prominent being indium antimonide, mercury cadmium telluride, and gallium arsenide and aluminum arsenide based quantum well detectors. This section will introduce these different technologies and their status in research and commercial availability. In addition to mainstream technologies, emergent technologies will

be discussed as well, namely III-V superlattice materials that rely on interband transitions.

Thermal detectors work by an element being locally heated by impinging infrared radiation. The change in temperature of the absorber element, with respect to a reservoir to which the absorber is anchored, is then measured directly by the change in resistance across the absorber. Figure 1.5 shows a diagram and scanning electron microscope (SEM) image of a microbolometer that would be found in a microbolometer FPA.

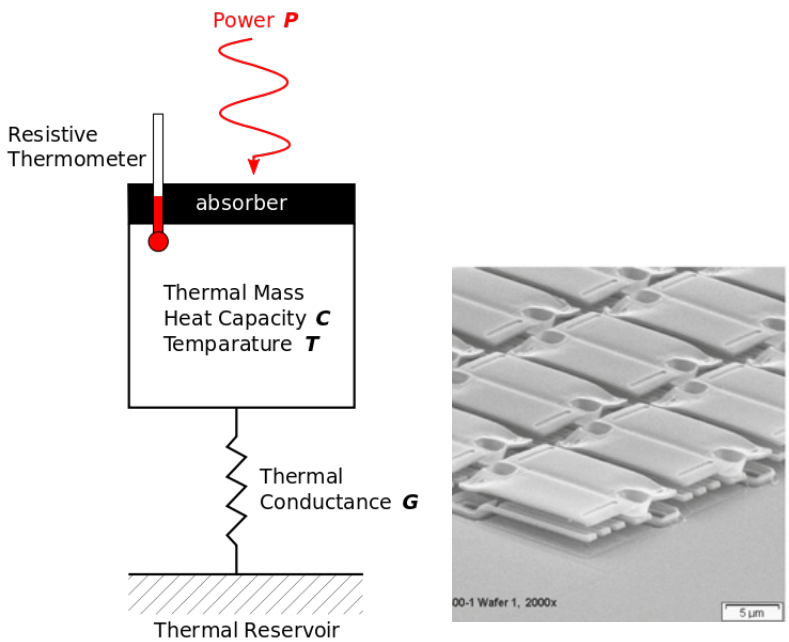

Figure 1.5: A bolometer consists of an absorbing element anchored to a heat sink or thermal reservoir by a channel with some conductance, G (illustrative figure on left). An SEM image of an actual microbolometer array (right).

A weakness of bolometers is that they are inherently slow (50 - 100Hz) as compared to photon detectors because the speed of bolometer is related to the ratio of the heat capacity of the absorber and the thermal conductance it has with the reservoir. Also, they have comparatively lower detectivity values ($10^8 - -10^9$ Jones) compared

to photon detectors. However, many bolometer designs operate at room temperature and even with their slow response speed, this places them at a considerable advantage for LWIR operation.

Photon detectors work by absorber elements creating electrical signals (photovoltaic) or producing a change in conductivity (photoconductive) by absorbing photons in the infrared spectrum much in the same way modern digital cameras work. An illustration of both photovoltaic detectors and photoconductive detectors are shown in figure 1.6.

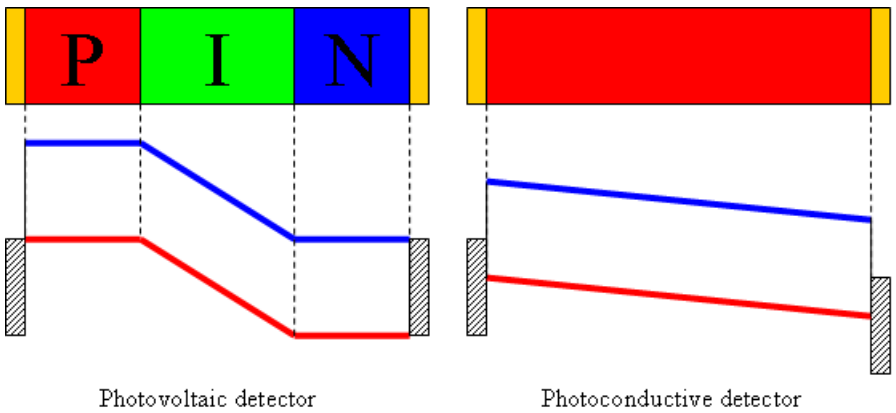

Figure 1.6: Diagram and bandstructure of a P-I-N photodiode and a photoconductor. for the PIN detector the different regions are labelled, the photoconductor is uniform throughout, and the gold rectangles on the end represent the metal contact. In the band structure in the lower portion of the figure, the blue line represents the conduction band, and the red line represents the valence band energy. A photon is absorbed when it has sufficient energy to promote an electron from the valence band to the conduction band.

Photon detectors are markedly faster (100kHz - 50MHz) than thermal detectors with photovoltaic detectors being faster than photoconductive detectors. However, most such detectors require cryogenic cooling with a roughly inverse relationship between the operating temperature and cut-off wavelength. For instance most SWIR detectors, like InGaAs detectors, operate at room temperature and most MWIR and

LWIR detectors require cooling to 77K or colder. But photodetectors generally have significantly higher detectivity values (10^{10} Jones for LWIR).

There are several mainstream technologies that are commercially available from numerous manufacturers. Some of these technologies include InSb, MCT, QWIPs, and microbolometers. Some manufacturers include FLIR, EPIR, SOFRADIR, Teledyne Judson, Hamamatsu, Semiconductor Devices, IR Associates, and Qmagiq. This section will cover different mainstream technologies available, describe their characteristics, advantages, disadvantages, and list companies that make them. The primary ones that will be discussed and compared, however, are InSb and HgCdTe given they both operate by interband transistions (carrier excitation from valence band to conduction band) which is similar to the operational behavior and characteristics as the upcoming superlattice based competitor.

Indium Antimonide (InSb) InSb detectors are one of the primary technologies used for MWIR applications because of its good yield, responsivity, detectivity and spatial uniformity [41]. It is manufactured and sold by several companies including but not limited to InfraRed Associates, Judson Teledyne, Hamamatsu Photonics, Semiconductor Devices, FLIR, Raytheon Vision Systems, etc. Its performance is comparable with MCT and growth and fabrication procedures are well established. Specific detectivity values reported by the previously mentioned companies are $\sim 1 \times 10^{11}$ Jones. However, they require cryogenic temperature operation (77K) and do not have a tunable band gap. Thus, InSb detectors performance are limited to MWIR and cannot be used for high temperature operation. They are nonetheless one of the primary detector technologies for MWIR.

Mercury Cadmium Telluride (HgCdTe, or MCT) based detectors have some of the best performance characteristics. MCT detectors have tunable band gaps, and consequently a tunable cut-off wavelength, by variation of the material composition, and have high responsivity and detectivity [42]. The responsivity and detectivity of

MCT detectors are very good with values very close if not at ideal background limited conditions. The main drawback of MCT detectors is that they are very expensive due to low yield from difficulties in handling and processing. MCT detectors are widely available and are produced by all the companies listed in the previous section as well.

QWIP detectors are photoconductors and work using intraband transitions (transitions from confined energy levels in quantum wells to continuum energy states above the conduction band). Such detectors have good uniformity and low dark current but are limited by cryogenic temperature operation (60-80K) and low quantum efficiency due to a lack of normal incidence absorption [43]. They have achieved commercial success with companies such as Qmagiq (US, http://www.qmagiq.com/) and IRnova (Sweden, http://www.ir-nova.se/). A graphical illustration of the basic operation of a QWIP detector is shown in figure 1.7.

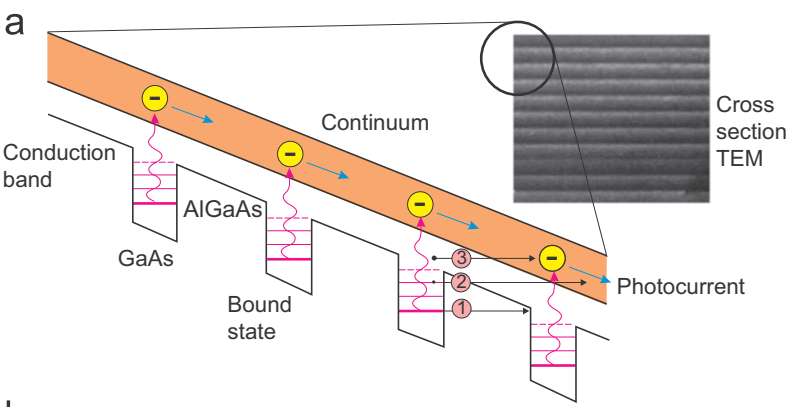

Figure 1.7: QWIP detector bandstructure, photon absorption and transport illustration from ref. [2].

Indium Arsenide (InAs) and Indium Arsenide Antimonide (InAsSb) detectors are limited similarly as InSb detectors but have shorter cutoff wavelengths and can operate at higher temperatures. In recent years InAs and InAsSb detectors have been used in nBn [6, 44] architectures to achieve higher operating temperatures and

are now commercially available operating at temperature of 150K from SCD. Several technologies including MCT and InSb are shown in figure 1.8.

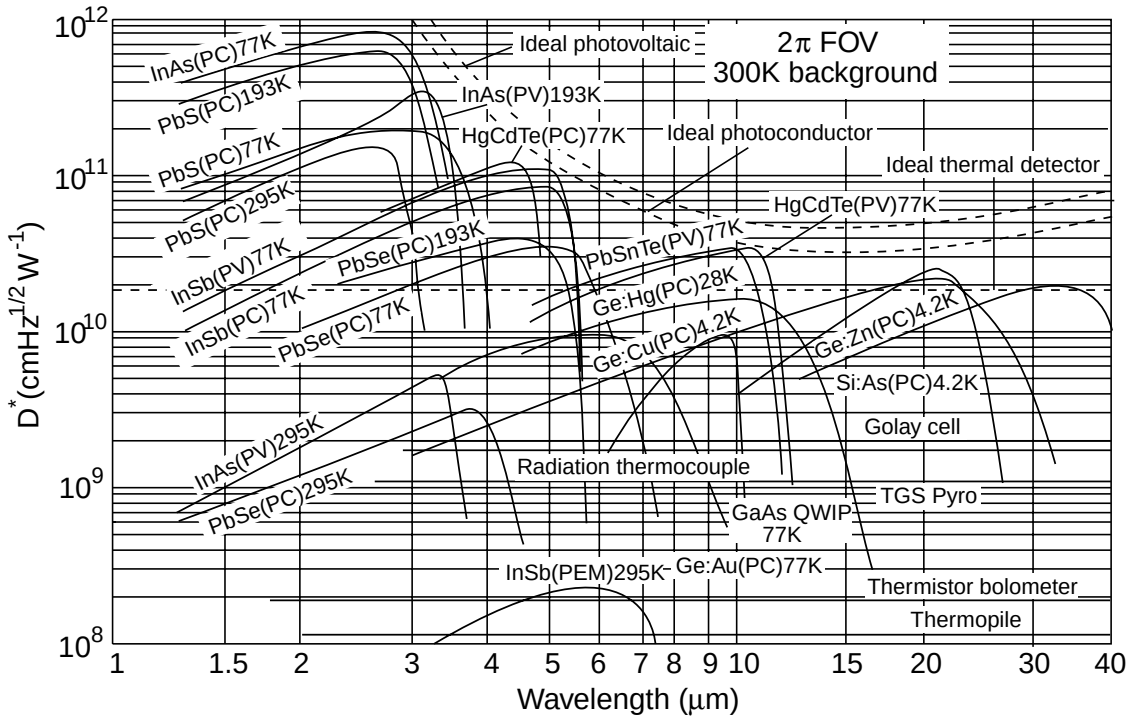

Figure 1.8: Specific detectivity vs. wavelength plot for several different detector technologies from ref. [3].

1.3.1 Figures of Merit

Detectors are evaluated and compared for their performance using several characteristics or figure of merits such as detectivity as mentioned in an earlier section. This section will outline and describe some of the more common figures used. More detailed definitions and techniques for determining their quantities are discussed in chapter three.

Spectral Response: This is the electrical response produced by a detector depending on the wavelength of light or radiation it absorbs. It indicates the cut-off

wavelength, whether it is, for example, a short-wave, mid-wave, or long-wave (SWIR, MWIR, or LWIR) detector as well as the spectral range of the detector, whether it is a narrow band or broad band detector.

Operating Temperature: This is the temperature at which a given detector can work properly. This parameter is very important and is one of the major motivations for IR detector research. It determines if a detector requires cooling, and if so, what kind and how expensive the detector will be as well as its reliability. Examples of different means of cooling detectors are shown in the following table

Table 1.2: Different types of cryocoolers and their temperature ranges

Cryocooler	Temperature Range (K)
Single stage thermal electric cooler (TEC)	230 − 300
Multi-stage TEC	180 − 300
Radiation coolers	80 − 300
Joule-Thompson and mechanical refrigerators	10 − 300

Dark Current Density: Dark current is the electrical current present in a detector that arises due to some other means besides absorbed photons. It is a good indicator of the amount of noise present and consequently the operating temperature it will have. There are several factors that contribute to dark current most of which will be described in detail in chapter three.

Quantum Efficiency: Quantum efficiency (QE) has variations in its definition but for this text will refer to the fraction of light that is absorbed by carriers in the detector material. Other definitions include the amount of carriers that are extracted from the detector, however, this definition can be convoluted with photoconductive gain.

Specific Detectivity: Commonly known as D*, is a merit that describes both signal and noise of a detector. More specifically, it is the detectivity of a detector that is normalized with respect the area and noise measurement bandwidth of the detector, where detectivity is the inverse of the noise equivalent power (NEP), and where NEP is the signal power required to equal the noise level, or alternatively, the signal level required to achieve a signal-to-noise-ratio (SNR) of one.

Noise Equivalent Temperature Difference: Also known as NEDT, is the characteristic generally used to describe the performance of an infrared focal plane array (FPA). As the name suggest, it is the temperature variation of an object being viewed that is equal to the noise level. Thus NEDT is an indicator of the minimum resolvable temperature difference that a given infrared camera can perceive.

1.3.2 IR Detector Technology Status and Trends

In recent years most discussion of infrared detectors was concerned with that of third generation infrared detectors [45] and now there is even light discussion about fourth generation detectors [46]. Before this, first generation IR imaging systems consisted of linear arrays that would spatially scan across a region to form an image. Second generation systems consisted of two dimensional starring arrays. Nowadays, third generation systems consist of large format ($1-5$ mega-pixels) arrays, higher frame rates, improved thermal resolution, multi-color operation, and higher operation temperature. Fourth generation IR imaging systems as perceived by the "crystal ball" will include multimodal data acquisition "such as color, polarization, dynamic range and phase" as well as "smart pixels" such that FPA level image processing is capable of condensing the data set acquired during imaging.

Improvement in temperature operation has been one of the strongest research thrusts in third generation IR systems. Previously the trend for the operating tem-

perature as a function of cut-off wavelength has followed $T = \frac{300K}{\lambda_C}$ as dipicted in figure 1.9 [2].

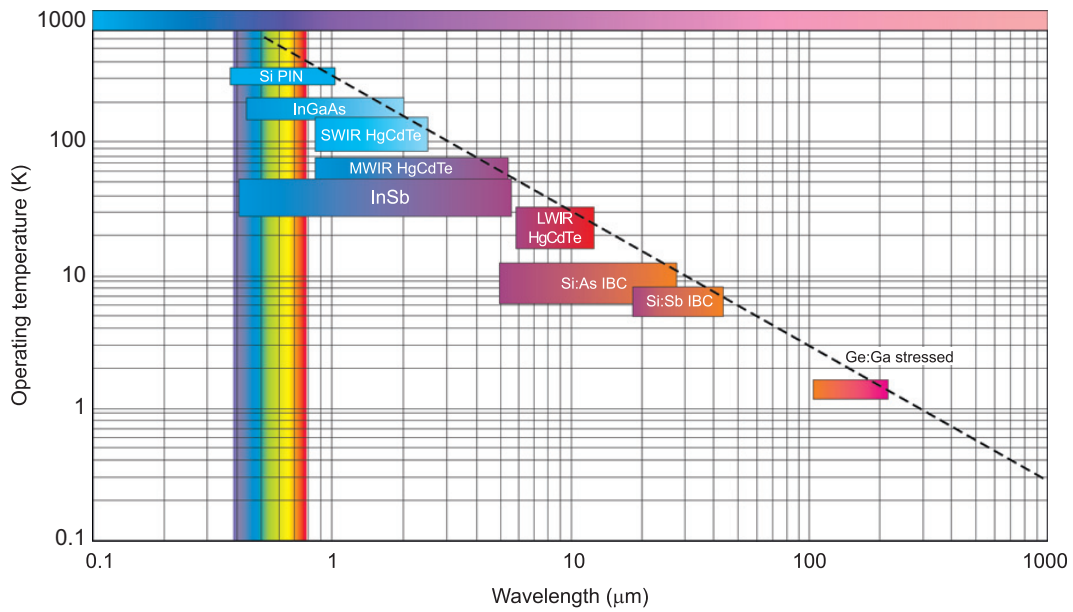

Figure 1.9: Operating temperatures for low-background material systems with their spectral band of greatest sensitivity. The dashed line indicates the trend toward lower operating temperature for longer wavelength detection.[2].

Rule 07 [47, 4, 48], an empirical fit that was originally created to be a design rule of thumb for HgCdTe IR systems, has recently become a useful trend for device comparison. The rule describes the dark current density as a function of both wavelength and temperature for HgCdTe based detectors. It holds prominence with emergent technology research such as research in T2SL because HgCdTe based detectors are currently one of the best performing detector materials available. Figure 1.10 shows Rule 07 plotted with some results for T2SL as reported in [4] as compared to theoretical expectations of T2SL detectors.

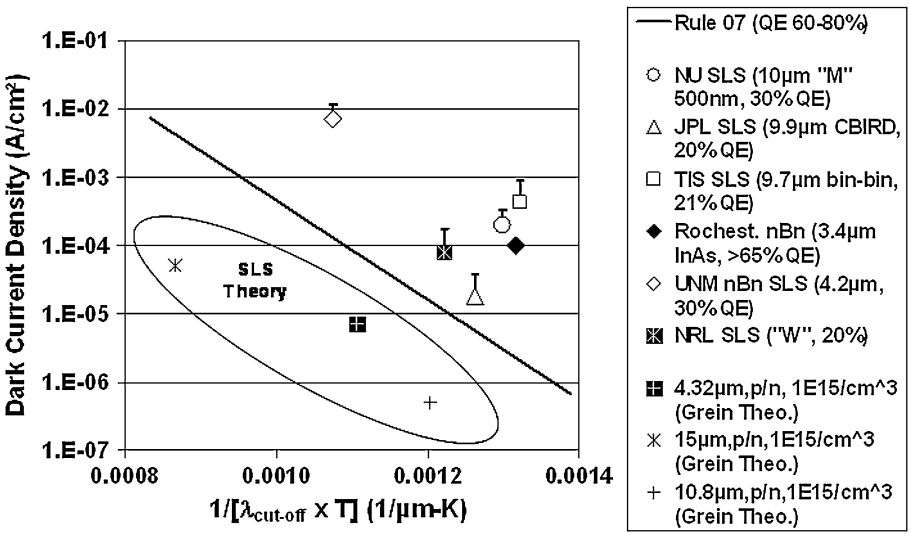

Figure 1.10: Comparison of Rule 07 with experimental and theoretical results of T2SL detectors.[4].

At the quantum structure infrared photodetector (QSIP) conference of 2012, a conference that attracts most of the leaders in infrared detector technology research, the largest sub category of presentations was focused on type-II superlattice based technologies and heterostructure detectors because of their potential for high temperature operation. The growth in T2SL research has actually sparked more research in the competitor technology, HgCdTe, to make improvements in the detector fabrication and operation including research in new lower cost substrate materials. Other research trends include enhancing optical absorption or coupling using plasmonic and photonic crystal structures [49].

1.3.3 New Research Thrusts

The different technologies discussed previously have various limitations to the performance value of each detector. The performance is ultimately dictated by the SNR as characterized by either D* for a single pixel detector, or NEDT for FPAs or similar

figure of merits. In this section, various noise sources will be discussed along with the status and trends of some popular detector technologies and new emergent material technologies and design architectures.

Sources of Noise

The sources of noise are quite prevalent in detector systems and include amplifier noise, background noise, and thermal noise processes within the detector material. This thesis is concerned primarily with the operation of the detector material itself so amplifier noise will not be discussed to much extent and background noise or noise due to the random flux of photons is the theoretical limiting factor and is handled by manipulation of the detector optics and field of view. The internal thermal noise processes of the detector material include shot noise and Johnson noise contributions from the detector electrical current and dynamic resistance. The detector current depends on Shockley-Read-Hall (SRH) generation-recombination (G-R), band-to-band tunneling (BTB), trap-assisted-tunneling (TAT), Auger generation-recombination, surface leakage current, and radiative recombination. More detailed descriptions are included in chapter three.

New Materials and Architectures: InAs/GaSb Superlattices and Novel Heterostructures

New materials and device designs have been developed to overcome these limitations. The T2SL material system has certainly garnered much attention for its potential performance, however, it still has dark current limitations the two biggest being SRH G-R current and surface leakage current[50]. Another material design utilizes Stranski-Krastinov quantum dot growth, commonly known as quantum-dot infrared photodetectors or QDIP with similarities to QWIP based detectors [51]. QDIP detec-

tors are attractive because of their normal incident absorption and band engineering versatility but still have low operating temperature due to large dark current densities at high temperatures. Modern T2SL based detectors have been designed to overcome dark current limitations by utilizing special heterostructure schemes. Some of these designs have also been utilized in the more traditional materials as HgCdTe and InAs.

The InAs/GaSb type-II strain layered superlattice material system is characterized by a theoretically superior dark current performance, as compared with HgCdTe detectors, and a versatile semiconductor band structure. T2SL material consists of alternating layers, on the order of 1nm - 5nm thick, of the III-V InAs and GaSb binary semiconductor materials as depicted in figure 1.11. The term superlattice comes from this system being a repetition of multiple crystal lattices, or a lattice of lattices, hence "superlattice". The material is also characterized by locally induced strain within each layer or period which is a key characteristic for reducing Auger recombination. To prevent the strain from compromising a thick structure, which is necessary for detectors, strain compensation layers are inserted in each period which prevent the strain from accumulating while allowing local strain to exist.

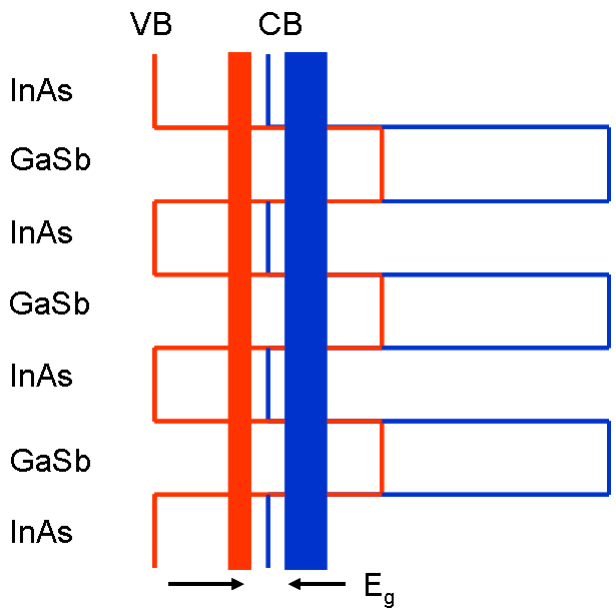

Figure 1.11: Superlattice bandstructure illustration with alternating layers of InAs and GaSb with the conduction band represented by the blue line and the valence band represented by the red line. The superlattice minibands are represented by the thick red and blue lines whose separation is the effective superlattice band gap energy.

T2SL was first theorized by Esaki and Tsu in the 1970s [52, 53] and in 1987 its application to infrared detection was proposed by Smith and Mailhiot [54]. With the improvement of molecular beam (MBE) technology, significant work has been contributed to understanding fundamental principles of theoretical properties, crystal growth, fabrication, and device operation of superlattice materials [55, 56, 57, 58, 59]. Key advantages offered by superlattice based detectors over other more traditional materials are reduced Auger recombination; mature III-V device fabrication; versatile band gap engineering to cover SWIR, MWIR, LWIR and VLWIR; high quantum efficiency; and low tunneling currents. However, since the T2SL material has yet to experimentally achieve theoretical superiority over its rival, HgCdTe, in terms of dark current levels, research continues to make improvements. Most of the dark current limitations arise from SRH G-R mechanisms and surface leakage current, thus most

research has been poured in developing heterostructures and passivation recipes to counter these issues. There is also much to still to be learned concerning growth effects on strain balancing, strength of photoresponse and cut-off wavelength [60, 61, 62]. The research in this dissertation is focused on the operation of antimonide and superlattice based IR detector technology that utilize heterostructures. The next chapter will discuss in more detail some of the more prominent heterostructures that have been studied.

1.4 Organization and Contribution of This Work

The author of this work has been involved in numerous projects with infrared detection technology. Contributions have been made with regards to characterization of materials, fabrication of detectors, and characterization of detectors. More specifically, he has co-authored work concerning MWIR and LWIR pBiBn barrier engineered detectors [10, 63], MWIR T2SL interband cascade detectors [64, 63], gallium free MWIR InAs/InAsSb superlattice based detectors [65], minority carrier lateral diffusion length in nBn detectors [66], LWIR T2SL nBn and p-i-n detectors [67], and various passivation schemes [68, 69, 70].

The dissertation presented here describes research conducted on mid-wave and long-wave detectors based on T2SL heterostructures utilizing heterostructure designs. This work is divided into seven chapters, the first being the introduction. Chapter two discusses the history of heterostructure detectors in regards to T2SL research including discussions on nBn, pBiBn, pMp, and CBIRD designs and close with a description of the device designs considered here. Chapter three describes materials and methods used in this work including material growth by molecular beam epitaxy, detector fabrication, material characterization and detector characterization. Chapter four presents work on mid-wave InAsSb detectors based on the

nBn design. Chapter five shows research with mid-wave T2SL detectors based on the nBn design. Chapter six presents the extension of the nBn design to the long wave and shows the behavior of similar devices with variations in the design. Finally chapter seven summarizes the work of this dissertation and provides an outlook for future endeavors.

1.5 Summary

This chapter introduced the history of infrared detection, modern detector technologies, detection figures of merits, emerging technologies, applications and contributions of this dissertation. Infrared detectors have come a long way since the 1800s with single element detection and sixteen minute response times to high resolution detector arrays with response times on the order of microseconds. Detectors of today are fully characterized for their wavelength response, operating temperature, efficiency, noise, detectivity, and response speed. The time of World War II saw a dramatic jump in detector capabilities with the improvement of HgCdTe, InSb, and micro-bolometer based technology. Indeed we have come a long way since Herschel's detectors of 16 minute measurements with 0.5K resolution to 1MHz speed with 20mK temperature resolution. The past few decades has also seen significant improvements in those technologies as well as new technologies garnering interest like the InAs/GaSb type-II superlattice material system. Designs utilizing this material are still in development and are the concern of many studies including this dissertation.

Chapter 2

Heterostructure Detectors

Incorporation of unipolar barriers in mid-wave and long-wave infrared detectors improve performance by lowering dark current density and, consequently, raises the detector operating temperature. Various heterostructure architectures have been utilized [11, 8, 67, 71] for performance enhancement of LWIR detectors. T2SL have gained interest in recent years for its theoretical potential to surpass the performance of HgCdTe based detectors due to a reduced auger-7 recombination lifetime [54]. However, it has not yet achieved this owing primarily to Shockley-Read-Hall (SRH) generation-recombination (G-R) mechanisms being the limiting dark current mechanism [72]. Researchers are tackling this from two different approaches, one being from a material stand point [73], the other being device design utilizing the structures listed earlier. The subject of this dissertation is concerned with the later topic.

Design of heterostructure devices with T2SL materials is made possible by the III-V 6.1$\mathring{A}$ family of materials [5] in terms of lattice parameters and band gap which makes way for the versatility of T2SL materials [74]; figure 2.1 illustrates this along with figure 2.2. Examples of the different material systems and heterostructure

detector designs are presented in this chapter.

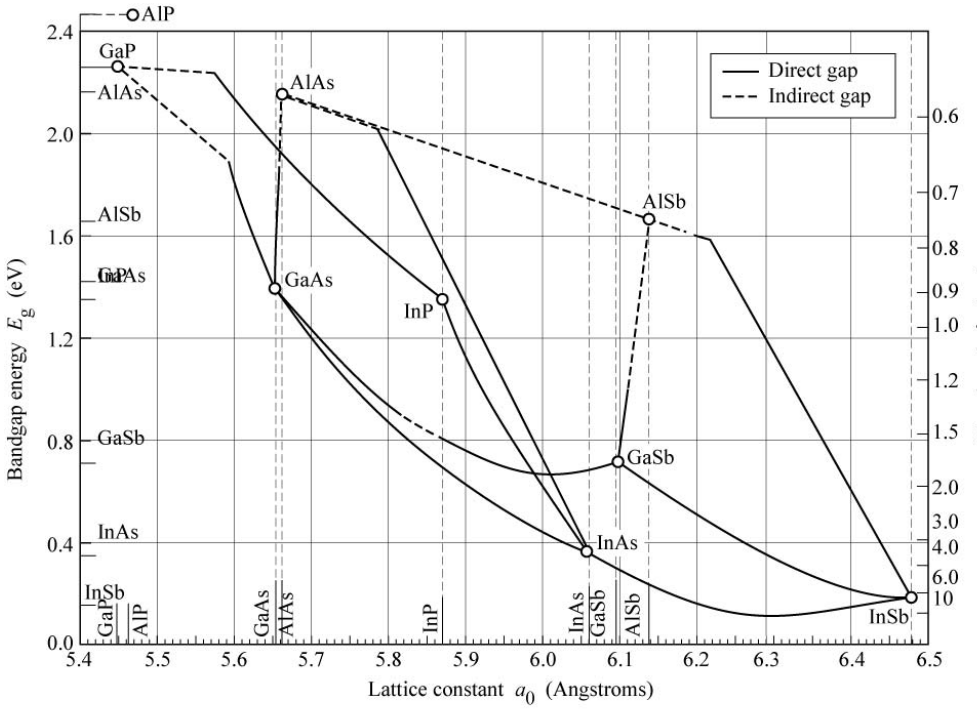

Figure 2.1: Band gap energy versus lattice constant for III-V semiconductors.

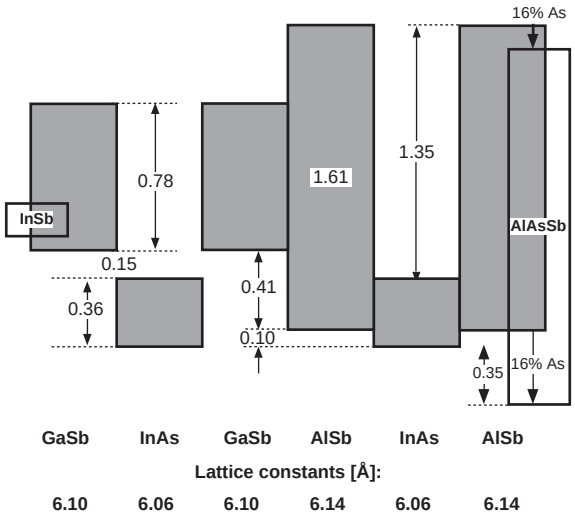

Figure 2.2: Band gap energy of the III-V 6.1$\mathring{A}$ family as presented in ref. [5].

2.1 nBn

The nBn design has become very popular and has been used in various materials. The very first proposed design that incorporated an nBn configuration was actually with HgCdTe in 1987. It received much more attention however in 2006 when Maimon and Wicks of the University of Rochester used it for an InAs detector. Much work with nBn, or XBn, has also been invested by Klipstein at SemiCondutor Devices (SCD) where it has become a commercial product. Santa Barbara Infrared and IRCameras along with Lockheed Martin have also developed a commercial camera based on the nBn design. In 2007, Rodriguez of the University of New Mexico adapted the design to the T2SL material system for the mid-wave range. It was later used for long-wave as well as dual-color designs.

The basic design of an nBn detector consists of a n-type narrow band gap absorber material followed by a wide band gap barrier layer, which has no valence band offset with the other layers and a large conduction band offset, capped with a narrow band gap n-type contact layer. The motivation for the design is that the lack of a depletion region decreases the amount of dark current in the device by reducing different mechanisms such as SRH generation-recombination, band-to-band tunneling, and trap assisted tunneling could take place. When biased, most of the electric field falls across the wide band gap barrier which also limits the amount of band bending within the narrow band gap materials. The barrier also blocks the flow of majority carrier electrons making the current due to minority carrier holes, and photogenerated electrons and holes. The drawback of the design being that it requires an applied bias to extract carriers. An illustration of the ideal nBn bandstructure under externally applied bias is shown in figure 2.3.

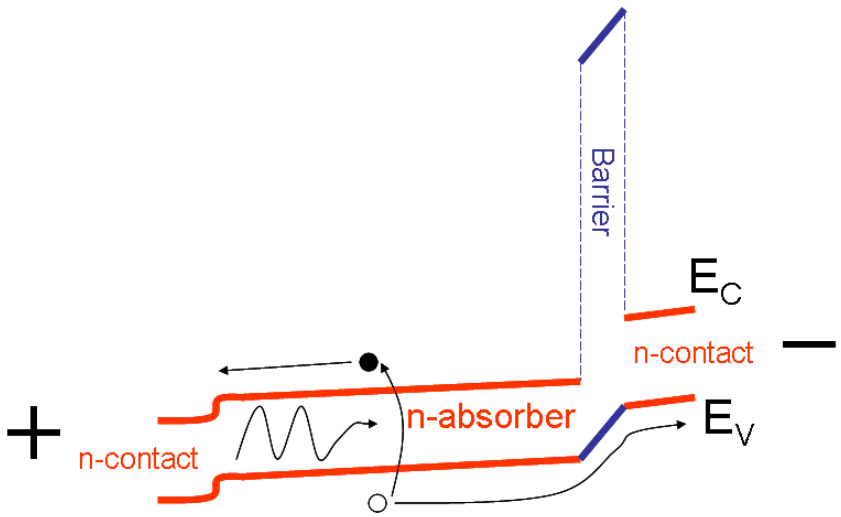

Figure 2.3: Qualitative illustration of the nBn band structure under bias with carrier absorption and current flow.

The parameters that go into designing a nBn detector are important for optimizing dark current and photoresponse. such parameters include the doping of the contact layers, absorber and barrier; the valence band alignment between the different layers; and the different possible material systems for the absorber, barrier and contact layers. Figure 2.4 shows the different alignments amongst the layers. The conduction band offset, ΔE_C, should be sufficiently large between the absorber/contact layer and barrier so as to prevent thermionic emission of carriers over the barrier from the contact layer. On the other hand, the valence band offset, ΔE_V, between the absorber/contact layer and barrier needs to be minimal or non-existent to prevent the hindrance of the flow of photocurrent. Parameters that affect the alignment of these junctions include the material composition and the doping concentration. In the case of doping, for instance, increasing the n-type dopant will raise the Fermi energy level which then by aligning with the other layers forces the conduction and valence bands to lower in energy with respect to valence and conduction bands of the other layers. Conversely, increasing the p-type doping lowers the Fermi energy level which then causes the valence and conduction band to raise in energy with respect to the

other layers. The degree to which the material composition affects band alignment greatly depends on what material is being utilized which may be constrained due to lattic matchin conditions. Misalignment of the valence band between the barrier and absorber/contact layer will result in either a well or barrier to be formed. Either case results in the blocking of current flow however the formation of a well also increases the chances of tunneling to occur. Thus for optimal device operation proper care must be taken in the design of a nBn detector.

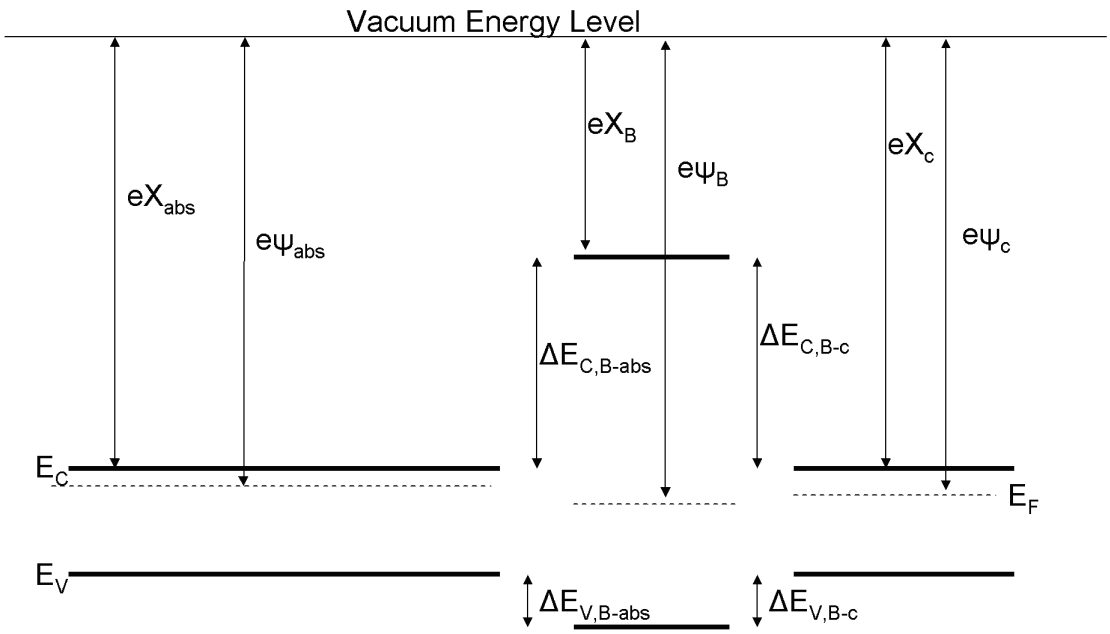

Figure 2.4: illustration of the various energy levels and band alignments of the nBn architecture.

With the reduction of dark current in the nBn design relative to a traditional p-i-n design comes higher operating temperatures. Figure 2.5 illustrates this comparison using an Arrhenius plot in which the dark current is plotted on the vertical axis on a log scale and the inverse of the temperature is plotted on the horizontal axis. The slope of the line in such a plot is known as the activation which provides clues about the limiting dark current mechanism. For instance if the slope is equal to the 0K

band gap energy ($E_{g,0}$) then the dark current is limited by diffusion current. If the slope is approximately half $E_{g,0}$ then the dark current is limited by G-R current. For most p-i-n diodes, high temperatures are dominated by diffusion current and low temperatures are dominated by G-R. In the case of the ideal nBn architecture, the current is dominated by diffusion for the whole temperature range because G-R current is either completely removed or greatly reduced. This translates to two possibilities in the improvement of detector operation: (1) a given detector can operate at the same temperature with significantly reduced dark current density and consequently reduced noise and improved detectivity, or (2) a given detector can operate with the same dark current density as a p-i-n detector but at a significantly higher temperature.

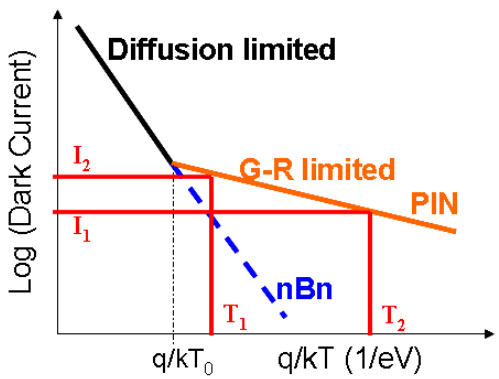

Figure 2.5: Qualitative illustration of the dark current in a nBn detecton compared to the conventional p-i-n architecture.

Aside from reducing G-R dark current, the nBn design can also be used to reduce surface leakage current by utilizing a shallow etch processing scheme. In a typical photodiode the pixel is defined by etching away the material surrounding the pixel area until the bottom contact is reached which exposes the narrow band gap absorber layer. This layer is susceptible to surface leakage current due to various surface states caused by damage during etching or oxidation. Using the nBn design, with the shallow etch fabrication scheme, surface leakage current is removed or reduced

because the narrow band gap absorber remains unetched and thus protected. This is different from passivation since the material is never once damaged and exposed. Where as with passivated devices, the material damaged and exposed during the processing and then covered with a protective material. This is akin to placing a band-aid on a wound; for nBn detectors, the wound is never made. The pixel is then defined by the minority carrier lateral diffusion length, as opposed to etched dimensions. However, a potential problem with this is if the diffusion length is longer than the separation between each pixel, interference or cross talk between the pixels can create blurry or low resolution images. See figure 2.6 for a side profile illustration of a shallow etched nBn detector.

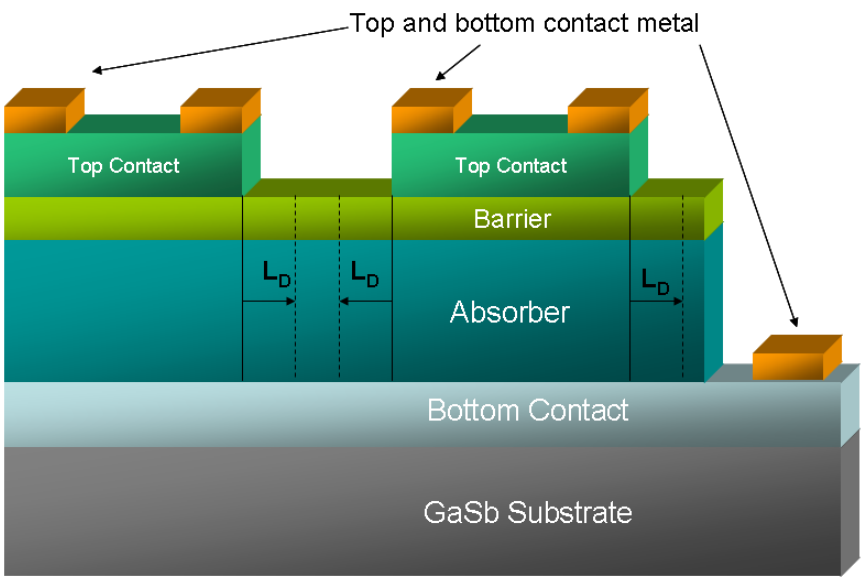

Figure 2.6: Diagram illustrating the shallow etch scheme used with the nBn device in which pixels are etched only to the barrier layer and the absorber layer is left unaltered. The total pixel area and volume is defined by the minority carrier lateral diffusion length (L_D).

Barrier designs such as the nBn design also lend themselves quite easily to multi-color detection. Starting with the nBn design, lengthen the top contact and lower its doping level such that it makes a suitable absorber. Next change its band gap while

maintaining a nearly zero valence band offset with the barrier. Now when operating the detector with a negative bias (negative top contact with respect to the bottom contact) the photo carriers created from infrared radiation absorbed in the bottom absorber layer will be collected, where as if a positive bias is applied photo carriers excited from the top absorber layer will be collected. Thus a dual-color detector detector can be created utilizing dual bias polarity operation. Figure 2.7 illustrates the band structure operation of a nBn dual-color detector.

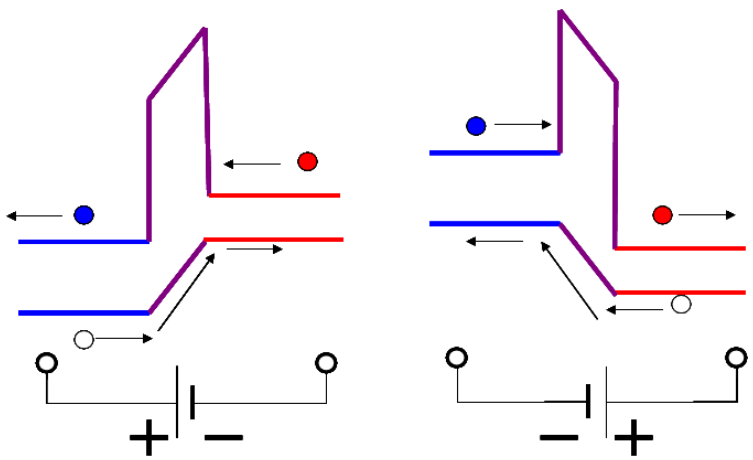

Figure 2.7: Dual color detection in nBn band structure using opposite polarities.

Some basic characteristics concerning the operation of the nBn design, as well as other heterostructure designs, are not well understood. For instance, the role of photoconductive gain is still unknown and limited work has been done to investigate. One study by Soibel et. al. [75] investigates gain in the CBIRD detector and a design similar to the nBn known as "pMp" is described as having no gain [76]. Both of theses designs will be described later in this chapter. A discussion of the physics of photoconductive gain along with an experimental study is presented in chapter six.

2.1.1 HgCdTe

The very first mention or allusion to a nBn type configuration for an infrared detector was described in the 1987 patent by Anthony White [77]. The primary motivation for such a design in HgCdTe material was to have a detector with the simplicity of a photoconductor, in terms of only having to deal with n-type material, but have the low noise or dark current of a photodiode. The patent also envisioned other variations including a dual-color design and a p-n junction diode but with an electron barrier in between. Adaptations of these variations in other materials will be discussed later.

The HgCdTe based nBn design was picked up later by Anne Itsuno [78], motivated by the difficulties associated with controlled p-type doping whether it be by ion implantation [79] or in MBE grown HgCdTe structures [80]. In addition, the versatility of HgCdTe material of band gap variation with nearly zero variation in lattice constant allows multi-color devices to be fabricated with this system as described earlier.

The device fabricated was grown by MBE on a bulk CdZnTe (211)B substrate and consisted of three layers: a narrow band gap top contact, a wide band gap barrier, and a narrow band gap absorber. All three layers are doped with indium and the growth was terminated with CdTe. The top contact and absorber had Cd mole fractions of approximately 0.3, which corresponds to a cut-off wavelength of approximately $5.7\mu m$ at 77K, and the barrier layer had a Cd mole fraction of approximately 0.64. Devices were fabricated by traditional fabrication methods: optical photolithography, plasma etching to access the absorber contact, metallization, and lift-off. Zinc Sulfide (ZnS) was used as passivation and insulation between the detector material and metal contact pads. The metal contacts consisted of 100nm of indium and the the extended metal contact pads were made with Ti/Au with thicknesses of 20nm/300nm.

A valence band offset between the absorber and the barrier hindered the photo

current at low biases resulting in a turn on voltage of $\sim -0.8V$. Dark current density above 180K was limited by Auger mechanisms; at or below 180K it saturates at $-0.54A/cm^2$. This is attributed to surface leakage current due to a strong dependence on the perimeter to area ratio. It is stated that further research and optimization of the nBn device structure with HgCdTe is necessary before an accurate comparison can be made with Rule 07. Carrier collection was concluded to be good from photoresponse measurements which implied a QE greater than 100%. The impossibly large QE was attributed to a large lateral photon collection. Further research and optimization is needed to evaluate if the nBn architecture is a suitable design for HgCdTe based detectors.

2.1.2 InAs

One of the more popular initial implementations of the nBn design was with indium arsenide (InAs) by Maimon and Wicks [6]. InAs has a typical 77K detectivity of 8×10^{11} Jones and a cut-off wavelength of approximately $3\mu m$. The initial study used aluminum arsenide antimonide (AlAsSb) as the barrier material and found using an arsenic concentration of ~ 0.15 produced the highest QE possible with a nearly zero valence band offset. The detector in the study consisted of three layers grown on an InAs substrate starting with a $3\mu m$ thick n-type InAs layer ($N_d \sim 2 \times 10^{16} cm^{-3}$ non-intentionally doped), followed by the 100nm thick AlAsSb barrier layer, and finished with a n-type InAs top contact layer ($N_d \sim 1 \times 10^{18} cm^{-3}$, intentionally doped). The material was fabricated into $100x100\mu m^2$ detectors. The initial results are shown in figure 2.8.

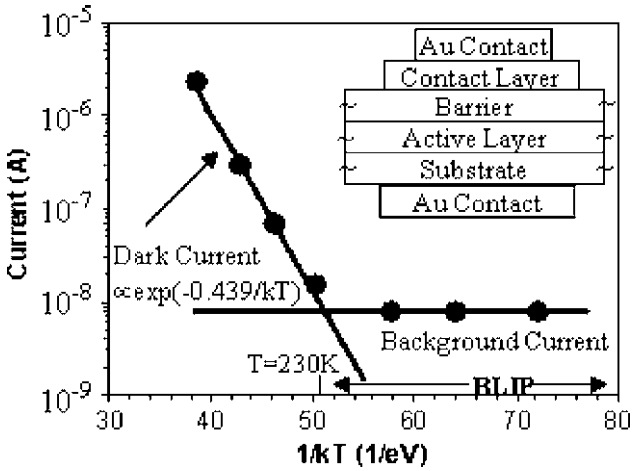

Figure 2.8: Current-voltage data as a function of the inverse of temperature for the InAs based nBn detector from [6]. The inset shows a schematic of the device structure.

For the high temperature range (230K - 300K) the detector was concluded to be free of SRH G-R current since the activation energy was 0.439eV which is comparable to the 0.415eV band gap energy of InAs at 0K. At lower temperatures (below 230K), the current is limited by the 300K (room temperature) back ground radiation (Background limited performance or BLIP) which is on the order of 100K higher than for the traditional p-n InAs detectors. This detector was also investigated for its ability to prevent surface leakage current by using a shallow etch scheme in a separate study [81]. The detector was shown to be diffusion limited from room temperature to $\sim 142K$ in comparison to a p-n InAs detector which was surface limited for temperatures below 250K.

2.1.3 InAsSb

A variant of the nBn design was introduced with indium arsenide antimonide (InAsSb), so called XBn or "bariode", by Klipstein in 2008 [82]. In this design, it is emphasized

that the structure need not be symmetric in terms of the bandstructure as illustrated in figure 2.9 in which the 'X' layer can be 'n' or 'p' type and have a different band gap energy.

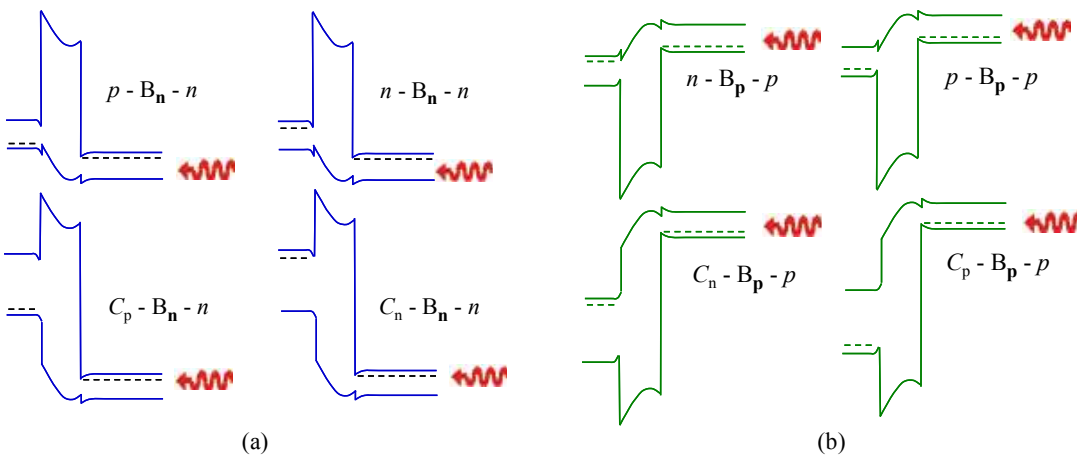

Figure 2.9: Variations of the XBn bandstructure with top contacts of the same (indicated by lower case 'n' or 'p') and different sized band gaps (upper case 'C') for both n-type and p-type doping ('n' or 'p' subscript) for the cases in which the barrier is electron blocking (a) and hole blocking (b).(from [7])

The publications by Klipstein et. al. [82, 44, 7, 83, 84, 85], though applied only to MWIR InAsSb based detectors, provide a thorough look at the operation of an nBn detector and its variations. For instance, it is shown that the tunneling current for detectors with barriers $> 1000\mathring{A}$ to be sufficient for blocking tunneling current. As well as the variation of dominant current mechanisms as a function of bias. Similar InAsSb detectors with nBn and pBn configurations were made and tested by Klem et al. [86] to compare device operation. The pBn was shown to behave similar to a p-n homojunction detector with reduced dark current; the nBn had dark current further reduced but required external bias for operation. A MWIR nB_nn FPA was fabricated and found to have a NEDT of 20mK at 150K [7]. The dark current is also shown to agree well with rule 07. Thus the InAsSb nBn or XBn variations work quite well as a competitor with InSb FPAs without having to be

cooled to 77K. Indeed they have even come to be commercial products for SCD (Hot Pelican, https://www.scd.co.il/) and IRC (http://www.ircameras.com/technology/). However, one drawback is the limitation in cut-off wavelength which is $\sim 4.2\mu m$ where as InSb has a cut-off wavelength of $\sim 5.5\mu m$ which extends to the end of the MWIR atmospheric transmission window. This is where T2SL has an advantage in being able to tune the desired response wavelength.

2.1.4 MWIR T2SL, LWIR T2SL, and dual color T2SL

The nBn architecture was utilized with MWIR T2SL material in 2007 by Rodreguez et. al. [87]. The detector structure consisted of a 400nm thick T2SL bottom contact composed of 8 monolayers (MLs) InAs / 8 MLs GaSb (n-type doped, $\sim 10^{18}$), followed by a $3\mu m$ thick absorber layer of the same T2SL (non-intentionally doped n-type, $\sim 10^{15}$), followed by a 50nm thick $Al_{0.4}Ga_{0.6}Sb$ barrier layer, and capped by a 100nm thick top contact layer with the same superlattice and doping of the bottom contact layer. At room temperature, the results were on the order of 1 A/cm^2 for current density and a peak D* of $\sim 1 \times 10^9$ Jones at -0.3V corresponding to a QE of 0.18. At 77K the dark current density was $\sim 3 \times 10^{-}3$ A/cm^2 however the device was only diffusion limited for temperatures above $\sim 150K$.

The nBn design was later applied to a LWIR T2SL design by Khoshakhlagh et. al. [67]. In the report, the performance of a LWIR T2SL nBn detector was compared with the performance of a LWIR T2SL p-i-n homojunction detector. Dark current density was found to be moderately lower in the nBn design with $0.05A/cm^2$ compared to $0.08A/cm^2$ with the p-i-n design.

2.2 pBp

The converse of the nBn detector is the pBp detector. In this design there is a large offset in the valence band between the absorber and barrier layers with little or no offset in the conduction band. The first report of such a detector was published by Nguyen et. al. [8] in which a so called "pMp" design is implemented that uses the "M-structure" [9] as the barrier material. A diagram illustrating the pMp detector is shown in figure 2.10. The "M-structure" is a superlattice material with repeating layers of AlSb/GaSb/InAs/GaSb as shown in figure 2.11 [9].

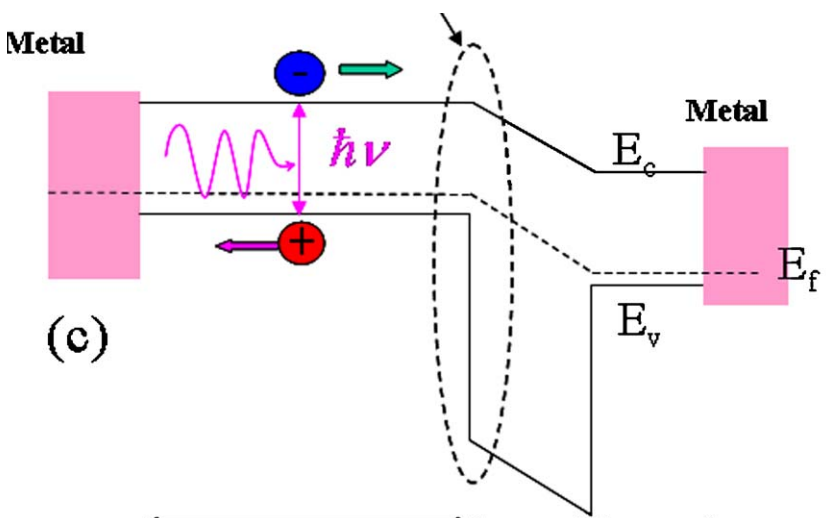

Figure 2.10: pMp band structure illustration [8]

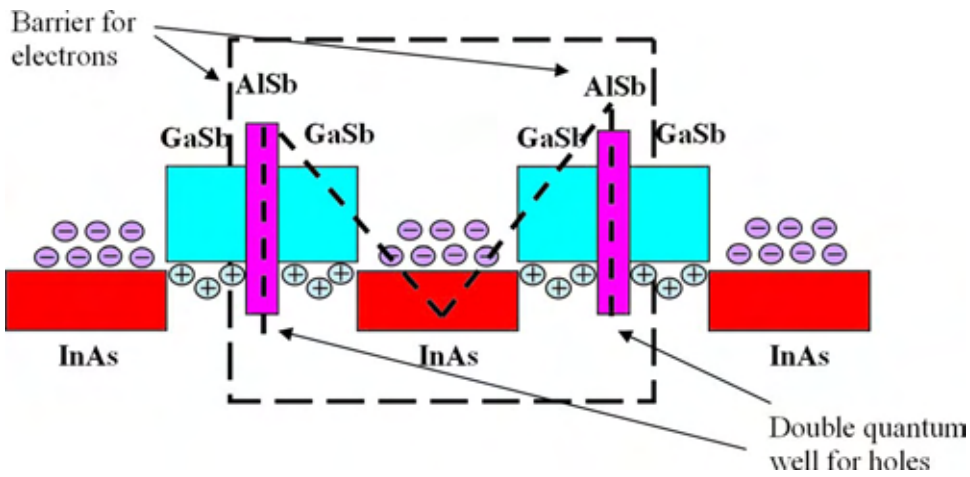

Figure 2.11: "M" structure illustration [9]

The pBp or pMp design has the advantage over nBn of utilizing electrons as the minority carrier which have a significantly higher mobility than holes in T2SL; approximately two orders of magnitude [88]. Plus with the pMp design the barrier is composed of a superlattice material which should provide further versatility in the band structure design as compared to the nBn initialy created with T2SL material which used AlGaSb as the barrier material. The pMp detector in this study is a VLWIR detector with a cut-off wavelength of approximately $14\mu m$. It resulted in a responsivity of 1.4A/W, dark current density of $3.3mA/cm^2$, and detectivity of 4×10^{10} jones at an operating temperature of 77K and bias of 50mV. The design was later adapted for the MWIR in which the contact doping layer was studied [89]. It achieved a $4.9\mu m$ cut-off with a dark current density $2 \times 10^{-5} A/cm^2$, a QE of 0.44, and a D* of $6.2 \times 10^{11} cmHz^{1/2}/W$ (Jones) at 150K and 50mV. The optimal structure was determined to be one with the barrier side contact undoped (n.i.d. lightly p-type). A highly p-type doped contact was found to lead to excessive accumulation of carriers at the barrier junction and consequently increase dark current.

A pBp design was also used to create a dual color detector [90]. The operating

principle being similar to that of the dual color nBn detector. The design incorporated a MWIR absorber with a 5 $5\mu m$ cut-off wavelength and a LWIR absorber with a $9\mu m$ cut-off. At 77K the MW response had an estimated D* and QE of 5×10^{11} Jones and 0.39, respectively, with an applied bias of $+0.1V$. The LWIR response had an estimated D* and QE of 2.6×10^{10} Jones and 0.17, respectively, with an applied bias of $-0.4V$. Aside from being dual color, this pBp design differed from the pMp design also in the barrier material which consisted of a InAs/AlSb superlattice as opposed to the M-structure.

2.3 Complementary Barrier Designs: pBiBn and CBIRD

The CBIRD and pBiBn designs have been developed with success in LWIR T2SL detectors. Both designs use complementary barrier technology. The pBiBn design, developed by Gautam et. al. [71, 10] at the University of New Mexico, consists of a n-type T2SL bottom contact followed by a n.i.d. InAs/AlSb T2SL which creates a barrier in the valence band. Next is a lightly p-type doped T2SL absorber followed a GaSb/AlSb superlattice that serves as a barrier in the conduction band. The structure is then capped with a p-type T2SL top contact. The structure resembles a p-i-n structure but with an electron barrier separating the 'p' and 'i' layer, and a hole barrier separating the 'i' and 'n' layer. An example of the bandstructure is shown in figure 2.12.

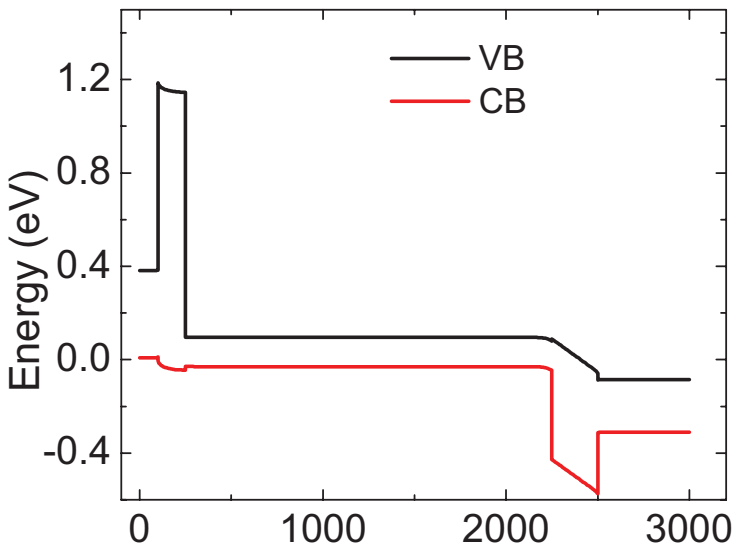

Figure 2.12: pBiBn band structure [10]

The CBIRD (complementary barrier infrared detector), developled by Ting et. al. [11, 91] at the NASA Jet Propulsion Lab (JPL) consists of a n-type InAsSb bottom contact followed by a wide band gap superlattice electron barrier, p-type narrow band gap absorber layer, capped by a wide band gap n-type top contact layer that also serves as a hole barrier. An uncommon characteristic of the CBIRD design is the tunnel junction that is used for the bottom contact between the electron barrier and n-type InAsSb layer. The bandstructure of the CBIRD is shown in figure 2.13.

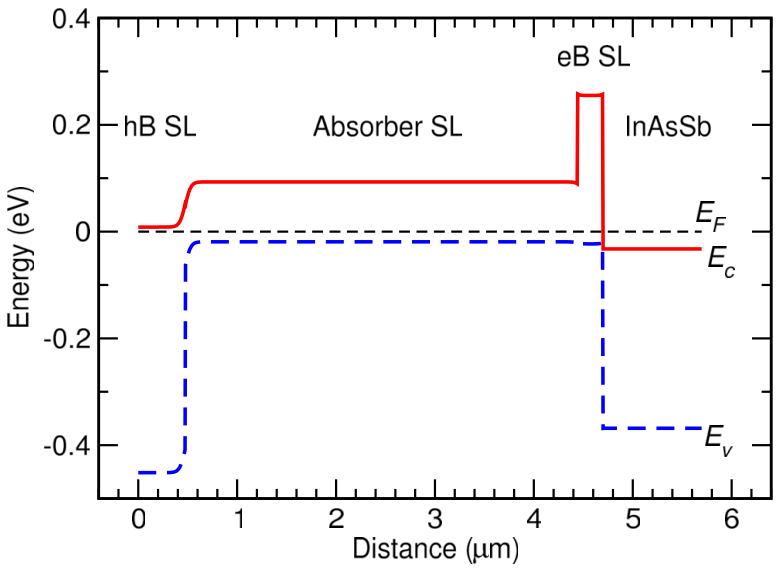

Figure 2.13: CBIRD band structure [11]

2.4 Additional III-V Superlattice Systems

Additional variants of the T2SL exist that offer improved properties in photon absorption, and band gap versatility. The W-structure, which consists of alternating layers of InAs/GaInSb/InAs/AlGaInSb, improves collection efficiency by increasing the minority-carrier mobility [92]. The previously discussed M-structure, which consists of alternating layers of AlSb/GaSb/InAs/GaSb, provides a larger degree of bandstructure variation, as compared the InAs/GaSb superlattice, for enabling the realization of complex heterostructure designs [9]. Also, there is also the N-structure, which consists of alternating layers of AlSb/GaSb/InAs, that improves photon absorption by manipulating the overlap of the electron and hole wavefunctions [93]. One final T2SL variation that has gained attention in the past few years is the gallium-free or InAs/InAsSb superlattice [73, 65, 94, 95] for its significantly longer carrier lifetime compared to the more traditional InAs/GaSb superlattice. LWIR material

have been reported with lifetimes up to 412ns [73] and MWIR material have had lifetimes up to $9\mu s$ [95]. In comparison the traditional InAs/GaSb superlattice has lifetimes on the order of 100ns for MW and 30ns for LWIR [96]. However, early detector results have either had low QE [94] for LWIR or high dark current [65] for MWIR.

2.5 Summary

Heterostructure detectors have been shown to be quite useful in improving detector performance characteristics by decreasing dark current and thus increasing the SNR. A wide variety of designs have been developed and refined that incorporate single barriers and double barriers. These designs have been utilized in several different material systems ranging from II-VI materials like HgCdTe to III-V materials like InAs and InAsSb. However T2SL materials are much more versatile in band engineering and thus lend themselves to such designs more readily. Along with multi-color design capabilities for SWIR, MWIR and LWIR. Indeed implementing heterostructure architectures with the T2SL system has proven to make it closely competitive with HgCdTe based detectors. However, design constraints do exist such as the proper alignment of the bandstructure between the absorber and barrier layers. Also some properties such as photoconductive gain are not well understood.

Chapter 3

Materials and Methods

The studies conducted within this dissertation utilized research tools available at the Center for High Technology Materials at the University of New Mexico, Albuquerque, New Mexico, unless otherwise stated. The studies include work with simulations, material crystal growth, material characterization, device fabrication, and device characterization. Simulations were used for device design and/or device operation analysis, in particular the Synopsis Sentaurus TCAD simulation environment as well as custom software developed in Matlab, were utilized. Device structures were created using Molecular Beam Epitaxy (MBE). Following device structure growth, samples were characterized for crystalline quality with X-ray Diffraction (XRD), optical characteristics using photoluminescence (PL) and Fourier Transform Infrared (FTIR) spectroscopy, and electrical transport characteristics using room temperature Hall measurements. The material was then fabricated into single pixel detectors as well as focal plane arrays in a cleanroom environment using standard III-V semiconductor processing techniques. Fabricated detectors were then tested to determine their spectral response, dark current and photocurrent behavior, responsivity, and detectivity. Detailed fabrication and detector characterization steps and notes are outlined in the appendix.

3.1 Molecular Beam Epitaxy

Molecular Beam Epitaxy, or MBE, is a very well controlled form of crystal growth in which individual layers, or monolayers, of atoms can be grown with great precision. This technique of crystal growth has allowed research in III-V superlattices to make great strides in the past few decades. Indeed, the control the atom deposition is so precise, researchers even report studies on structures incorporating sub-monolayers of atoms. The practical and philosophical implications of which continue stir up interesting debates. A diagram illustrating a MBE system is shown in figure 3.1.

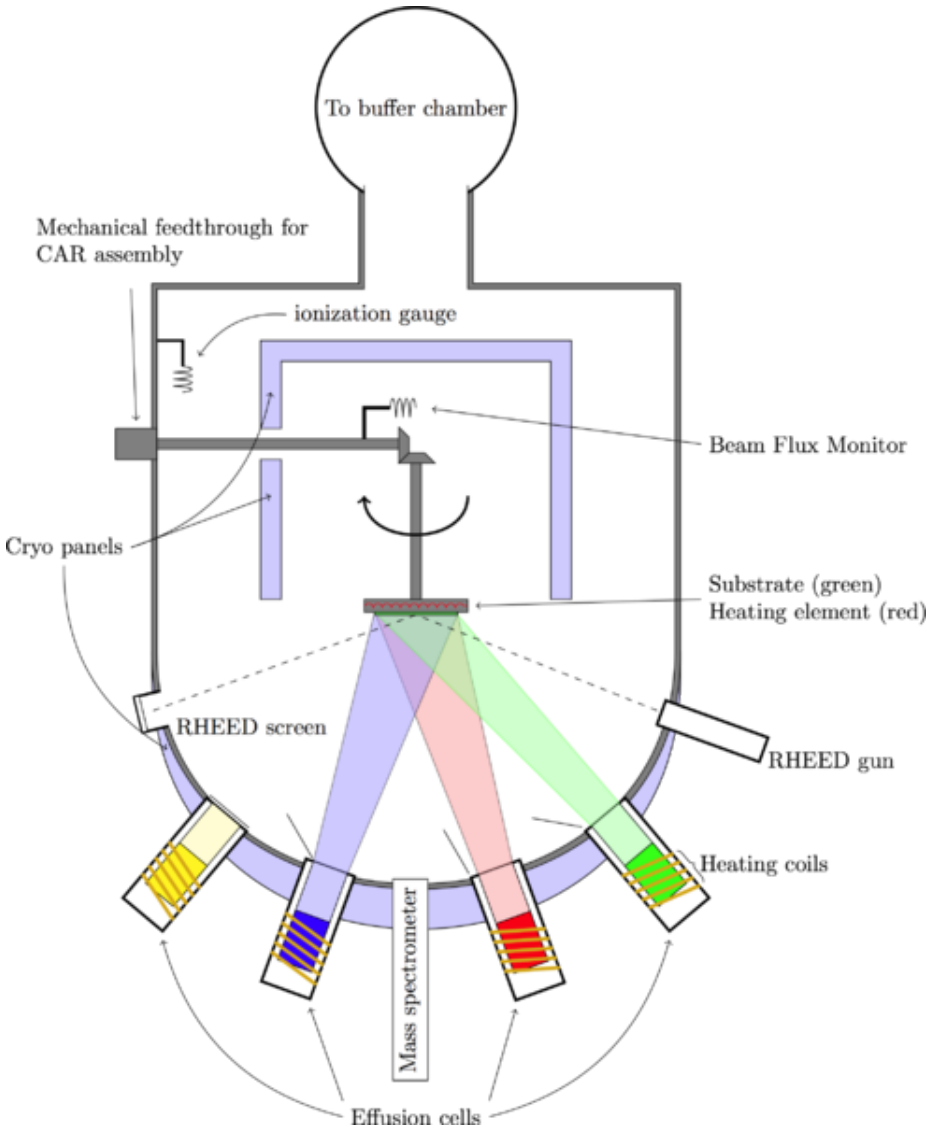

Figure 3.1: Molecular Beam Epitaxy system diagram.

An MBE system is an ultrahigh vacuum material growth chamber that utilizes elemental material sources that are heated to evaporate the component materials and deposit them in crystalline form on the target substrate. The high vacuum creates an extremely large mean-free-path for the source atoms to freely travel to the target without interaction with other atoms. The elemental sources are housed in effusion

cells that control the heating and evaporation of the material. The target stage, where a substrate is held during crystal growth, is positioned such that it is facing the source materials but placed some distance away from them to ensure uniform crystal growth over the whole substrate. The target stage also rotates during the growth period to further help with uniformity. Externally controlled shutters are positioned over the opening of the source material cells to control what material is grown and allow for structures with different material layers to be created. The development and refinement of MBE technology is what has allowed III-V based superlattice materials to become a practical material system.

3.2 Material Characterization

Following the growth of the samples, but before device fabrication, tests are conducted to determine the crystalline, optical quality, and transport properties of the material. X-ray diffraction (XRD) was measured in a Philips double-crystal X-ray diffractometer using the Cu Kα1 line, which has a wavelength of 0.154056 nm. Information gathered from XRD measurements include lattice mismatch, interface roughness, and the superlattice period spacing. Each XRD spectrum has a peak for the substrate, in our case the GaSb, and a main or zeroth order peak for the superlattice. The amount by which the peak locations differ indicate the lattice mismatch and incidentally strain in the structure. The breadth of the main peak is an indicator of the roughness of the interfaces between each layer and thus the Full-Width-at-Half-Maximum (FWHM) is often quoted when describing the crystalline quality of a superlattice. Also, the XRD pattern for a superlattice sample includes several satellite peaks due to the numerous repeating period layers. The spacing between these peaks indicate the period spacing of the different layers which is useful to confirm growth conditions and layer thicknesses.

Common optical tests conducted on the sample material prior to device fabrication include photo-luminescence (PL) and transmission/absorption. PL measurements are conducted utilizing a laser with a wavelength corresponding to an energy greater than the bandgap of the material being tested, optics and optical mounts for aligning the laser to the sample, optics for collecting the photon flux given off by the sample, a monochrometer for resolving the spectral features of the photon flux, a infrared detector, and a cryostat. An example of such a setup is shown in figure 3.2. Samples are mounted on a stage, which can be within a cryostat if desired, and the laser is turned on. The laser light on the sample excites electrons from the valence band to the conduction. After some time, the excited carriers decay and give off a photon as they drop across the band gap. The wavelength of the photon corresponds to the energy of the bandgap. This measurement is routinely conducted on freshly grown material to determine if the material is optically working properly and if the band-gap is as expected.

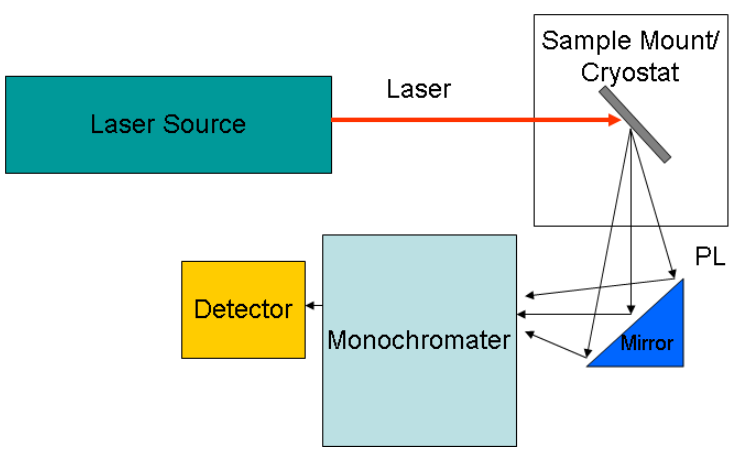

Figure 3.2: Photo-luminescence setup schematic.

Transmission measurements are also conducted to test the material optical properties. The measurement is conducted utilizing a FTIR and a cryostat. The FTIR consists of an IR source, an interferometer, IR broad band IR detector, and optics for directing the source path. A diagram of the setup is shown in figure 3.3. The

measurement is conducted by first taking a background spectrum which can be either of just atmospheric conditions, or with a substrate that is the same as the one the material being tested is grown on. then a spectrum is collected of the actual sample and normalized with respect to the background spectrum. This measurement tests the optical quality of the material; more specifically, it can be used to measure the cut-off wavelength as well as the absorption quantum efficiency of the material.

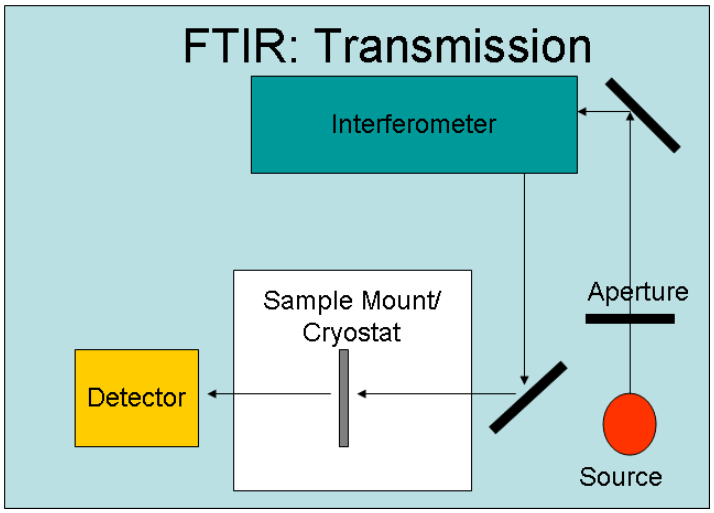

Figure 3.3: Infrared transmission setup schematic.

3.3 Device Fabrication

Following crystal growth of the device structures and material characterization, the samples are processed into functional detectors and mounted onto chip carriers. The material can either be fabricated for single pixel test structures or for FPA chips to be mounted on a read out integrated circuit (ROIC) for image testing. For single pixel fabrication, devices are made that include a variety of test structures including transfer line method (TLM) structures, single pixels with varying sizes, and single pixels with varying optical apertures but constant pixel size. Fabricated samples will

have multiple die that include each of these test structures. for FPA fabrication, each die or chip has one 320x256 FPA. There are several variables for changes within the fabrication procedure but the process can be broadly divided into the three following steps: pixel or mesa definition, surface passivation and metal contact deposition. The following figure outlines the general fabrication procedure in a little more detail. This section will describe these different steps and discuss the challenges, techniques and previous research associated with them.

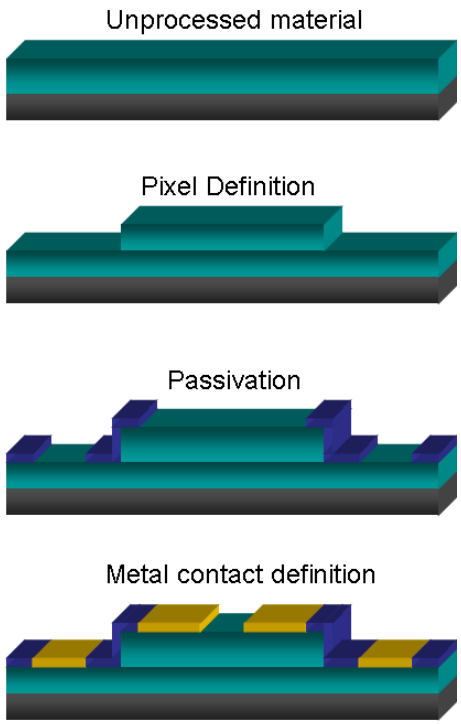

Figure 3.4: Abbreviated single pixel fabrication procedure.

3.3.1 Pixel Definition

Defining the pixel or mesa (Spanish for table) as it is commonly referred to as, generally requires etching away the material surrounding the area of interest to a depth corresponding to the bottom contact layer. To complete this requires first

to pattern the surface with a masking layer to protect areas of interest such as the pixels. Numerous techniques exist for doing this including deposition of a metal, a dielectric, or using photoresist (PR). For all the research conducted here, PR was used as the masking layer. The actual etching process can be done by either dry etching in a plasma chamber or by wet etching with acidic and basic solutions. Dry etching techniques can be divided into reactive ion etching (RIE), inductively coupled plasma (ICP), and electron cyclotron resonance (ECR). All of these techniques utilize a high vacuum chamber with at least one of the following gases: chlorine (Cl), boron trichloride (BCl3), argon (Ar), nitrogen (N), helium (He), and oxygen (O2).

RIE consists of a chamber with an electrical field placed across electrodes at the top and bottom of the chamber. The sample or target is located at the bottom electrode and has a strong radio frequency (RF) signal applied to it. The RF signal strips electrons from the gas molecules creating a charged cloud of ions or plasma. This plasma is then directed by the electric field to strike the sample target and etch away exposed material. The etching process is two fold having both a chemically reactive effect due to the highly reactive ion, as well as a mechanical effect from the impact of the charged particle on the target.

ICP is generally used in conjunction with RIE but has the added benefit of creating a higher density plasma which can create good etch profiles with less potential for damage during the etch process. ICP works by applying an electromagnetic signal through a coil of wire wrapped around the chamber that turns the gas molecules in the chamber into a plasma instead of relying solely on the RF signal applied to the target electrode.

ECR is also generally used in conjunction with RIE and produces an etch process very similar to RIE-ICP. The system, however, produces a high density plasma by using the principle that an electron when exposed to a uniform and static magnetic field will have circular motion due to the Lorentz force. Once again, a high density

plasma can be produced more efficiently, with less energetic ions required and thereby reducing the potential of unwanted damage during the etch process.

Pixels can also be etched using wet chemical etching. Typical recipes include phosphoric acid (H_3PO_4) or hydrochloric acid (HCl) based solutions. More details of the chemical solutions and recipes are given in appendix A. Chemical etching has the benefit of not requiring expensive and complicated vacuum systems and also do not damage the surface sidewalls of the detectors. However, they tend to be much less uniform than dry etching techniques.

3.3.2 Surface Passivation

Most detector fabrication procedures include some form of surface passivation or encapsulation. The word passivation is generally used to describe a coating on a material that not only protects the material but also has some chemical effect on the material surface to reduce or remove unwanted qualities like surface leakage current. The word encapsulation is also included to describe a coating that merely protects the material but is chemically inert. The primary reason passivation is required is that one of the biggest obstacles T2SL technology is surface leakage current. This current is thought to be due to surface defect states created during the pixel definition etching process which results in dangling bonds from mechanical damage induced by the plasma. This is one of the advantages wet etching has over dry etching. Other ideas include oxidation of the material surface upon exposure to ambient atmosphere that contribute to unwanted surface states as well. These defect states create electrical traps and thus an easy path for current to flow. Thus a good passivation material will protect against oxidation and resolve traps resulting from dangling chemical bonds. Research in passivation/encapsulation layers include silicon dioxide (SiO_2), silicon nitride (Si_3N_4), sulfide based materials, and polymer

materials such as polyimide and SU-8 photoresist [97, 70].

Dielectric passivation using SiO_2 or Si_3N_4 can be achieved by different methods with plasma enhanced chemical vapor deposition (PECVD) being one of the more common techniques. PECVD is better over regular chemical vapor deposition (CVD) techniques (which require temperature on the order of 1000°C) because of the lower temperatures (100°C - 300°C) required which would otherwise damage or destroy the detector material. The dielectric quality can further be increased by using a high density plasma system such as an ICP-PECVD (similar to the system used for etching). Another possible technique deposits the dieletric material by electron-beam evaporation. SiO_2 passivation for VLWIR T2SL detectors has been found to increase surface resistivity by a factor of 5 and more than double R_0A [98]. In another study, it was shown to decrease dark current density by a factor 6 [70] for LWIR TSL detectors. In that same study, Si_3N_4 was only shown to decrease dark current density by a factor 2.5.

Sulfide based passivation has had great success with various investigations and has been utilized in different techniques including zinc sulfide (ZnS) overgrowth, ammonium sulfide treatment (NH_4S), and electro-chemical passivation (ECP). for a LW T2SL PIN detector structure Plis et. al. [70] showed a decrease in dark current density by a factor of 25 for NH_4S and 200 for ECP. However, the ZnS passivation only reduced dark current by a factor of 3. Gin et. al. [99] obtained over 2 orders of magnitude decrease in dark current density for a LWIR PIN T2SL. However, sulfur based passivation has been shown to damage T2SL based detectors [100].

Polymer passivation recipes have also been studied which offer the advantage of being able to be easily integrated in the detector fabrication procedure. Initial results have been favorable for work with MWIR and LWIR T2SL detectors passivated or encapsulated with SU-8 [101, 69], a negative tone photoresist available from Micro-Chem^{TM}. A promising reduction in dark current density was also observed

for polyimide passivation [102].

Most of the detectors fabricated for study in this dissertation were passivated with SU-8 or SiO_2. Specific details will be given for the different studies described in later chapters.

3.3.3 Metal Contact Deposition

Ohmic electrical contacts are necessary to ensure correct device behavior and not impede the flow of photogenerated current. An ohmic contact is defined as a junction that is not rectifying and has linear current-voltage characteristics. non-ohmic contacts are required for some detector designs but for all the devices in this dissertation ohmic contacts were used. Ohmic contacts are created by different techniques including choosing a contact metal that has a work function that will not form a barrier for current, place a narrow band gap semiconductor material between the contact metal and device, or heavily dope the contact layer such that tunneling assisted carrier flow between the contact layer and metal takes place. The later technique has been the simplest and most successful technique for our devices.

Electrical contacts are created by depositing metal on the highly doped contact layers. Prior to deposition, samples are patterned with PR to mask the areas of the sample that do not need metal contacts. Deposition takes place by loading the sample inverted inside a vacuum chamber which is evacuated to pressures on the order of 10^{-7} Torr. Target metal sources that are facing up towards the detector sample are heated by a spatially oscillating electron beam to the point of evaporation. The deposition rate is monitored and is controlled by tuning the electron beam current flow.

A typical metal contact recipe used for highly doped narrow band gap T2SL material consists of a layer of titanium to make strong mechanical adhesion and

electrical contact, a layer of platinum to serve as a diffusion barrier to block the dissemination of the top metal atoms into the device, and a thick layer of gold to serve as the top metal to make electrical contact with external components.

Following metal deposition, a process known as "lift-off" is performed which consists of rinsing/soaking the metal covered sample in acetone so that the PR can be dissolved and metal will "lift-off" where the PR was and remain only in the desired locations. If a polymer based passivation technique, such as SU-8 described in the previous section, is not being used then the detector sample is completed and may be mounted for testing.

To test the samples, individual dies (chips with complete test structure sets) are cleaved and mounted on an LCC chip carrier with a thermally conductive epoxy. An example sample is shown in figure 3.5.

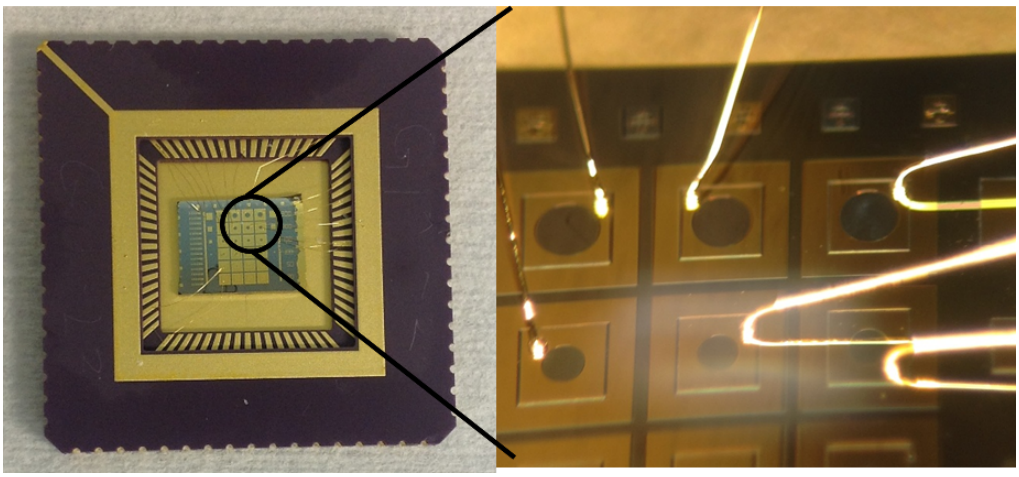

Figure 3.5: Single pixel test detector mounted and wire bonded inside a 68 pin LCC socket.

The LCC chip carrier used for the single pixel test structures have 68 pins and the LCC chip carriers used for FPA testing have 100 pins. Contacts on the samples are then wire bonded to the chip carrier and are now ready for testing.

3.4 Detector Characterization

Single pixel devices may be tested for contact resistance, dark current, photocurrent, surface leakage effects, spectral response, responsivity, and noise. For most of the these tests the devices are cooled by either a Janis-Research^{TM} cryostat with a closed cycle helium cryo-pump or a Janis-Research^{TM} liquid nitrogen cooled pour filled cryostat. The tests for the contact resistance and for surface leakage effects are conducted using a Janis-Research^{TM} liquid nitrogen cooled flow-through probe station.

3.4.1 Current-Voltage Characteristics

Current-Voltage (I-V) characteristics are measured using either a HP 4145B semiconductor parameter analyzer or a Keithley 236 source measure unit (SMU). For a p-n junction type devices, the N-side contact is grounded and the P-side contact is connected to the variable bias probe. Most of the detectors discussed within this dissertation are heterostructure devices based on the nBn or pBp configuration and do not follow the reverse bias/forward bias convention of a regular diode. As such, the orientation of the applied bias will be described for each case. Figure 3.6 shows a schematic of the I-V setup.

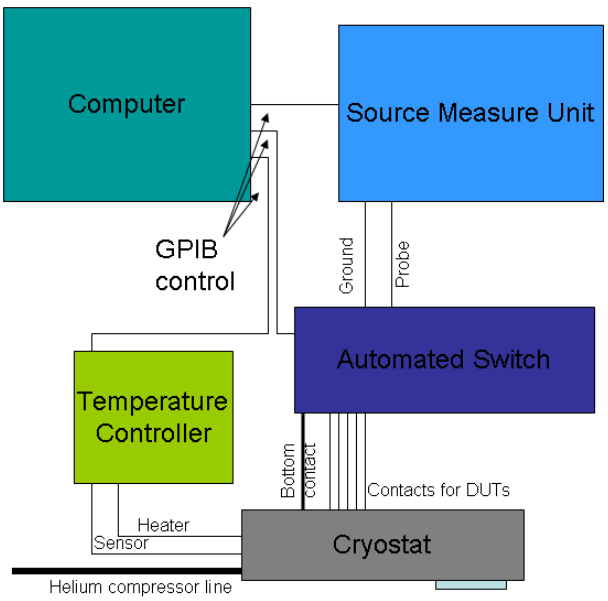

Figure 3.6: Current-Voltage setup schematic.

Contact Resistance

The contact resistance describes how good the ohmic contact is. It is determined by using the TLM patterns created in each test die during fabrication. The test structure consists of multiple contacts with varying separation distances on the same contact layer. An illustration is given in figure 3.7.

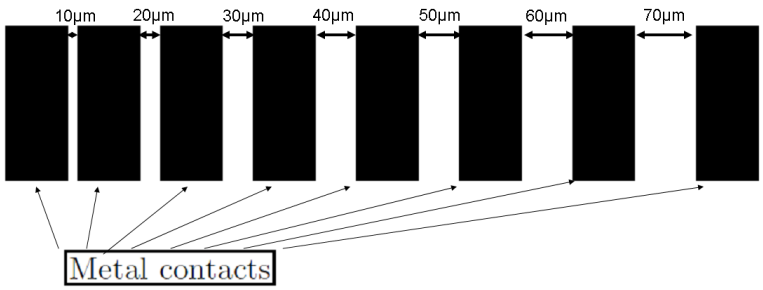

Figure 3.7: Transmission Line Method (TLM) metal contact with variable spacing for testing contact resistance.

The white background represents the semiconductor contact layer and the black patterns represent the metal contacts. These patterns are made on both the top and bottom contact layer. The distance between each contact varies slightly from one to the next. In our case the distance between the closest two is $10\mu m$ and the separation between each pair increases by $10\mu m$ with the largest separation being $70\mu m$. Current-voltages data is measured for each adjacent pair. If the I-V curve is linear then the contact is ohmic, however, if the curve is non-linear then some barrier exist between the metal contact and the semiconductor contact layer such as a Schottky barrier. For the linear curve case, the resistivity of the material can then be determined by taking the slope of the I-V curve for each contact pairs and plotting it against the separation distance for each pair. The material resistivity is then the slope of that curve. In mathematical terms, $Resistivity = \frac{d(dV/dI)}{dx}$. The resistivity determines the channel resistance, the resistance of the material between the contact pads. The y-intercept on the plot is then the contact resistance.

Dark Current

Dark current is a very important parameter to measure because it tends to be the limiting factor in a detector's performance. That is one of the reasons it is used in Rule 07 for estimating the performance of an MCT detector. Several mechanisms exist that contribute to dark current including processes from the bulk material as well as from surface states. This section will describe how dark current is measured and how the measurement can be varied for determining which dark current mechanisms are present.

Bulk material effects refer mechanisms due to material properties not dependent on the device processing. Some common mechanisms include Shockly-Read-Hall (SRH) generation-recombination (G-R) current, band-to-band (BTB) tunneling current, trap-assisted-tunneling (TAT) current, Auger recombination current and diffusion current. One technique for determining the dominant dark current mechanism is to measure dark current at several temperatures and then plot the data for some bias using an Arrhenius style plot in which the current is plotted on a logarithmic scale versus the inverse of temperature; specifically, $1/kT$, in which the slope of the line is in terms of energy. Mathematically the relation is $J = J_0 \times e^{-E_A/kT}$. The slope of the curve on the Arrhenius scale is then the activation energy which can provide clues about which current mechanism is dominating. For instance, if the activation energy is equivalent to the bandgap energy, the detector is diffusion limited. If it is on the order of one half of the bandgap, G-R current is most likely the dominant mechanism. Activation energies on the order of 10% or less than the band gap tend to be limited by tunneling current or surface leakage. Figure 3.8 graphically illustrates the mechanisms for SRH G-R, BTB, and TAT currents.

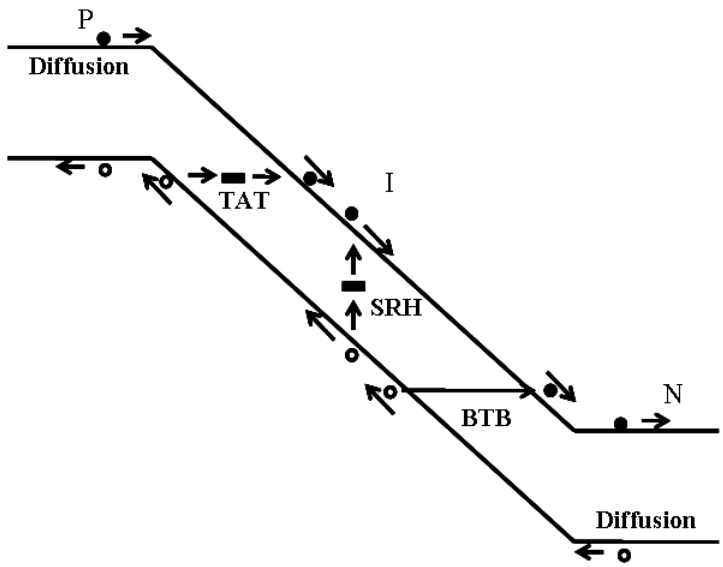

Figure 3.8: Illustrations of SRH generation-recombination current, band to band tunneling current, and trap assisted tunneling current in a narrow band gap p-i-n diode.

More detailed expressions for different current mechanisms are given in the following expresions; the first shown is for diffusion current, J_{diff}. Diffusion current is the process by which carriers move due to carrier concentration gradients across the device. Detectors are generally designed to have this as the limiting current mechanism. The expression of diffusion is shown in equation 6.2 from ref. [103].

$$J_{diff} = n_i^2(T)\sqrt{qk_BT}\left(\frac{1}{N_A}\sqrt{\frac{\mu_e}{\tau_e}} + \frac{1}{N_D}\sqrt{\frac{\mu_h}{\tau_h}}\right)(\exp\left(\frac{qV}{k_BT}\right) - 1) \tag{3.1}$$

Where $n_i(T)$ is the intrinsic carrier concentration, q is the electronic charge, T is temperature (K), k_B is Boltzmann's constant, N_A and N_D are the acceptor and donor doping concentration, μ_e and τ_e are the electron mobility and lifetime, μ_h and τ_h are the hole mobility and lifetime, and V is the externally applied bias.

SRH G-R current is a mechanism by which carriers (electrons and hole) recombine or are generated with the assistance of an energy state or trap place nearby the middle

of the semiconductor band gap. Thus, thermalized carriers have a higher probability of recombining if such a mid-gap trap energy level exists. These traps exist due to random defects within the semiconductor material. This mechanism is one of the biggest limiting factors in the performance of T2SL based detectors. The expressions for SRH current is shown in equations 3.2, 3.3 from ref. [104].

$$J_{SRH} = \frac{qn_iW}{\tau_{SRH}} \frac{2k_BT}{q(V_bi - V)} \sinh\left(\frac{qV}{2k_BT}\right) f(b) \tag{3.2}$$

$$f(b) = \int_0^\infty \frac{1}{u^2 + 2bu + 1} du, b = \exp\left(-\frac{qV}{2k_BT}\right) \cosh\left(\frac{E_t - E_i}{kT}\right) \tag{3.3}$$

Where W is the depletion width, τ_{SRH} is the G-R lifetime, V_{bi} is the built-in potential, E_i is the intrinsic Fermi energy level, and E_t is the trap energy level.

BTB tunneling current is the current induced by carriers tunneling across the junction due to the applied bias and built-in potential of the depletion region. For T2SL based detectors this current process is reduced, as compared to HgCdTe based detectors, due to a large electron effective mass. The expression is given in equation 3.4 from ref. [103].

$$J_{BTB} = \frac{q^3F(V)V}{4\pi^2\hbar^2} \sqrt{\frac{2m_T}{E_g}} \exp\left(-\frac{\sqrt[4]{2m_TE_g^3}}{3q\hbar F(V)}\right) \tag{3.4}$$

Where m_T is the reduced tunneling effective mass, E_g is the bandgap, and F(V) is the electric field as a function of voltage. TAT tunneling current is a similar mechanism but is helped by trap energy levels within the band gap similar to SRH G-R current. The expression for which is given in equation 3.5 from ref. [103].

$$J_{TAT} = \frac{q^2 m_T V M^2 N_t}{8\pi\hbar^3 (E_g - E_t)} \exp\left(-\frac{\sqrt[4]{2m_T (E_g - E_t)^3}}{3q\hbar F(V)}\right) \tag{3.5}$$

Where M is the transition matrix element associated with the trap and N_t is the trap density .

Surface leakage current results from imperfections on the detector sidewall which result in surface energy states that provide paths for current to flow. This mechanism of dark current can be especially detrimental to devices with small areas such as high density FPAs in which the perimeter to area ratio is quite high. To measure the effect of surface leakage current pixels with varying areas are fabricated and tested in an I-V setup. Devices with small areas (diameter or side length $< 100\mu m$) are often difficult to wire bond and if a test structure design did not include an extended enlarged pad for wire bonding, the detector requires a probe station for testing. Figure 3.9 illustrates a cryogenic probe station setup. The data is analyzed by plotting the current density as a function of function of area. If the current density increases as the area decreases, then surface leakage is a dominant effect for small area pixels. Another common method of analyzing such data is to plot the current density as a function of the perimeter/area ratio. For small pixels, the ratio of the perimeter to area is large. Thus, the perimeter sidewalls can contribute significantly to dark current if the pixel sidewalls suffer from surface energy states leading to surface leakage current.

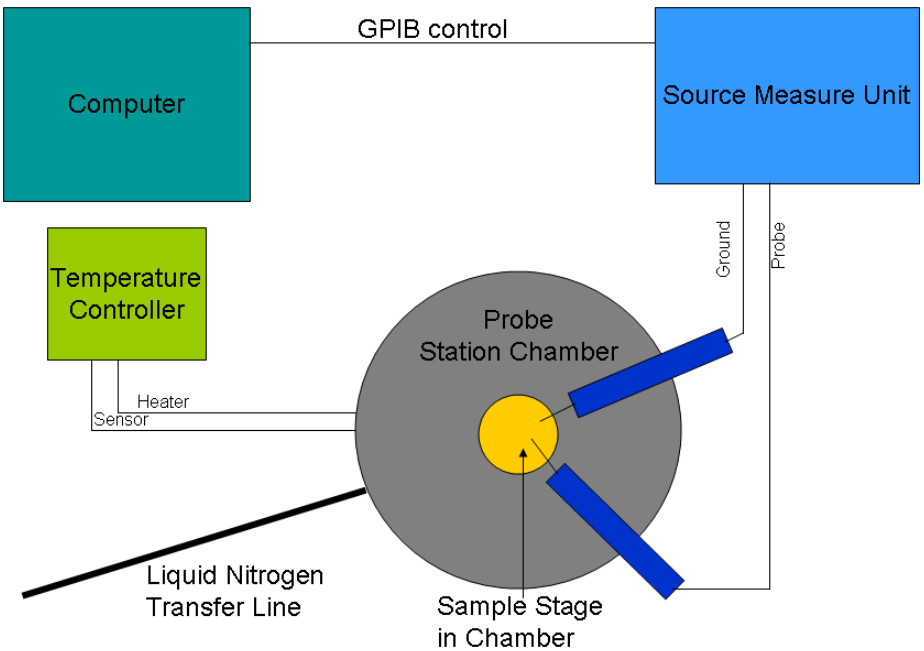

Figure 3.9: Cryogenic probe station setup schematic.

3.4.2 Spectral Response

The spectral response of a detector typically shows a curve describing the photoresponse of a detector with respect wavelength normalized to the maximum or peak detection wavelength. This can be used with responsivity (described in the next section) to show the calibrated responsivity as a function of wavelength. The measurement is conducted by utilizing a fourier transform infrared (FTIR) spectrometer with the detector under test (DUT) connected as an external detector. Initially a background scan is measured using a calibrated detector installed in the FTIR which is then used to normalize the response spectrum of the DUT. The difference in frequency response of the two detectors must also be taken into account. The DUT can be cooled using either a LN_2 pour filled cryostat or a cryostat cooled with a closed cycle helium cryopump. Below, in figure 3.10, is an illustration of the spectral response setup. More details are given in the appendix.

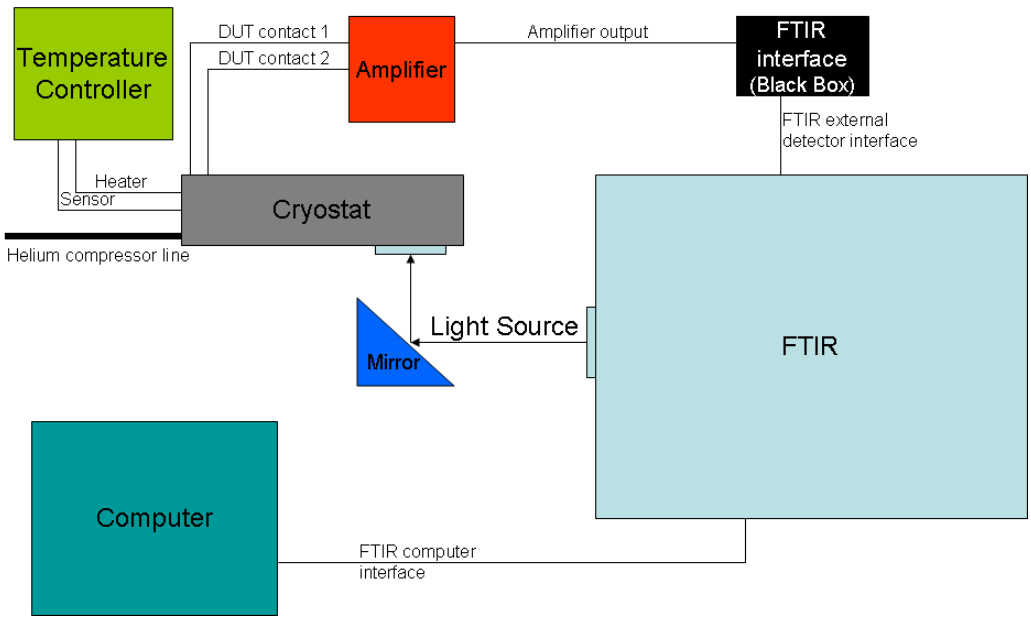

Figure 3.10: Spectral Response setup schematic.

3.4.3 Responsivity

Responsivity is a measure of the output electrical response of a DUT given some input photon flux. the measurement is conducted using a calibrated black body source, optical band pass filters, an optical chopper, a network analyzer or lock-in amplifier, a voltage amplifier, and a cryostat. A detector is cooled in a cryostat and between it and the black body is placed the optical chopper and optical filter. The voltage amplifier is used to strengthen the detector signal as well as apply a bias across the DUT. The signal is then fed to the spectrum analyzer where the signal is measured. The responsivity is calculated using the following formula:

$$R_\lambda = \frac{I}{A_{BB} \times \frac{A_{det}}{r^2} \times \int_0^{\lambda_{cut}} M_{e,\lambda}(\lambda, T) \times NR(\lambda)\, d\lambda} \tag{3.6}$$

Where $R_(\lambda)$ is the wavelength dependent responsivity, I is the amplitude of the signal measured by the network analyzer, $A_(BB)$ is the area of the black body aperture, A_det is the detector aperture area, r is the distance between the detector and black body, $\lambda_(cut)$ is the cut-off wavelength of the detector, $M_(e, \lambda)$ is the black body spectral radiance as a function of wavelength and temperature, $NR(\lambda)$ is the normalized spectral response, and λ is wavelength. Bias dependent responsivity can provide clues concerning the size of barriers in the bandstructure of the DUT as well as indicate the quantum efficiency (QE). A more general expression for responsivity is given in the next formula:

$$R_\lambda = \frac{G\eta\lambda}{hc} \tag{3.7}$$

Where G is gain, η is quantum efficiency, h is Planck's constant, and c is the speed of light. From this the gain*QE product can be calculated. A schematic of the responsivity setup is shown in figure 3.11.

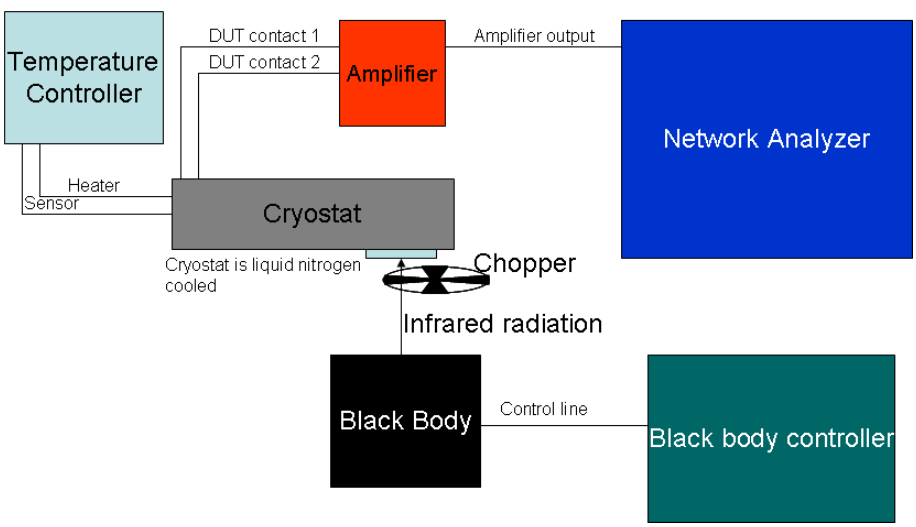

Figure 3.11: Responsivity setup schematic.

3.4.4 Noise

Noise is a measure of the random electrical sources in the DUT signal that compete with the actual photoresponse signal. There are numerous causes that stem from sources internal to the DUT such as SRH G-R and surface leakage current, and external sources such as system noise from the amplifier. Because of so many potential noise sources in the measurement setup, noise is a difficult parameter to measure and is often estimated from dark current measurements. The measurement utilizes a spectrum analyzer, a voltage amplifier, and cryostat. Dark noise can be measured if a cold shield is placed in front of the DUT or a 300K ($\sim$ room temperature) background noise can be measured if no shield. A black body can also be utilized to measure background limited noise. An illustration of the noise measurement setup is shown in figure 3.12.

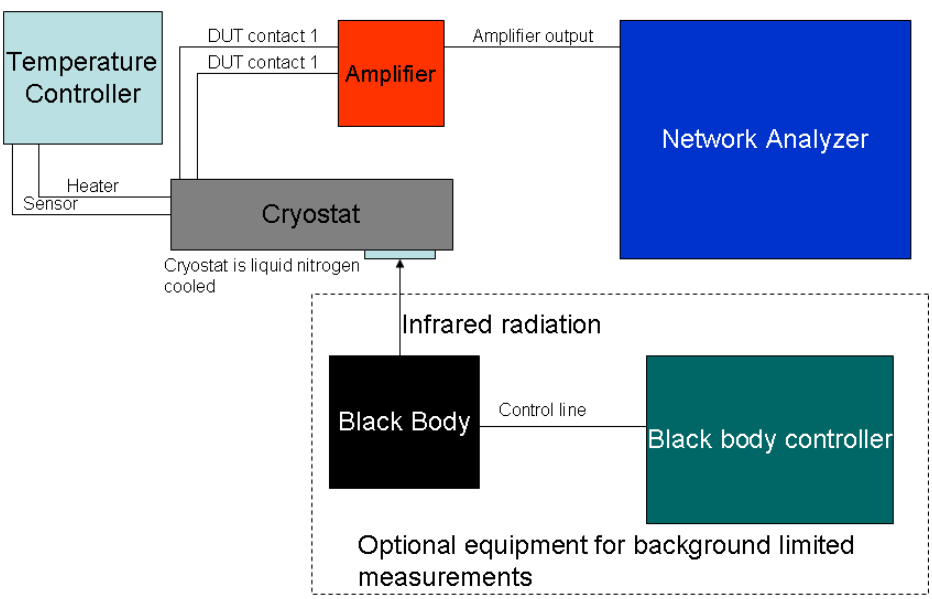

Figure 3.12: Noise setup schematic.

Once the noise is determined, it is used to calculate such quantities as noise-equivalent-power (NEP) and detectivity. The expression for calculating specific de-

tectivity (D*) using noise measurements is shown below.

$$D* = \frac{R_\lambda \sqrt{A\Delta f}}{i_{noise}} = \frac{\sqrt{A\Delta f}}{NEP} \tag{3.8}$$

Where R_λ is responsivity, A is the detector area, and δf is the frequency bandwidth of the noise measurement. Alternatively, D* can be estimated using dark current density as shown below [15].

$$D* = \frac{R_\lambda}{\sqrt{2qJ + 4kT/R_D A}} \tag{3.9}$$

Where J is the dark current density and R_D is the dynamic resistance which is the inverse of the slope of the I-V curve at the detector's operating bias. The first term in the denominator represents shot-noise and the second represents Johnson-noise.

3.5 Summary

In this chapter I have described the tools that were used to conduct to the research for this dissertation. The primary tools include equipment for detector fabrication and characterization. Single pixel detectors were fabricated using standard techniques including optical photolithography, wet chemical and dry etching, PECVD SiO_2 and Si_3N_4, SU-8 lithography, and electron beam metal evaporation. Characterization techniques include transmission measurements, variable temperature I-V measurements, spectral response, responsivity, and noise measurements.

Chapter 4

MWIR InAsSb nBn Detectors

This chapter will discuss basic characteristics of $InAs_{(1-x)}Sb_{(x)}$ based nBn detectors with an $AlAs_{(1-x)}Sb_{(x)}$ barriers. The first section will describe the detector designs and discuss growth and fabrication details. The second section will present the characterization results. Finally, the results will be summarized in the third section along with concluding remarks.

4.1 Detector Designs and Fabrication Details

The variables at play in the design of InAsSb nBn detectors include composition and doping conditions of the absorber, contact, and barrier. Such variations have been outlined by Klipstein et. al. [7]. In this study we investigate the parameters related to the barrier conditions including two different compositions of the AlAsSb used for the barrier as well as two different doping conditions making for a total of four samples under investigation. Tolerable lattice mismatch being the primary constraint on the material composition. Another design was also tested that used an AlGaSb barrier layer, however, this device had very high dark current that behaved linearly

with bias like a photoconductor. It was concluded the valence band of the AlGaSb barrier was sufficiently high as compared to the conduction band of the absorber and contact layer such that tunneling across the barrier junction was taking place; so this design was excluded from further study.

The structures for this study were grown by Intelli Epi^{TM} and IQE^{TM} using solid source molecular beam epitaxy (MBE) on Te-doped epi-ready (100) GaSb substrates. The two structures grown by Intelli Epi^{TM} consisted of a 1000nm thick $InAs_{0.91}Sb_{0.09}$ (lattice matched to GaSb) bottom contact layers doped with silicon at a concentration of $1 \times 10^{18} cm^{-3}$. Next a 3000nm thick $InAs_{0.91}Sb_{0.09}$ n-type absorber layer with a doping concentration (n-type) of $1 \times 10^{17} cm^{-3}$ was grown. This was followed by a 100nm thick AlAsSb barrier layer grown using the digital alloy technique (alternating layers of AlAs and AlSb, similar to superlattice). The barrier is non-intentionally doped and is estimated to be p-type with an acceptor concentration on the order of $10^{15} cm^{-3}$ [105]. A 300nm thick n-type InAsSb layer, with the same parameters as the absorber, was then grown to create a top contact and this was followed by a 10nm InAs capping layer (n-type, $1 \times 10^{18} cm^{-3}$). Silicon was used as the doping material. The difference between the two structures is the composition of the barrier region in which for structure A the As/Sb ratio is 0.15/0.85 and for structure B the As /Sb ratio is 0.10/0.90. In terms of the digital alloy, the composition corresponds to 3 monolayers (MLs) of AlAs and 17 MLs of AlSb for structure A, and 2 MLs of AlAs and 18 MLs of AlSb for structure B. The two structures grown by IQE^{TM} were similar, however, the doping material used was tellurium instead of silicon and the barrier region was doped with a concentration of $1 \times 10^{17} cm^{-3}$. For this study sample C will correspond to the IQE^{TM} sample with a barrier As/Sb ratio of 0.15/0.85 and sample D will correspond to the IQE^{TM} structure with a barrier As/Sb ratio of 0.10/0.90. These structures are summarized in figure 4.1.

The crystalline quality was evaluated for structures A and B with X-ray diffrac-

tion (XRD) measured in a Philips double-crystal X-ray diffractometer using the Cu K-α_1 line. The XRD data for both structures is shown in figure 4.2. The lattice mismatch of the $AlAs_{(1-x)}Sb_{(x)}$ barrier of structure A was 0.97% with respect to the GaSb substrate whereas the barrier of structure B had a lattice mismatch of 0.17%. The lattice mismatch for sample C and D are should be similar to A and B, respectively.

Structure	Barrier Composition	Barrier Doping
A*	$AlAs_{0.15}Sb_{0.85}$	**p ~ $1 \cdot 10^{15}$ cm^{-3}
B*	$AlAs_{0.10}Sb_{0.90}$	**p ~ $1 \cdot 10^{15}$ cm^{-3}
C†	$AlAs_{0.15}Sb_{0.85}$	n = $1 \cdot 10^{17}$ cm^{-3} Doping compensation
D†	$AlAs_{0.10}Sb_{0.90}$	n = $1 \cdot 10^{17}$ cm^{-3} Doping compensation

J.A. Lott, et. al., Appl. Phys. Lett. **56 (13), 1242-1244 , 1990.

*Samples grown by Intelli Epi™
†Samples grown by IQE™

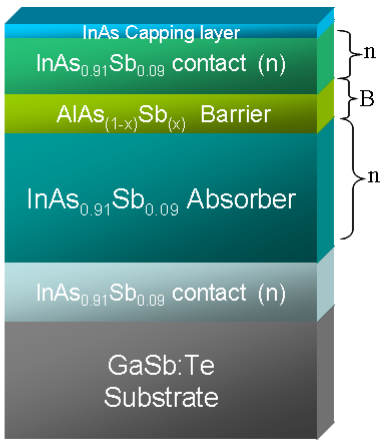

Figure 4.1: MWIR InAsSb nBn detector structure and table with detailed descriptions of the four different samples [12].

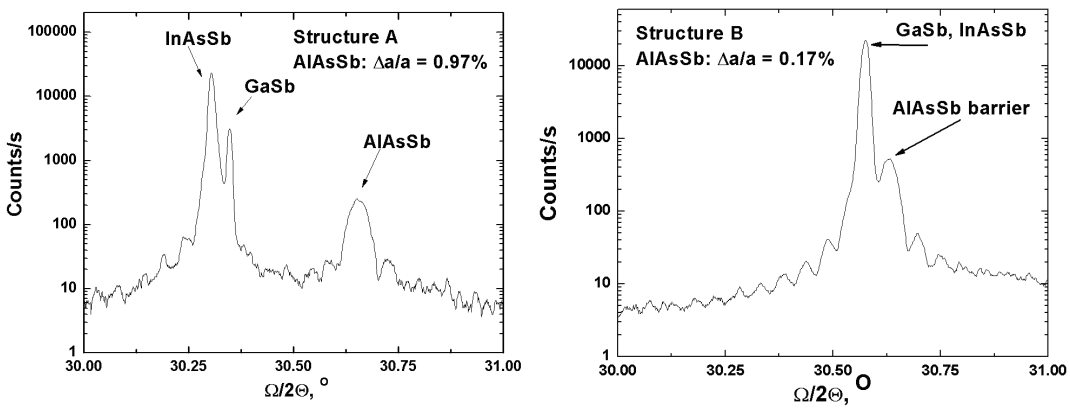

Figure 4.2: X-Ray diffraction of structure A and B [12].

Single pixel devices with square mesas of 410 x 410 μm^2 and apertures with diameters ranging from 25μm to 300μm were fabricated from the structures. The processing utilized standard optical photolithography, for definition of the top contact mesas, followed by a shallow etch in a phosphoric acid solution to the barrier region. Then another photolithography step was performed to define deep etch regions for obtaining access to the bottom contact. This deep etch was conducted using inductively coupled plasma (ICP) dry etch with BCl_3. An additional photolithography step was utilized to define regions for deposition of metal contacts. Metallization was performed using an e-beam evaporator with a metal composition of Ti/Pt/Au (500/500/3000 Å). This was then followed by passivation of the mesa side walls with SU-8 photoresist.

For this study we focused on the effect of the barrier composition and the barrier doping concentration on InAsSb nBn detectors. The barrier composition affects characteristics such as lattice mismatch, band-gap, electron affinity, and valence and conduction band offset. The doping concentration will affect such characteristics as the Fermi energy level and consequently the amount of depletion between the barrier region, contact and absorber regions.

4.2 Results and Discussion

Various characteristics of the devices were then measured and compared. The measurements conducted include: spectral response, dark current as a function of applied bias for temperatures ranging from 77K to room temperature, variable temperature responsivity and variable temperature specific detectivity as a function of bias.

4.2.1 Dark Current

Variable temperature measurements of dark current were conducted for the four devices and the Arrhenius behavior was then plotted in order to analyze the current limiting mechanisms. The temperature was varied from 50K to 290K with 10K temperature steps, however, for the low temperature region the current was below the minimal current reading capability of the system. Dark current as function of bias at a temperature of 150K is shown in figure 4.4 and variable temperature dark data for an applied bias of 0.2V is presented in figure 4.3. An applied bias of 0.2V was chosen because the responsivity achieved roughly 90% of the saturated value at this bias.

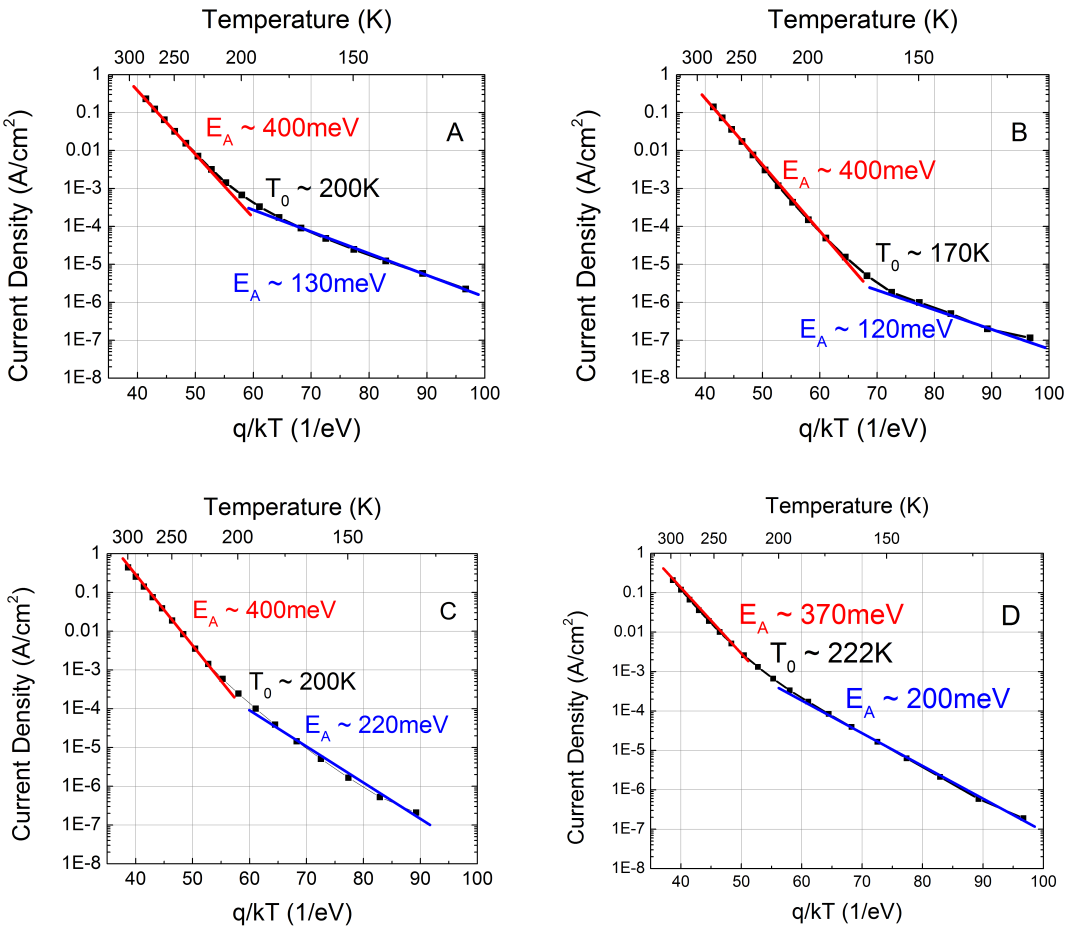

Figure 4.3: Dark current plotted on Arrhenius scale for the four detector structures. The activation energy for the high temperature and low temperature regions are indicated along with the transition temperature.

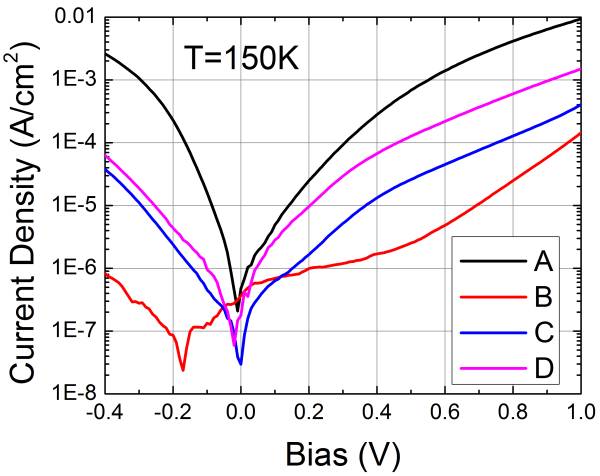

Figure 4.4: Dark current for all four nBn detectors at 150K as a function of bias.

The data does not indicate diffusion limited behavior for all temperature ranges as indicated from the lack of a constant slope. Structure A, B, C, and D show diffusion limited performance from room temperature down to 200K, 170K, 200K, and 222K, respectively. The activation decreases below these transition temperatures indicating each detector is G-R limited for low temperature operation. Structure B has the lowest dark current density and transition temperature. The dark current density for structure B at 150K is $9.93 \times 10^{-7} A/cm^2$ which is on the same order of magnitude of a HgCdTe detector of similar cut-off wavelength according to Rule 07 [4].

The dark current of structure B is markedly decreased compared with A. This could be due to a couple of different factors. The band alignment and doping conditions may be in a more suitable state in structure B such that there is less band bending and depletion and consequently less G-R current. Compared with structure A, the higher Sb concentration in structure B provides a smaller band gap, slightly increased electron affinity, and smaller lattice mismatch with GaSb [106, 107]. This should result in raising the valence band position by only $\sim 20meV$ [106]. Another

explanation is the possibility of decreased G-R current due to a decreased trap center density because of the smaller lattice mismatch which would have a lower probability of the formation of defect sites.

Devices C and D show decreased dark current density with respect to device A, however both of them have higher dark current than device B. The difference between the first two versus the second two is the n-type tellurium doping in the barrier layer. This means the band alignment of the barrier is shifted down with respect to the absorber and contact. The G-R current does not appear to be significantly increased compared to structure B, so the size of the depletion does not appear to be significantly changed with doping conditions. Another factor to consider is that the cold shield during the measurement may be at a slightly higher temperature than the detector itself. Thus the current measurement may be influenced by the back ground radiation, small as it may be, coming from the cold shield. A detailed look at the bias dependent responsivity will provide more clues in the band alignment of the detectors.

4.2.2 Photoresponse

The spectral response, a necessary component for calculating responsivity, was measured for multiple temperatures from 77K to 290K. The normalized spectral response of the four devices measured at 77K and 150K is presented in figure 4.5. It is noted that the peaks of structure A and B are blue shifted as compared to structure C and D, however, the 0% cut-off wavelength is about the same. The softened slope of the cut-off wavelength is attributed to some mechanism akin to the Moss-Burstein effect [108] which requires that for highly doped semiconductors, absorbed photons must excite electrons to energy states above the minimum of the conduction band.

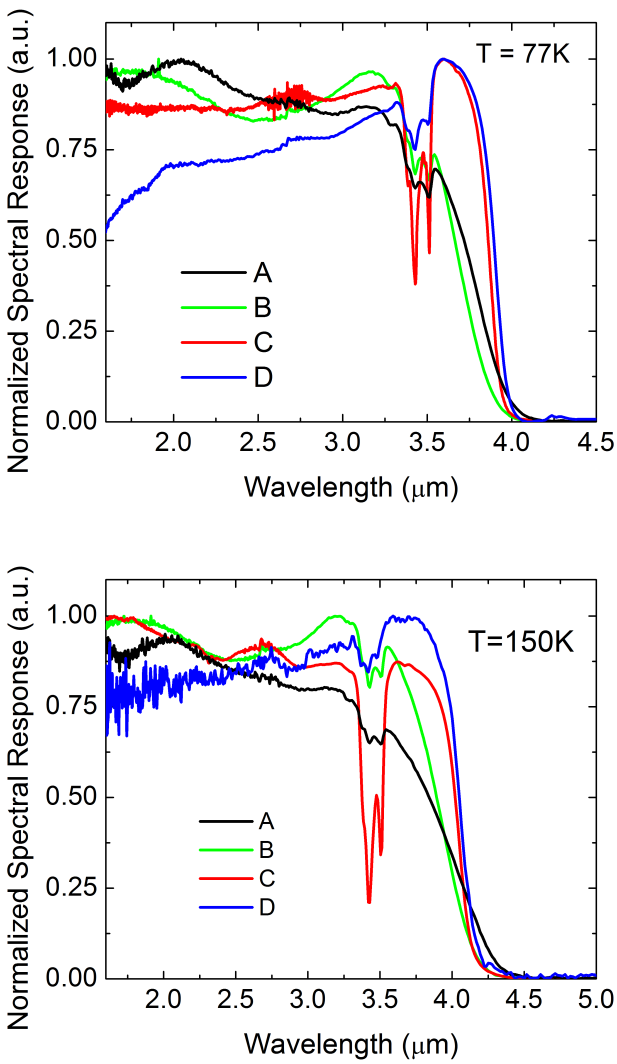

Figure 4.5: Normalized spectral response of the four detectors at 77K and 150K.

The responsivity was measured for biases ranging from 0 to 1.0V and temperatures ranging from 77K to 290K. The variable temperature responsivity data as a function of bias for the four devices are shown in figure 4.6. We see that structure A had the lowest responsivity and had little temperature variation at high bias ($> 0.2V$). Structure C had the largest responsivity for the measured temperature range and structure D had the most variation with temperature which was close to

30% in the saturated signal range. One of the more prominent differences amongst the four detectors is that the responsivity for structure A and B is significantly lower than it is for structure C and D. We see the signal saturate for all four detectors so it is not a matter of a applying enough bias to overcome a barrier. In fact, the saturation bias is roughly 200mV for all four detectors so the valence band barrier does not seem to vary much from one design to the next. However, the responsivity for each detector was calculated at $3.6\mu m$, which is the peak wavelength for detectors C and D, so the blue shifted peaks of detector A and B is one factor that contributes to the decreased photo-response.

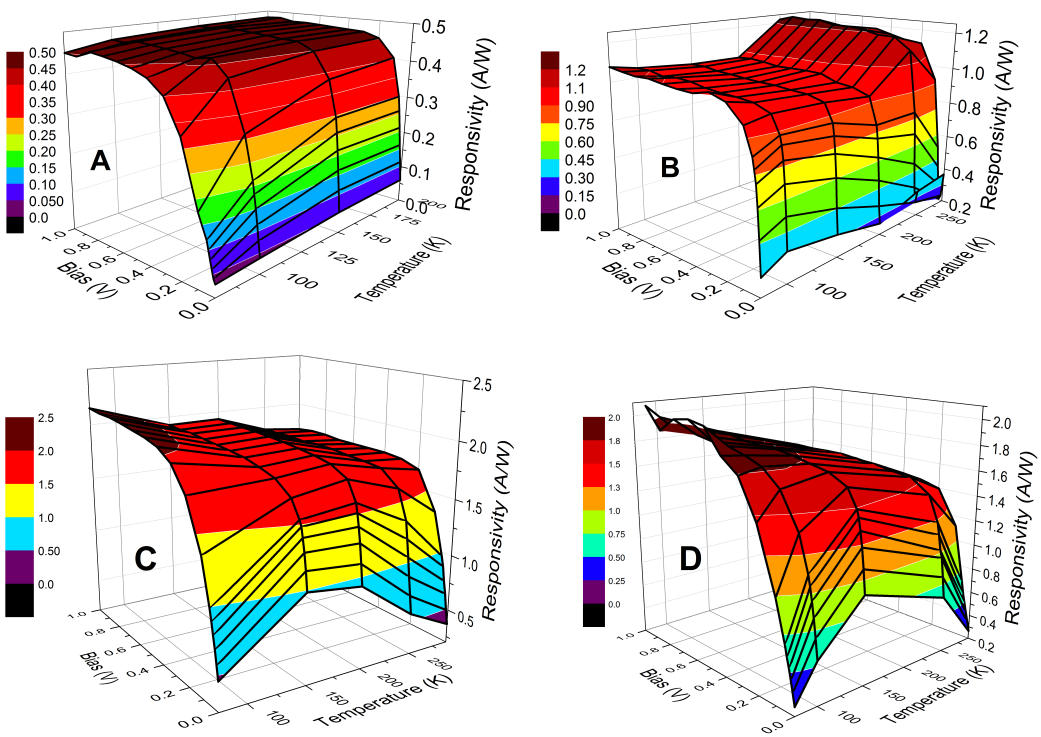

Figure 4.6: Variable temperature responsivity as a function of bias for all four detectors.

Another interesting difference is observed in the temperature variation. For the structures doped with silicon, A and B, the saturated signal is relatively stable with

increasing temperature, aside from the anomalous spike in signal for detector B. However, for the structures doped with tellurium, C and D, the signal deceases with increasing temperature. This along with the fact that the signal strength is significantly smaller than C and D suggests that the doping material has a significant effect on the the behavior of the device. However, it is acknowledged that other potential variables exist given that these detectors are grown in different MBE chambers by two different companies.

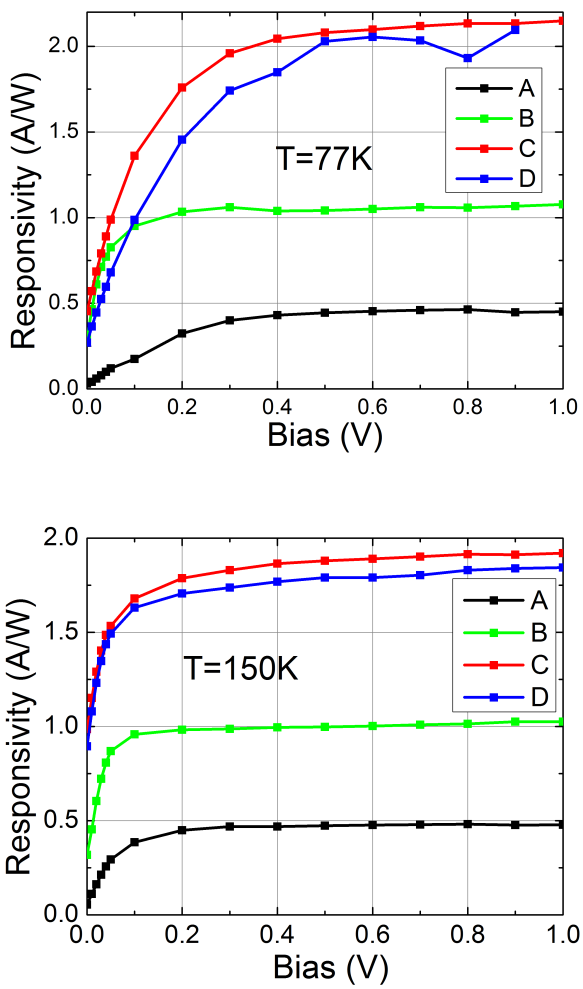

Figure 4.7: Bias dependent responsivity for 77K and 150K for all four detectors.

In figure 4.7 we see a comparison of the bias dependent responsivity for all four detectors at 77K and 150K. It is interesting to note that at 77K the bias dependence is fairly different for detector B as compared to the others. For instance, detector B is roughly saturated with a bias of 200mV where as the others require a bias of 400mV. However, at 150K detector B is saturated by 100mV and the other three are saturated by 200mV. Thus, all four detectors appear to have a temperature dependent turn on bias. There is going to be a barrier for all four detectors due to the top contact which is heavily doped compared to the absorber; so some bias will be required to overcome this. One of the goals is to minimize this required bias.

Assuming unity gain for these devices, quantum efficiency was calculated for a temperature of 150K and an applied bias of 0.2V. for devices A, B, C, and D they are 16%, 34%, 62%, and 59% respectively. The estimated QE for an InAsSb absorber $3\mu m$ thick is $\sim 70\%$ [109, 82] which implies the photoconductive gain or collection efficiency is reduced.

4.2.3 Detectivity

The specific detectivity for structures A, B, C, and D are shown in figure 4.8 as a function of bias for temperatures ranging from 150K to 290K. At the time of testing, structure A did not produce a signal above 200K. D* was calculated using dark current density to estimate Johnson and shot noise, as described in chapter three, because of difficulties in accurately measuring the actual detector noise.

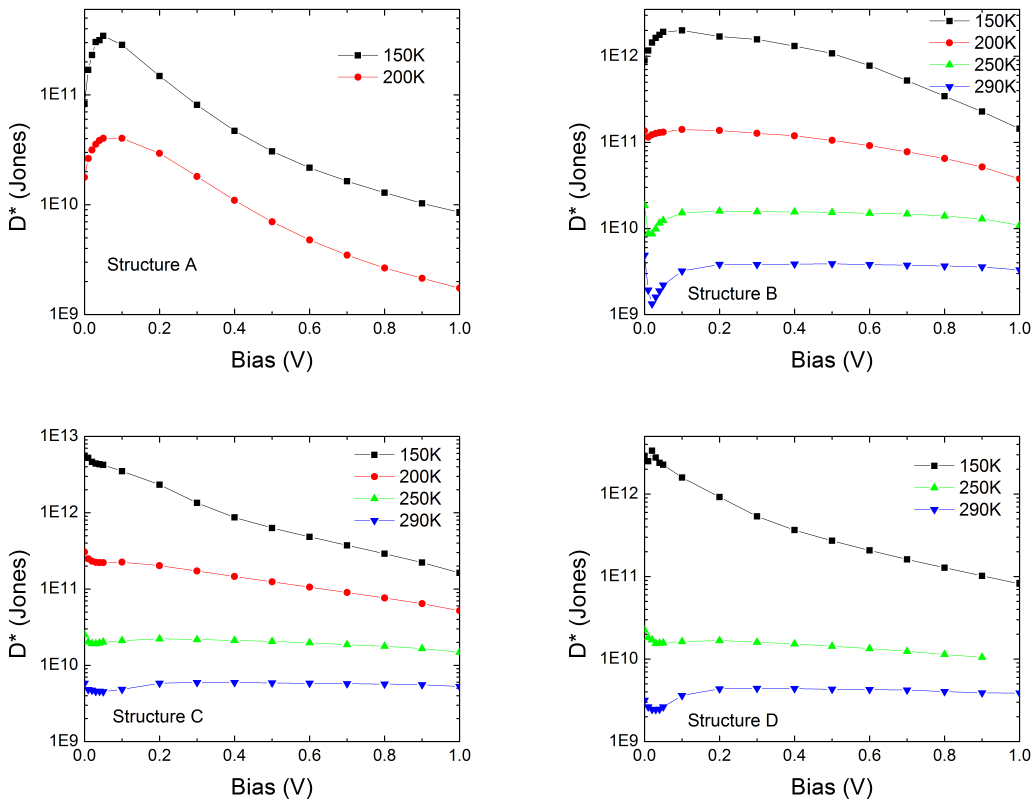

Figure 4.8: Variable temperature specific detectivity as a function of bias for all four detectors.

Of the three devices, structure C has the best D* performance with a value of 2.33×10^{12} Jones at an applied bias of 0.2V, wavelength of $3.6\mu m$, and operating temperature of 150K. Structure B was very close with a D* of 1.69×10^{12} Jones for the same parameters. If the peak response of detector B was not blue shifted, it would have performed better than structure C.

4.3 Summary

In this work we have presented the performance results of InAsSb based nBn MWIR detectors with AlAsSb barrier regions with different compositions and doping conditions. The data from this study is summarized in table 4.1 for an operating temperature of 150K with an applied bias of 0.2V.

Table 4.1: MW InAsSb detector summary

Structure	A	B	C	D
Responsivity (A/W)	0.45	0.98	1.79	1.70
Quantum Efficiency	0.16	0.34	0.62	0.59
Specific Detectivity ($cm\sqrt{Hz}/W$, Jones)	1.49×10^{11}	1.69×10^{12}	2.33×10^{12}	9.21×10^{11}
Dark Current Density (A/cm^2)	2.65×10^{-5}	9.93×10^{-7}	1.65×10^{-6}	6.31×10^{-6}
Activation Energy (eV)	0.37	0.4	0.4	0.37
Diffusion Limited Temperature (K)	200	170	200	222

The best performance based on D* results was achieved by structure C which had an n-type doped barrier region and a barrier composition of $AlAs_{0.15}Sb_{0.85}$. Detector B actually had a lower dark current density but had a slightly reduced D* in comparison with detector C because of a blue shifted response peak that was observed in detectors A and B which was attributed to the silicon dopant. All four detectors required an applied bias to achieve the maximum responsivity which varied with temperature suggesting a temperature dependent barrier in the valence band.

Detector B required the smallest bias out of the four. The variation between the two different barrier compositions did not significantly affect device performance except for in the case of detector A which was attributed to increased G-R current created by potential defects induced from the larger lattice mismatch compared to detector B. This behavior, however, was not observed in detector C which had the same barrier composition as detector A.

Chapter 5

MWIR T2SL nBn Detectors

5.1 Detector Designs and Fabrication Details

An important factor effecting the electrical and optical performance of narrow band gap IR detectors is the background carrier concentration [110]. In this chapter we look at electrical and optical performance of a mid-infrared T2SL based nBn detector with different doping concentrations in the absorber region. This is done to systematically optimize the n-type carrier concentration in the absorber layer. P-type doping was not considered since it would contribute to the creation of a depletion region.

The detector structures were grown in a VG-80 molecular beam epitaxy (MBE) system equipped with Ga/In SUMO^{TM} cells and valved cracker sources for group V Sb_2 and As_2. Details of the growth conditions have previously been reported [111]. The growth substrates were n-type (Te-doped) GaSb (100) epi-ready substrates. Initially $\sim 0.36\mu m$ thick n-type SLS contact layer composed of 170 periods of 10 monolayers (MLs) of Si-doped InAs and 10 MLs of n.i.d. GaSb was grown. This was followed by $\sim 1\mu m$ thick absorber layer of the same SLS composition but with different doping conditions. A 100 nm thick n.i.d. (p-type) $Al_{0.2}Ga_{0.8}Sb$ layer was

grown to create the barrier. This was followed by a 20 nm n.i.d. GaSb spacer layer and capped by a $\sim 0.1\mu m$ thick top contact layer composed of the same SLS as the bottom contact layer. Four samples of this structure were grown with different doping concentrations in the absorber region. These concentrations, determined by Hall measurements, were $5 \times 10^{16} cm^{-3}$ (n.i.d. SLS material), $1.4 \times 10^{17} cm^{-3}$, $4.0 \times 10^{17} cm^{-3}$ and $3.5 \times 10^{18} cm^{-3}$. The hall measurements were conducted prior to making the actual detector structures in which four samples were created with thin T2SL layers grown on semi-insulating GaAs substrates with different tellurium source temperatures. These samples were then mounted and wired in a van der Pauw configuration for hall measurements. The calibrated tellurium source temperatures were then used to dope the absorber layer. A schematic of the structure is presented in figure 5.1. The lattice mismatch, full width at half maximum (FWHM) of the 1st SLS satellite peak, and SLS period as a function of the doping concentration is shown in figure 5.2. The samples were processed using standard photolithography and inductively coupled plasma (ICP) etching techniques into single-pixel detectors with $410\mu mx410\mu m$ mesas with optical apertures varying in diameter from $25\mu m$ to $300\mu m$.

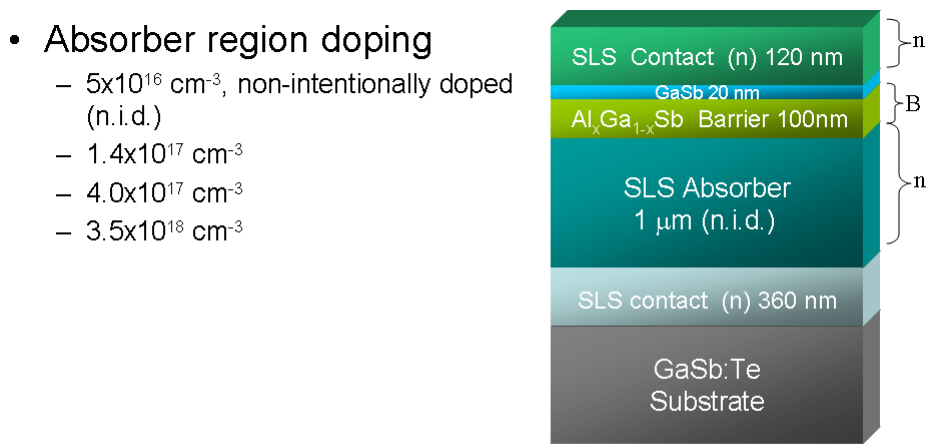

Figure 5.1: MWIR T2SL nBn detector structure with four different doping concentrations.

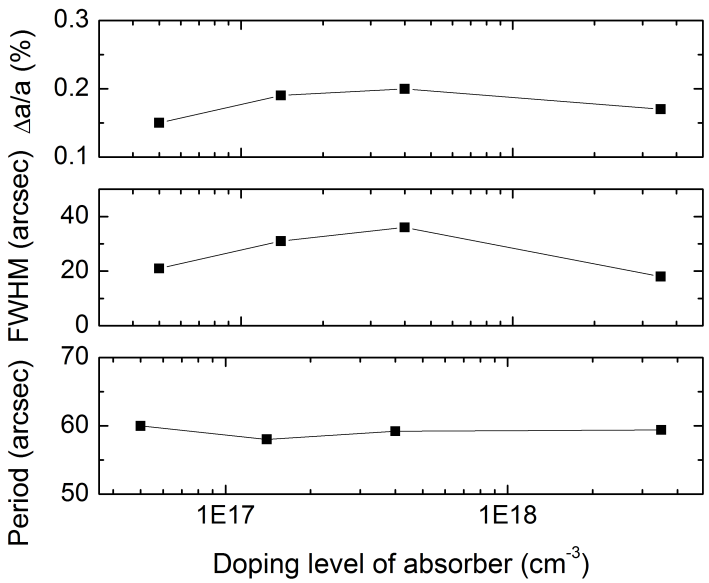

Figure 5.2: X-ray diffraction results showing lattice mismatch, FWHM, and period spacing as a function of the absorber doping concentration.

The processed devices were then characterized to determine their dark current

density, spectral response, responsivity and specific detectivity.

5.2 Results and Discussion

5.2.1 Dark Current

Current-voltage (IV) characteristics were measured for the devices at 77K as shown in Figure 5.3. It should be noted that the forward bias in this study was defined as a positive voltage applied to the bottom contact of the device with respect to the top contact. At 77K and 0.1V of applied bias, the dark current density increases by three orders of magnitude (from $\sim 0.3mA/cm^2 to \sim 0.3A/cm^2$), when the doping concentration is changed from $5 \times 10^{16} cm^{-3}$ to $3.5 \times 10^{18} cm^{-3}$. For a conventional p-i-n photodiode design made of a similarly narrow band gap material, increasing the absorber doping above $10^{16} cm^{-3}$ would result in a very thin depletion region and Zener breakdown [82], which is not necessarily the case for the unipolar nBn detector device. We believe that this increase in the dark current suggests that there is a quantum well (QW) for the minority carriers (holes) formed in the valence band. With an increase in the doping level of the absorber the depth of this QW increases. We think, during the device operation holes may be trapped in the QW whereas electrons are accumulated near the barrier. This leads to an enhanced electron-hole recombination similar to BTB tunneling. Thus, for the higher doped absorber region the carrier lifetime will be decreased due to the increase in electron-hole recombination. Since dark current is inversely proportional to the carrier lifetime, the increase in dark current density is expected and observed for the higher doped devices.

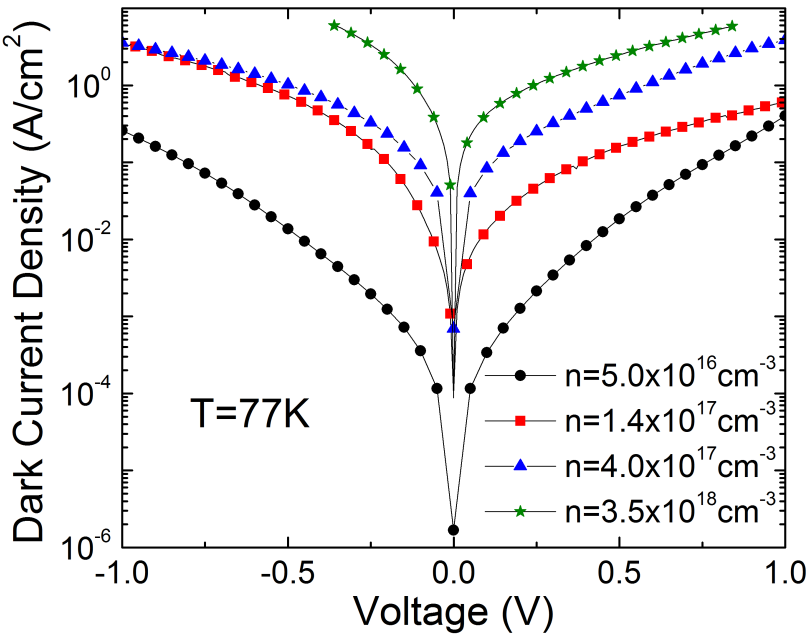

Figure 5.3: Dark current density of the four detectors.

Dark current density as a function of temperature was also measured for the detector with the n.i.d. absorber is plotted on an Arrhenius scale shown in figure 5.4. The activation energy for the high temperature range is $146meV$ which is close to half the expected band gap energy for the MWIR T2SL indicating the detector current is G-R limited. The $25.9meV$ activation energy at the lower temperature range indicates the detector current is limited by tunneling. The increased G-R and tunneling may be a result of the potential well formed by the mis-alignment of the absorber and barrier as described earlier. Such a situation is illustrated in the band structure simulation in $nextnano^{3TM}$, courtesy of Elena Plis, shown in figure 5.5.

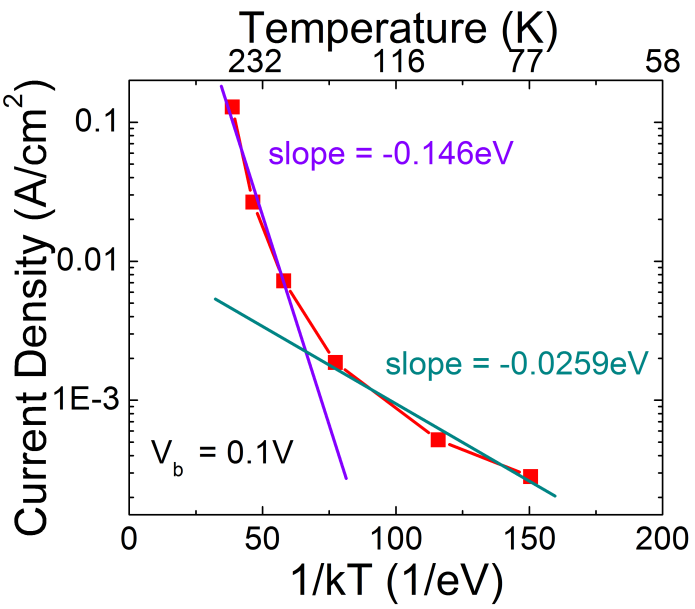

Figure 5.4: Arrhenius plot of the dark current density of the detector with n.i.d. absorber.

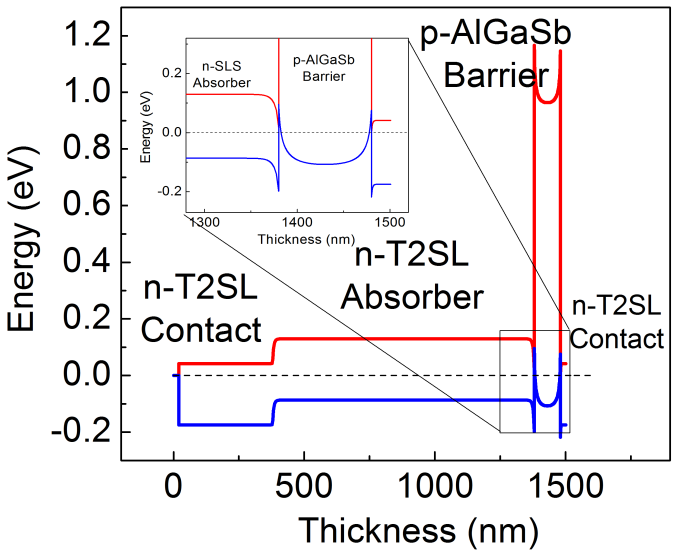

Figure 5.5: *nextnano*^{3} simulation of the bandstructure alignment in the MWIR T2SL nBn detector.

5.2.2 Photoresponse

The spectral response of the detectors was measured with a Nicolet 670 Fourier transform infrared spectrometer (FTIR) relative to a standard deuterated triglycine sulfate (DTGS) thermal detector. The 100%-cut-off wavelength of the n.i.d. detector is equal $\sim 6\mu m$ whereas the detector with the largest doping level ($n = 3.5 \times 10^{18} cm^{-3}$) shows a 100%-cut-off wavelength at $\sim 4.5\mu m$. The observed blue shift of cut-off wavelength is attributed to the Moss-Burstein effect [108]. the normalized spectral response of the four detectors measured at T = 77K with a bias of $V_b = 0.1V$ is presented in Figure 5.6.

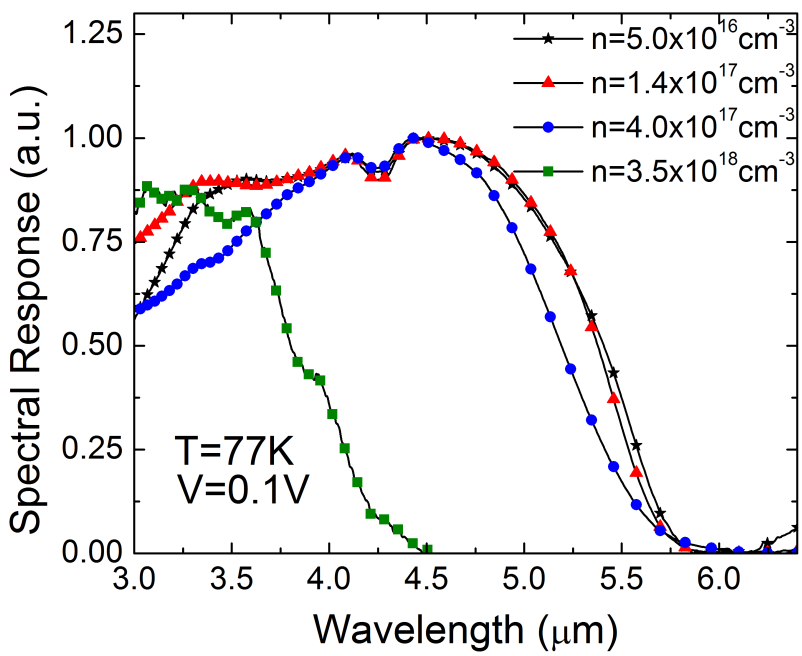

Figure 5.6: Spectral response of the four detectors.

The bandstructure mis-alignment of the absorber and barrier layer is also apparent in the bias dependent responsivity which is shown in figure 5.7. The responsivity

does not even saturate in the range measured up to $1.2V$ of applied bias indicating the presence of a barrier or a well in the valence band to impede the flow of carriers. Such a high bias is not acceptable because of the high dark current that would be experienced.

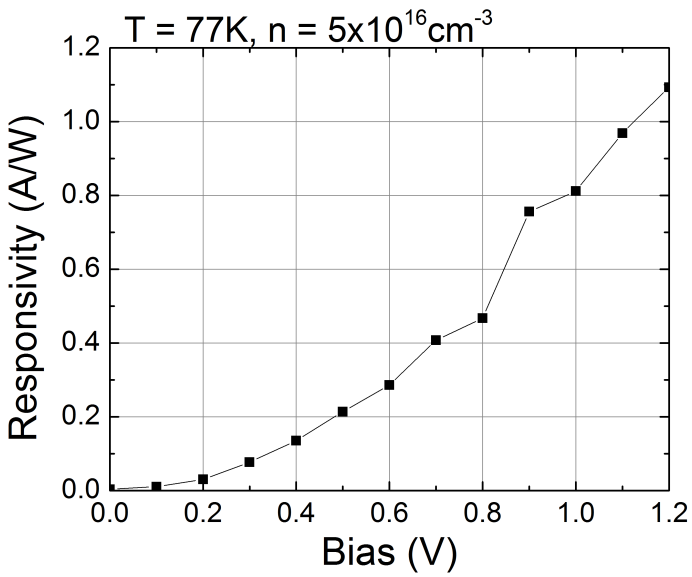

Figure 5.7: Bias dependent responsivity of the detector with the absorber doping of $n = 5 \times 10^{16} cm^{-3}$.

Johnson limited specific detectivity (D*) was estimated from dark current measurements and responsivity. The D* was calculated at $4.4\mu m$ for all the detectors studied. The low-temperature (77K) dependencies of specific detectivity along with the dark current density as a function of n-type doping level of the absorption region are presented in Figure 5.8 (Vb = 0.1 V). The significant degradation of both parameters with increased n-type doping level of the absorbing region is observed. The maximum detectivity that was measured was 2.3×10^{10} Jones for the n.i.d. device (0.1 V). The bias-dependent values of D* at 77K for the four devices are shown in Figure 5.9.

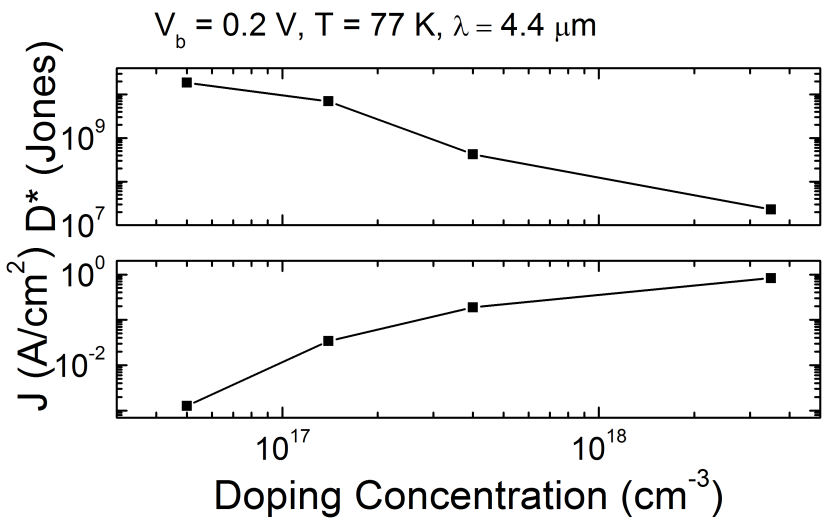

Figure 5.8: Absorber doping dependence of the four detectors.

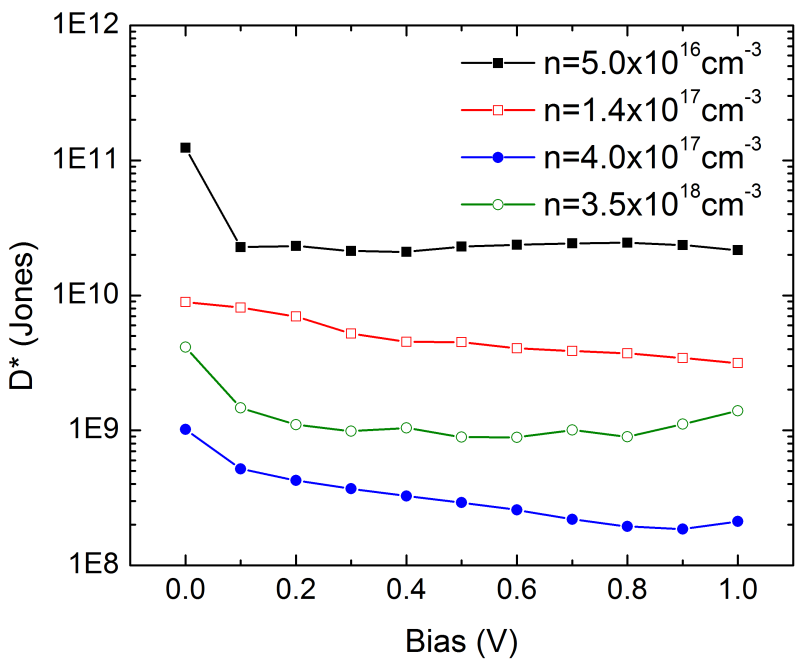

Figure 5.9: Specific detectivity bias depdence of the four detectors at 77K.

5.3 MWIR nBn With N-type Doped Barrier

To overcome the problem of the well in the valence band at the electron barrier layer the bandstructure of the electron barrier needs to be shifted down. Shifting the barrier bandstructure can either be done by adjusting the barrier layer composition or by changing its doping. Since changing the composition would also result in increased strain, which could result in defects, it was decided to adjust its doping. In order to shift the bandstructure, the barrier needs to be doped n-type which would raise the Fermi energy level of the barrier layer. Thus a similar design was fabricated and tested as the previous four designs, however, the barrier layer was doped lightly n-type ($\sim 7 \times 10^{15} cm^{-3}$). Dark current density as a function of temperature and bias was measured for this detector which is shown in figure 5.10.

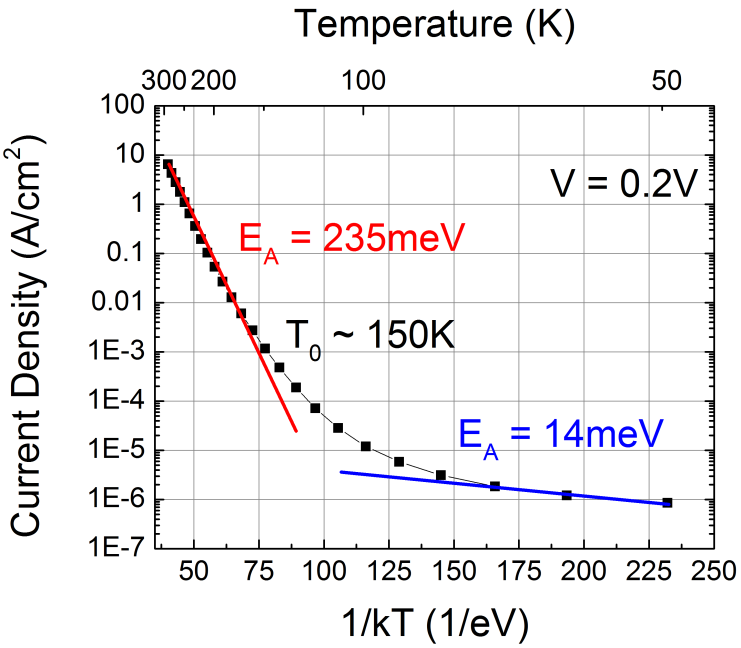

Figure 5.10: Arrhenius plot of dark current density for MWIR nBn detector with n-type doped barrier.

This detector clearly showed diffusion limited current for the high temperature

range. From approximately 150K to 290K the detector was diffusion limited with an activation energy of $\sim 235meV$ which agrees well with the expected band gap energy of 244meV. The activation energy then transitions to $\sim 14meV$ at 80K and lower. The dark current density is also approximately two orders of magnitude lower at $\sim 80K$. Thus the detector with the doped n-type barrier shows a clear improvement over the earlier design. For comparison, in figure 5.11 the Arrhenius plot for a MWIR p-i-n detector's dark current density is shown. Note that for the high temperature range ($> 100K$) the activation energy is $\sim 130meV$, on the order of half the bandgap indicating G-R limited. However, once again at low temperatures the activation energy is $\sim 12meV$, much less than the bandgap energy indicating surface leakage effects or tunneling.

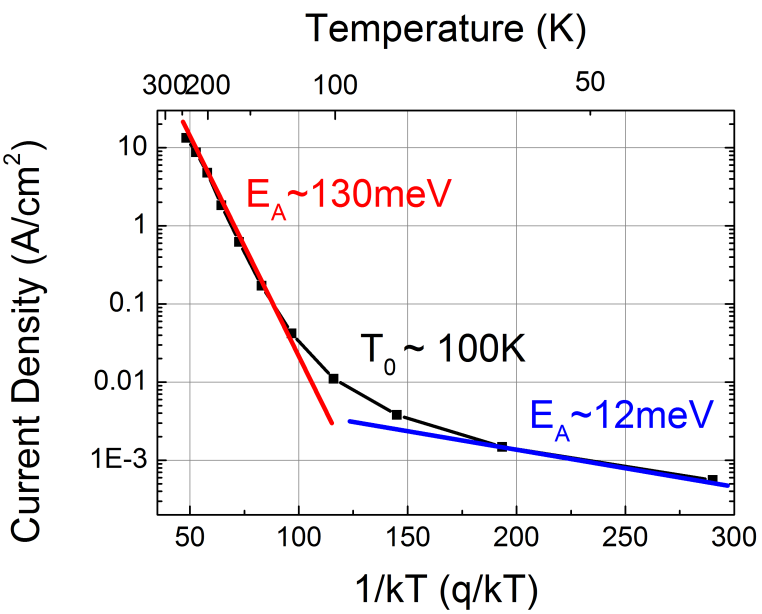

Figure 5.11: Arrhenius plot of dark current density for a MWIR PIN T2SL detector.

5.4 Summary

In conclusion, we have investigated the electrical and optical properties of a MWIR nBn detector as a function of background carrier concentration in the absorbing region of the device. Contrary to our expectations, dark current density was dramatically affected by the change of the n-type doping level in the detector absorption region. Such behavior can be attributed to the presence of a quantum well (QW) for the minority carriers (holes) formed in the valence band. The device with the n.i.d. doping level in the absorption region demonstrated the best performance among all studied samples. However, the dark current was still rather high and diffusion limited current was not achieved. To correct for the apparent well present in the valence band, the electron barrier layer was lightly n-type doped to shift the band structure down. The modified design had diffusion limited current down to 150K and achieved a dark current density of 3×10^{-6} at 80K.

Chapter 6

LWIR nBn, pBn, and pBp Detectors

6.1 Introduction and Motivation

Incorporation of unipolar barriers in long wave infrared (LWIR) detectors improve performance by lowering dark current density and, consequently, raises the detector operating temperature. Various heterostructure architectures have been utilized [91, 8, 67, 71] for performance enhancement of LWIR detectors. This section will describe and contrast the use of a nBn and pBn architecture for LWIR detectors based on type-II InAs/GaSb superlattices (T2SL) as well as discuss photoconductive gain in a pBp type configuration.

A pBn detector is desirable because it utilizes a wide band gap barrier at the p-n junction to help reduce dark current mechanisms without removing the built in potential of a diode. A nBn detector is expected to have even lower dark current due to the removed or reduced depletion region of a p-n junction and has the added benefit of only requiring one type of dopant which is advantageous for some materials

[77, 78]. Ref. [86] presents a similar study in which nBn and nBp detectors composed of MWIR InAsSb were compared for their photocurrent, temperature dependent dark current, dynamic resistance - area product, and carrier concentration. This study will focus on dark current and responsivity behavior for multiple temperatures and how the barrier and junction affect them.

6.2 Detector Designs and Fabrication Details

Three structures were produced for this study. One is a pBn and the other two are nBn designs. One of the nBn designs has a n.i.d. barrier and the other has a lightly doped p-type barrier. Both detectors are designed with a top contact with a larger band gap energy to help further reduce dark current associated with narrow band gap materials. The pBn design is desirable because of the large built in potential that is created which reduces the amount of applied bias required for operation, however, the nBn design has lower dark current due to less depletion extending into the narrow band gap material. Both designs work similarly with the detector junction being located at the interface of the barrier and absorber. The primary difference being that the nBn requires a significant applied bias. Descriptions of the device operation are readily available in ref. [6, 82].

The material schematic for the detector structures are shown in figure 6.1. Estimations of the band gap energies and electron affinities, as determined by the empirical pseudopotential method (EPM) [112, 71], were used to define the material layers.

Figure 6.1: Schematic of the LW pBn, nBn, and nB(p-)n structures.

All three structures consist of a n+ bottom contact superlattice layer composed of 135 periods of 14 mono-layers (ML) of InAs and 7 ML of GaSb. Strain compensation was also used in each layer period but the details of which are not discussed here. A layer with graded doping, from n+ to non-intentionally-doped (n.i.d.), 40 periods of the same superlattice was grown on the bottom contact layer followed by 300 periods of the same superlattice (n.i.d.) to serve as the absorber. This was followed by 45 periods of a superlattice composed of 7 ML of GaSb and 4 ML of AlSb; this layer serves as the electron barrier. The final capping layer composed of yet another superlattice consisting of 30 periods of 5 ML of InAs and 7 ML of GaSb serves as the top contact. The thicknesses are listed in figure 6.1. The differences between the three detectors are as follows: the pBn detector has a P+ top contact, the nBn detectors are the same but the top contact is N+ doped, and for one of the nBn detectors the barrier is lightly p-doped. Detailed growth descriptions can be found in ref. [111].

6.3 Results and Discussion

The detectors were electrically and optically characterized. For the spectral response and current-voltage measurements, the detectors were mounted in a helium cyro-pump cooled Janis-Research cryostat and regulated with a LakeShore 331 temperature controller. The spectral response was measured with a Nicolet 670 fourier transform infrared (FTIR) spectrometer using an external detector configuration. Current-voltage (I-V) measurements were conducted with a HP4145B semiconductor parameter analyzer. Responsivity was conducted in a liquid nitrogen cooled Janis cryostat and utilized a calibrated Mikron black body source tuned to 900K, an optical chopper, a long wave band pass filter, a Keithley 428 voltage amplifier, and a Stanford Research 770 network analyzer. It is noted that the bias configuration is such that reverse or negative bias extracts photo-response from both the pBn and nBn designs, so dark current and photo-response will only be discussed for that bias range.

The dark current density was measured for all three detectors for temperatures ranging from 50K to 200K in 10K steps. The dark I-V curves for each detector is shown in figure 6.2, an Arrhenius plot is shown in figure 6.3.

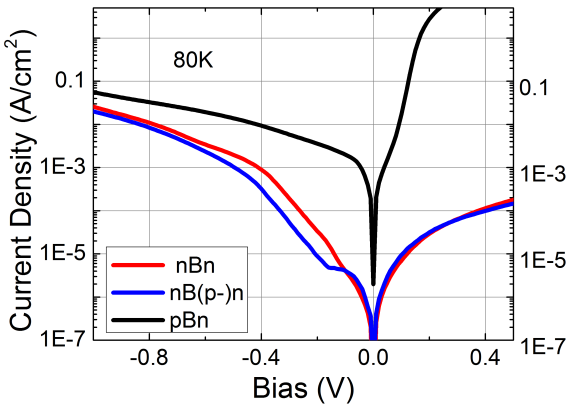

Figure 6.2: Bias dependent dark current density of the LW pBn, nBn, and nB(p-)n structures.

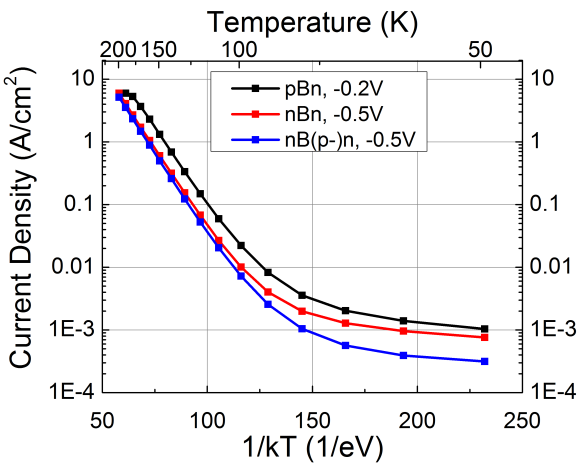

Figure 6.3: Temperature dependent dark current density of the LW pBn, nBn, and nB(p-)n structures plotted on an Arrhenius scale.

The primary differences observed between the pBn and nBn designs is that the pBn has an overall higher dark current density across the bias and temperature range shown and that it does not experience as strong as a bias dependence as the nBn detectors between 0V and -0.4V. Later, it is shown that the photo response for the nBn detectors have a turn-on voltage of $\sim -0.4V - 0.5V$ that corresponds with the

I-V data. Where as the pBn detector is shown to have an optical turn-on bias of ∼0.2V. The current density of the pBn detector at -0.2V is 3.58mA/cm^2 whereas for the nBn detector at a bias of -0.5V, is 1.98mA/cm^2. Even at the higher bias, the nBn design has a slightly lower dark current density than the pBn.

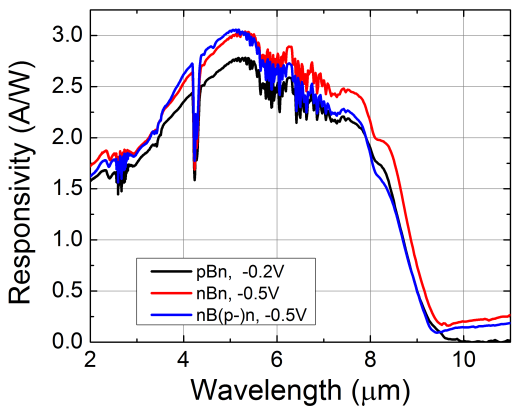

Figure 6.4: Spectral response of the LW pBn, nBn, and nB(p-)n structures at 77K.

The temperature dependent dark current plotted on an arrhenius scale shows all three detectors to be diffusion limited at high temperature. The low activation energy for the low temperature range for all three detectors suggest either surface leakage effects or tunneling. From 50K to about 70K the activation energy was ∼3.6meV – 8.6meV for all three detectors. From about 90K to 290K the activation energy is ∼102meV – 113meV which is slightly lower than the band gap expected from the measured cut-off wavelength of $\sim 9.5\mu m$ at 77K as shown in figure 6.4. For the whole temperature range in which the detectors are diffusion limited, the pBn detector is approximately a factor of two larger suggesting the nBn designs also diminish diffusion current. The transition temperature from diffusion limited to tunneling or surface limited behavior is roughly around 80K – 90K for all three detectors, however it is apparent that it is slightly lower for the nBn detector with the p-doped barrier which implies the p-type doped barrier potentially helps with

reducing tunneling current. This can be attributed to the importance of proper alignment of the barrier Fermi energy level to minimize the presence of depletion within the absorber [113]. To further investigate bandstructure alignment the bias and temperature dependent responsivity was measured which is shown in figure 6.5 and 6.6.

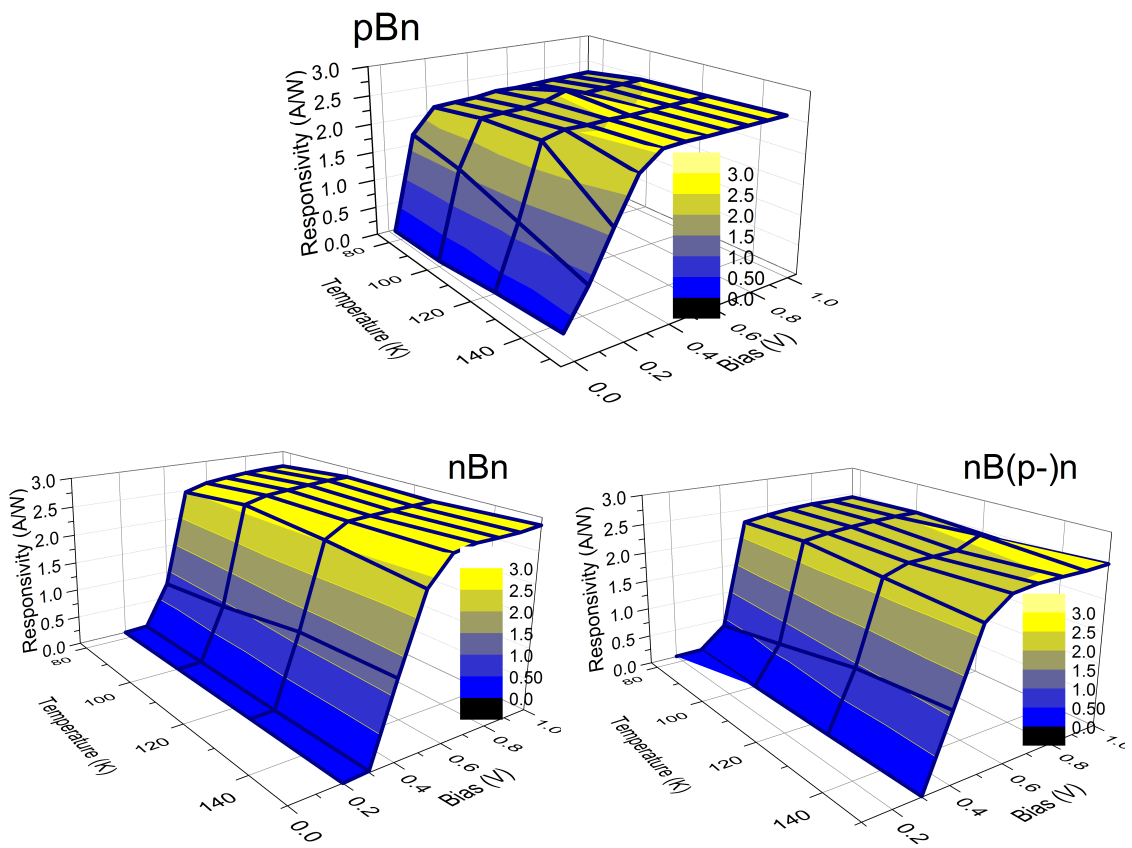

Figure 6.5: Bias and temperature dependent responsivity of the LW pBn, nBn, and nB(p-)n structures.

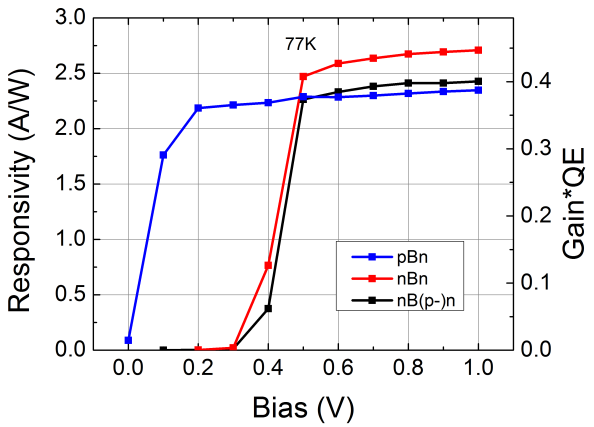

Figure 6.6: Bias dependent responsivity of the LW pBn, nBn, and nB(p-)n structures at 77K.

As mentioned earlier, the turn-on voltage for the pBn design is ∼0.2V and for the nBn designs is 0.5V. The turn-on voltage is defined here as the lowest bias at which the responsivity achieves roughly 90% of its maximum value or saturates. The responsivity at these biases are 2.18A/W for the pBn, 2.47A/W for the nBn with n.i.d. barrier and 2.26A/W for the second nBn detector. The three designs follow a very similar bias dependence from -0.4V to -1.0V. However, the nBn n.i.d. barrier design shows a slightly higher responsivity; on the order of 10% - 15% higher than the pBn. Several factors could play a part in causing this. For instance, it was recently shown that slight changes in the growth temperature can significantly affect the photo-response of a detector [61]. This can also be compounded by experimental error arising during device testing as well.

The turn-on voltage for all three devices can be explained by a barrier in the valence band of the structures. For instance the pBn design, which should have a 0V or very small turn-on voltage, must have a valence band offset between the absorber and barrier or barrier and top contact that hinders hole current. Thus, an external bias of at least 0.2V is required to supply enough energy to the holes to overcome

the barrier. This band offset is most likely between the absorber and barrier layer since the top contact is degenerately doped p-type. for the nBn detector, the top contact is degenerately doped n-type which forces the band structure to shift down in energy and creates an even larger valence band offset. To help explain this, TCAD simulations by the Synopsis Sentaurus simulation environment were conducted to estimate the energy band structure line up. The bandstructure for the individual layers were determined by EPM as mentioned earlier. The simulation results for 0V of applied bias for each design is shown in figure 6.7.

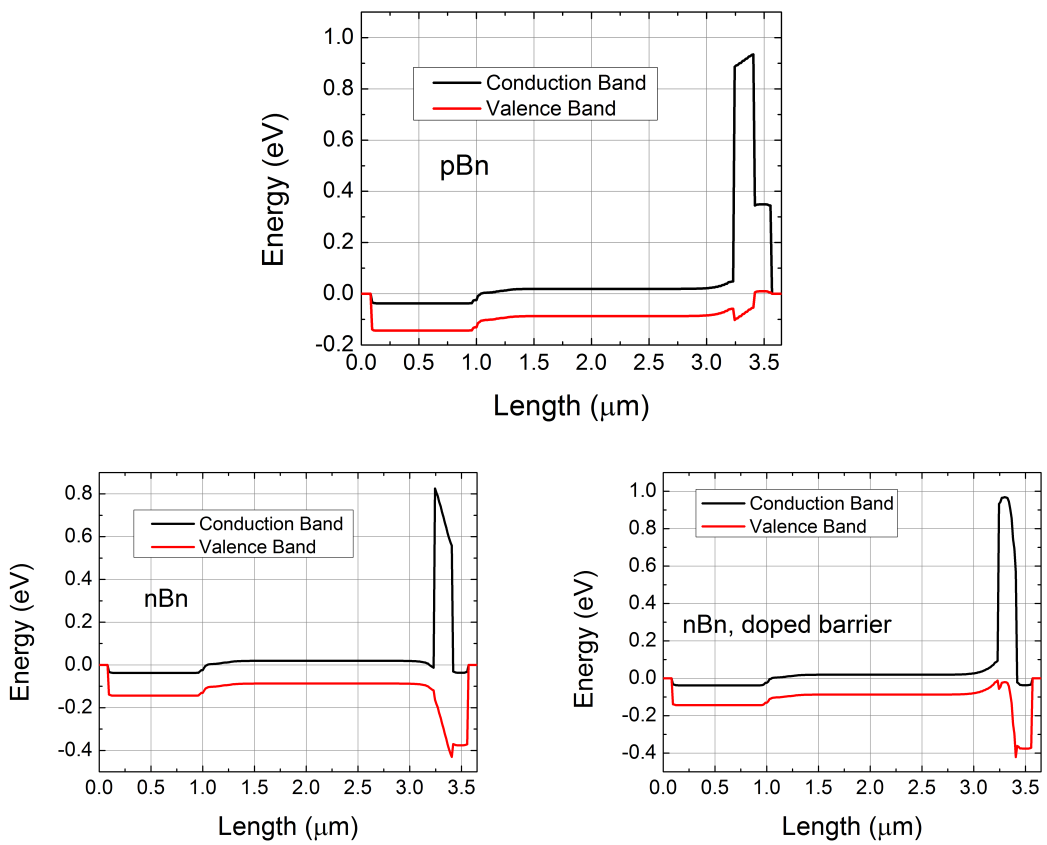

Figure 6.7: Simulated bandstructure of the LW pBn, nBn, and nB(p-)n structures.

The pBn design shows a valence band offset between the absorber and barrier

that creates a 41meV hole barrier. The hole barrier for the nBn design is 150meV. Understanding the turn-on voltage for the simulated band structures can provide clues about how much of a hole barrier exists in the real devices.

The saturated responsivity remains relatively constant across the temperature range measured, with just a slight 5% – 10% increase with increasing temperature. The turn-on voltage for the nBn detector remains relatively constant, for the measured temperature range, at $\sim$ -0.5V, but the turn-on voltage for the pBn design increases to $\sim$ -0.4V at 150K. One possible explanation of this is the difference in temperature dependence between the absorber layer and the barrier layer. For instance, the background carrier concentration has been shown to vary in in both MWIR and LWIR superlattice devices [114, 115, 116] which can cause the alignment of the junction between the absorber and electron barrier layer to shift. If the absorber was becoming more p-type with increasing temperature, the alignment of the fermi energy position would cause the valence band offset to increase and create a larger barrier between the absorber and electron barrier layer. In ref. [116] it is shown that the carrier type changes from n-type to p-type at 140K for LWIR T2SL which would match the result that we see. This effect is presumably not observed in the nBn detectors because of the already relatively large barrier that is present.

Table 6.1: Comparison of LW heterostructure detector designs

Structure	Dark Current Density (A/cm^2)	Gain*QE	D* ($cm\sqrt{Hz}/W$, Jones)	Bias (V)	50% Cut-off Wavelength (μm)
nBn	1.98×10^{-3}	0.41	2.87×10^{9}	0.5	8.6
nB(p-)n	1.05×10^{-3}	.37	2.36×10^{9}	0.5	8.36
pBn	3.58×10^{-3}	0.36	4.99×10^{9}	0.2	8.5
pBiBn [10]	1.57×10^{-5}	0.235	3.7×10^{10}	0.06	8.3
CBIRD [91]	9.9×10^{-6}	0.29	1.1×10^{11}, F/2	0.2	9.9
pπMn [117]	5×10^{-5}	0.44	8.1×10^{11}, JL	0.05	9.63
pMp [8]	3.3×10^{-3}	0.175	4.0×10^{10}, JL	0.05	14

The detector designs in this study exhibited dark current densities two orders of magnitude higher than other LWIR heterostructure T2SL detectors with comparable cut-off wavelengths. However, the QE was on par aside from the devices requiring significantly higher operating biases. An interesting note in the other designs listed in the table, however, is that all the structures are composed of a double barrier or heterostructure system. The pBn design in fact, is very similar to the pBiBn detector. The difference being the lack of a wide band gap hole barrier layer between the absorber and n-type contact. Even the pMp detector has a double barrier configuration which includes the M-structure superlattice valence band barrier adjacent to the top conatact and the GaSb bottom contact layer.

6.4 Photoconductive Gain in LW pBp

Single unipolar barrier detectors such as the nBn and pBp designs have been described as hybrid designs of diodes and photoconductors. However such characteristics as photoconductive gain has had limited investigation. This section investigates the presence of photoconductive gain in LWIR pBp detectors.

6.4.1 pBp detector

In the pBp architecture the minority carriers are electrons, as opposed to the nBn design [6], which is advantageous because of the higher mobility of electrons in comparison with holes (approximately two orders of magnitude higher) in the SLS system [88] which increases the photo response of a given device. pBp based devices have been previously investigated by Nguyen et al. [8, 89] in which a pBp or so called pMp

was created using the M structure for the barrier. For the work in this report the barrier is composed of an InAs/AlSb superlattice structure. The ideal band structure and operation of the pBp detector is illustrated in figure 6.8.

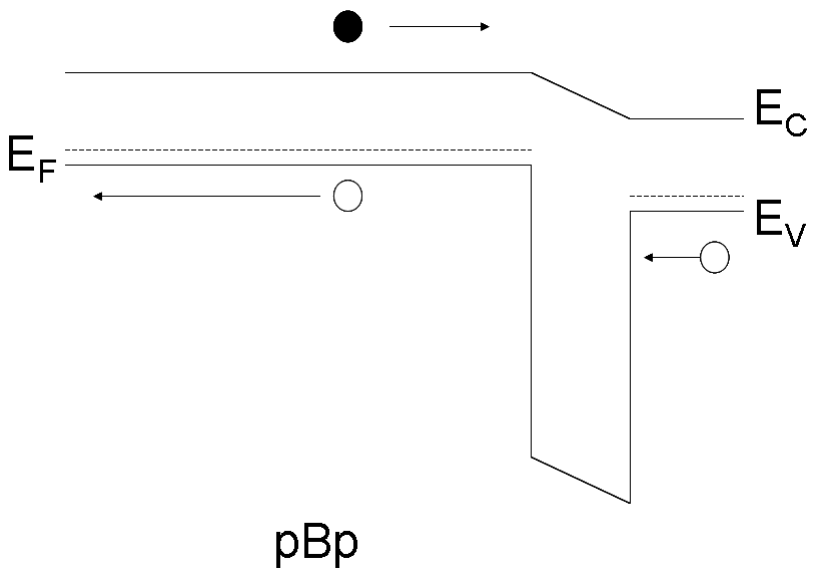

Figure 6.8: Qualitative illustration of pBp band structure showing direction of carrier flow.

6.4.2 Photoconductive Gain

Photoconductive gain is a characteristic of a detector that describes the amount of carriers extracted from a detector given a certain number of incident photons. For instance, a photodetector may absorb one photon but then contribute more or less than one electron to the photocurrent. In a typical photoconductor, when a photon is absorbed, an electron-hole pair is formed and these carriers are extracted by an applied bias at opposite terminals. However, this process may not occur so simply because the electrons and holes of a given material tend to have different mobilities and therefore have different transit times across the detector material. The electron usually has a higher mobility than the hole, and thus is extracted before the hole

is. In order to retain charge neutrality additional electrons can be injected by the contact, therefore more carriers are supplied to the photocurrent than produced by incident carriers. In turn, a gain is applied to the signal produced from incident photons. The situation described applies to detectors in general, however, it assumes that both contacts are non-blocking ohmic contacts. this isn't the case for a reverse biased P-N photodiode in which both contacts block the re-injection of photo-carriers, preventing a gain of more than unity [118, 119].

For the case of the pBp detector, we have a different situation in which one contact is an ohmic non-blocking contact and the other is effectively blocking carriers from being injected as depicted in figure 6.8. This prevents re-injection of holes at the anode but electrons can still be freely injected at the cathode. Enabling the possibility of a gain greater than unity. The general expression for photoconductive gain,$G = \tau/\tau_{tr}$, where τ is the carrier lifetime and τ_{tr} is the electron transit time. This expression implies that if the carrier lifetime is less than the electron transit time, gain will be less than unity and conversely if the carrier lifetime is greater than the electron transit time, the gain will be greater than unity. The complementary barrier infrared detector (CBIRD) has previously been studied for its PC gain properties and was found to have non-unity gain for certain design conditions [75]. A qualitative representation of the bias dependence of gain for devices with ohmic contacts, blocking contacts and one blocking contact based on the discussion from [120] is shown in figure 6.9.

The transit carrier transit time is determined by either drift (carrier transport by electric field) or by diffusion (carrier transport by a carrier concentration gradient). For the case of drift the transit time can be written as:

$$\tau_{tr,drift} = \frac{l}{v} = \frac{l}{\mu\frac{V_B}{l}} = \frac{l^2}{\mu V_B} \tag{6.1}$$

Where l is the length of the device, v is the carrier velocity, μ is the carrier mobility and V_B is the voltage bias across the device. The diffusion transit time the expression is:

$$\tau_{tr,diff} = -\frac{1}{D}\int_0^l \frac{n}{\frac{dn}{dx}}dx, \tag{6.2}$$

Where D is the diffusion coefficient, n is the carrier concentration, and x is the position within the device length from 0 to l. For the case of a linear carrier concentration profile $tau_{tr,diff} = \frac{l^2}{2D}$. The diffusion coefficient can be estimated using the Einstein relation: $D = \mu kT/q$. Given that the lifetime and mobility of superlattice materials have some uncertainty, the mobility-lifetime product can be isolated in the gain expression so that it may be used as a fitting parameter, which gives:

$$G_{diff} = (\tau\mu)\left(\frac{2kT}{l^2 q}\right), \tag{6.3}$$

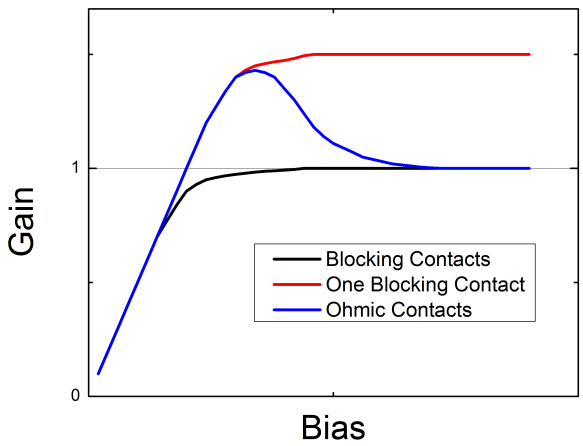

Figure 6.9: Qualitative illustration of bias dependent photoconductive gain for detectors with ohmic contacts, one ohmic and one non-ohmic/blocking contact, and both non-ohmic/blocking contacts.

Understanding photoconductive gain is important because it can affect a device's performance. For instance, a large gain can lead to filling of the read out integrated circuit's (ROIC) charge wells, which requires a shorter integration time for the ROIC, and a less than unity gain would require a longer integration time. Also, the speed of a device is inversely related with the photoconductive gain making devices with large gain to have low speed performance.

6.4.3 Fabrication and Design details

This section will cover details concerning the growth of the material and processing techniques used to fabricate the device.

Material Growth

The structures for this study were grown using a VG-80 solid source molecular beam epitaxy (MBE) system with a valved As cracker source on epi-ready (100) GaSb substrates. The two structures used in this study are shown in figure 6.10. More specifically, sample A, the p-i-n control sample, consists of 75 periods of 14 monolayers (MLs) InAs x 7 MLs GaSb n-type doped bottom contact superlattice layer, 50 periods of a graded n-type doped region of the same superlattice, 150 periods of a non-intentionally doped (N.I.D., n-type) LWIR absorber layer of the same superlattice, 25 periods of a graded p-type doped layer of the same superlattice, and finally a p-type doped GaSb top contact layer all grown on a n-type Te doped GaSb substrate. Sample B, a LWIR pBp detector, consists of 110 periods of the previously mentioned superlattice p-type doped bottom contact layer, 150 periods lightly p-type doped absorber layer of the same superlattice, 33 periods of a 16/4 ML InAs/AlSb lightly p-type doped, and 15 periods p-type doped top contact layer of the original superlattice all grown on a n-type Te doped GaSb substrate.

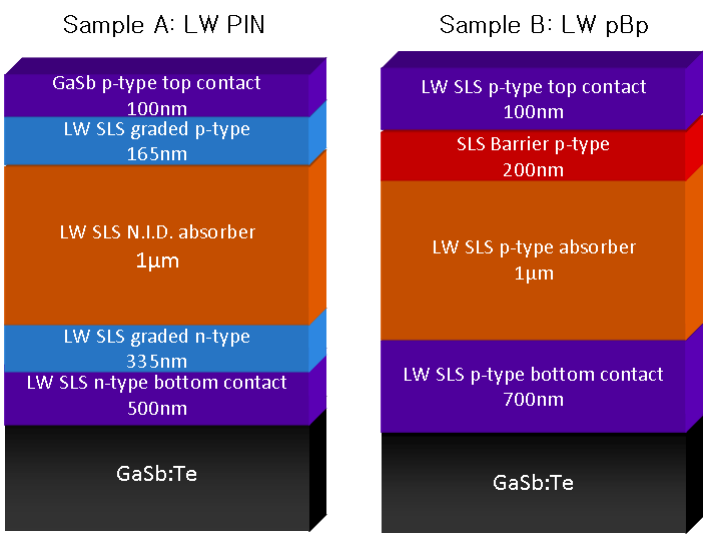

Figure 6.10: Schematic of the PIN and pBp structure.

These devices were designed to absorb long-wave infrared (LWIR) radiation and each have a $1\mu m$ thick absorber layer. The individual layer thicknesses were chosen using the empirical pseudopotential method (EPM) to determine the proper band alignments of the different regions[112, 71]. Doping for the barrier layer of the pBp device was decided using a systematic study consisting of devices with no doping, n-type doping and p-type doping.

Fabrication Details

Single pixel devices with square mesas of 410 x $410\mu m^2$ and apertures with diameters of $200\mu m$ were fabricated from the structures. The processing utilized standard optical photolithography for the various pattern definitions, an inductively coupled plasma (ICP) dry etch with BCl3 for etching to the bottom contact, and electron-beam metal evaporation of Ti/Pt/Au (500/500/3000 $\AA$) was used to make contact pads. Test pieces were then cleaved and mounted in 68 pin LCC chip carriers using silver conductive epoxy. Measurement pads on the test pieces were then wire bonded to the test pins on the chip carrier for testing in a cryostat.

Unprocessed material was also used for transmission measurements. In order to remove absorption affects from the substrate, transmission measurements are normalized to the transmission of the substrate with the epi-layer removed. Two pieces approximately $1cm^2$ in size were used for this measurement, one piece remained untouched, the other had the epi-layer etched away using the same ICP etching technique used in the detector fabrication.

6.4.4 Results and Discussion

Various characteristics of the two devices were then measured and compared. The measurements conducted include: X-Ray Diffraction (XRD) which is measured to

determine material quality before fabrication, absorption which indicates the absorption quantum efficiency to measure photoconductive gain, spectral response to determine spectral characteristics for calculating responsivity, and signal measurements for calculating responsivity as well. Details of these measurements and their results are described below.

X-Ray Diffraction

X-ray diffraction (XRD) spectra for both devices were collected to determine crystalline quality of the material. The XRD spectra was collected with a Philips double-crystal X-ray diffractometer using the $Cu - K\alpha 1$ line. Information that is gathered from XRD spectra include the period thickness of the grown superlattice and lattice mismatch which incidentally indicates whether the material is in tensile or compressive strain. Figure 6.11 shows the XRD spectra of the two samples in this study.

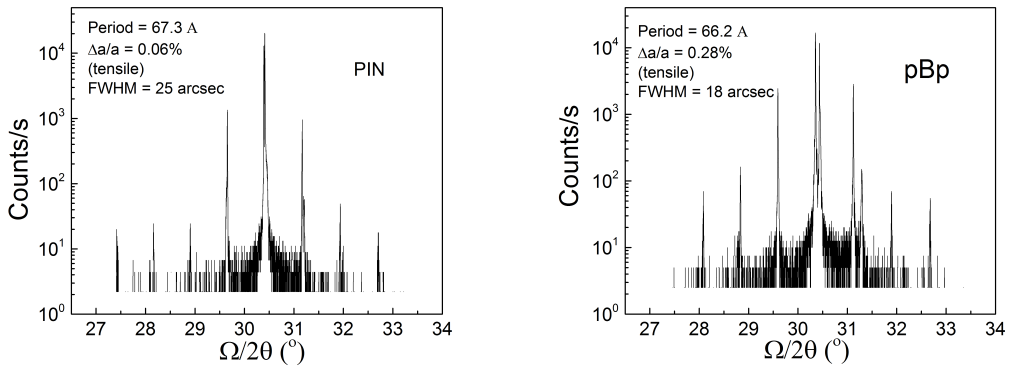

Figure 6.11: X-Ray diffraction spectrum of the PIN and pBp material.

The XRD data reveals the materials to be of suitable quality. Satellite peaks are observed indicating periodicity of the alternating material layers from which the period thickness was calculated to be 67.3$\AA$ and 66.2$\AA$ for the p-i-n and pBp structures, respectively. The lattice mismatch is 0.06% and 0.28% for the p-i-n and

pBp, respectively, indicating both structures to have slight tensile strain. The full-width-at-half-max (FWHM) was also determined to be 25 arc seconds and 18 arc seconds for the p-i-n and pBp, respectively, which is falls within the average interface roughness observed in our detector material growths.

Absorption

The absorption is determined by measuring the transmission of the sample mounted at the brewster angle with respect to the incident IR beam. This is done using a Nicolet 6700 Fourier Transform Infrared Spectrometer (FTIR) with a glowbar infrared source, a KBr beam splitter, a deuterated triglycine sulfate (DTGS) thermal detector, and a Janis research liquid nitrogen (LN_2) cooled pour filled cryostat. The sample with the epi-layer intact and the sample with the epi-layer etched away, as described earlier, are mounted using thermally conductive grease in the LN_2 cooled cryostat on a copper sample holder attached to the cold finger. The sample holder has holes over which the samples are placed for light transmission to be measured. The percent absorption is calculated from the transmission measurement data as follows: $A = 100 \times \left(1 - \frac{T_{sample}}{T_{substrate}}\right)$. Where "A" is the absorption, T_{sample} and $T_{substrate}$ are the transmission of the sample and substrate, respectively. The absorption data is shown in figure 6.12.

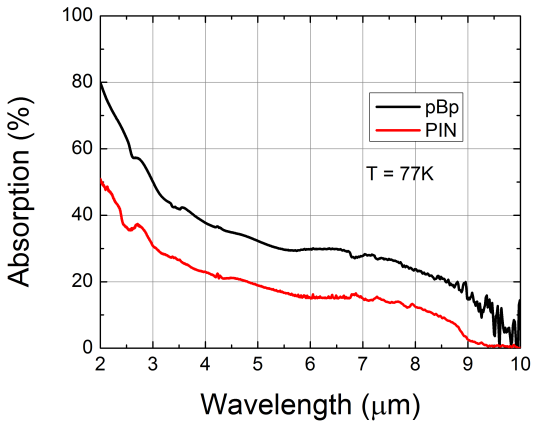

Figure 6.12: Absorption spectrum for the PIN and pBp detectors.

From the absorption spectrum, we see strong absorption in the near-IR region around $2\mu m$, the absorption decays and levels off around $6\mu m$ and then starts decaying again and appears to have a cutoff around $9.5\mu m$ for the p-i-n detector and around $10\mu m$ for the pBp. However, it is noted that the spectral range around the cutoff is rather noisy, due to significant LW absorption processes in the substrate, which makes the actual cutoff wavelength uncertain.

For the calculations in this study, including responsivity and photoconductive gain, the wavelength of $8\mu m$ is chosen because it is conventionally used as the beginning of the LWIR spectral range and because the absorption measurement is not noisy at that value giving us more certainty in the calculation. The absorption quantum efficiency (QE) is 12% and 23% for the p-i-n and pBp structure, respectively. The differences in the the QE value are attributed variations in the growth conditions. Also, the absorber for the pBp design is slightly p-type usually bears better absorption qualities than the n.i.d n-type absorber of the p-i-n.

Spectral Response

The spectral response was measured using a Nicolet 6700 Fourier Transform Infrared Spectrometer (FTIR) with a glowbar infrared source, a KBr beam splitter, a deuterated triglycine sulfate (DTGS) thermal detector, and a Janis research LN_2 cooled pour filled dewar. Results of the devices measured at 77K are presented in normalized arbitrary units and shown in figure 6.13.

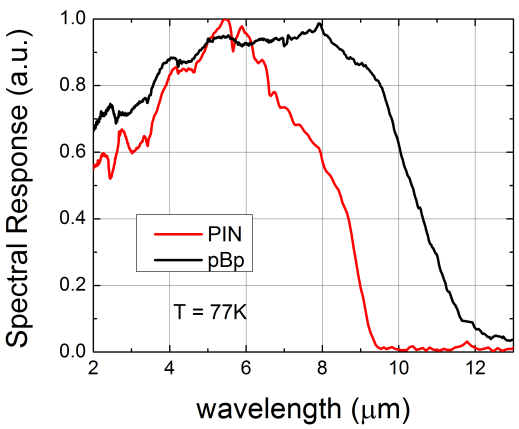

Figure 6.13: Normalized spectral response for the LW PIN and pBp detectors.

Both detectors show long wave response having 0% cutoff wavelengths of approximately 9.5 and 12μm for the p-i-n and pBp detectors, respectively. The differences in spectral features and cutoff wavelength are attributed to variations and uncertainty in growth conditions including source flux ratios and growth rates. Specifically, variations in the InSb strain compensation layer thickness can significantly affect the cut-off wavelength in T2SL materials [62].

Responsivity and Photconductive Gain

Responsivity was measured for the two detectors at 77K as a function of bias. The gain-efficiency product was calculated from the formula: $G\eta = R(hc/\lambda)$ and the gain was isolated by factoring out the estimated QE from the absorption measurement. The responsivity as a function of bias is shown in figure 6.14.

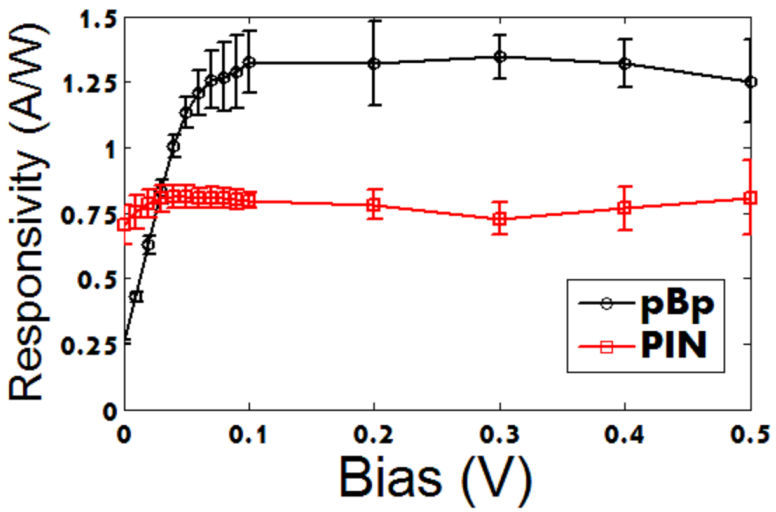

Figure 6.14: Bias dependent responsivity of the PIN and pBp detector

The pBp detector has a saturated responsivity of approximately $1.25A/W$ for the pBp detector and the p-i-n detector is lower with a value of approximately $0.75A/W$. The primary difference is the bias dependence in which the p-i-n has a weak dependence for the bias range measured and the pBp has a strong dependence for the low bias range but then saturates at $\sim 0.09V$.

The gain was then calculated using the gain-QE and dividing out the QE using the absorption-QE determined shown early. This assumes that the QE is not bias dependent. The gain for the two devices are shown in figure 6.15. for the p-i-n detector, the gain was determined to be $\sim 1 - 1.2$, which fits the expected value of unity with some experimental error. The pBp detector varies from ~ 0.2 to ~ 0.88

from a bias of $0V$ to $0.09V$ and saturates at ~ 0.88 for the rest of the bias range measured. The data collected in this study is shown below in Table 6.2.

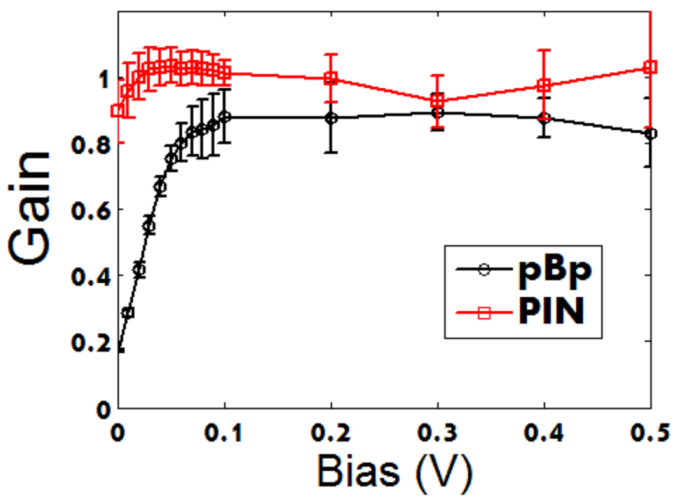

Figure 6.15: Bias dependent photoconductive gain for the LWIR T2SL PIN and pBp detectors at 77K.

Table 6.2: LW PIN and pBp detector summary

Detector	Abs. QE @ $8\mu m$	Cut-Off Wavelength (μm)	Responsivity @ 100mV (A/W)	Gain @ 100mV
PIN	0.12	9.5	0.75	1
pBp	0.23	12	1.25	0.88

The p-i-n detector exhibited a PC gain of ~ 1 as expected for a photodiode. For the pBp detector, the bias dependence was expected to be similar to the behavior exhibited in figure 6.9 for the detector with one blocking contact and one ohmic contact which produced a gain greater than unity. But this was not the case as observed in figure 6.15 which shows a gain less than unity indicating the pBp photoresponse

is similar to that of a photodiode. The slightly lower gain can be explained by decreased collection efficiency that results from hindered photocurrent as indicated by the necessity for a slight applied bias.

Using the mathematical definition of PC gain described earlier in the discussion we can analyze what the value of gain for the pBp detector suggests about its operation. Drift is presumably not the primary mechanism for which the carriers are collected since most of the applied bias is designed to fall across the barrier and not the absorber. Plus, uncertainty in the electric field across the absorber makes it difficult to estimate the drift transit time. Based on the gain of 0.88, the estimated mobility-lifetime product is $6.6 \times 10^{-7} cm^2/V$. The expected mobility-lifetime product based on literature [88, 96] is on the order of $10^{-5} cm^2/V$. Thus, the mobility or carrier lifetime for this particular detector must be lower than previously reported T2SL materials.

In Conclusion, a LWIR p-i-n and pBp detector based on the InAs/GaSb superlattice material system were fabricated and tested. The material quality was tested using XRD, absorption QE was determined using FTIR transmission measurements, spectral response was measured, and responsivity was determined using a calibrated blackbody. The gain for the pBp detector was shown to be lower than unity suggesting that the pBp detector will not contribute to over filling of the charge wells of ROICs and are suitable for high temperature operation and low NETD of focal plane arrays.

Chapter 7

Summary, Conclusions and Future Work

This dissertation has discussed single-unipolar infrared detectors designed for MWIR and LWIR. Background was provided describing the history of infrared detection and imaging along with status and trends of infrared detector technology as well areas of focus for research. The techniques for designing, material growth, fabrication and testing were also discussed in detail. Different kinds of semiconductor heterostructure designs were outlined and compared to those being studied here as well.

7.1 MWIR and LWIR Heterostructure Detectors

The work presented here described studies regarding variations of single unipolar barrier designs including nBn, pBp, and pBn in antimonide based material systems. The effect of varying barrier parameters were investigated for MWIR InAsSb/AlAsSb based detectors, absorber doping conditions and barrier doping were studied for MWIR T2SL based detectors, a comparison of LWIR T2SL nBn and pBn behavior

was presented, and photoconductive gain was studied for a LWIR T2SL pBp detector.

In the InAsSb nBn study, the AlAsSb barrier composition and doping were investigated. A total of four designs were made that included two different barrier compositions and two different doping conditions. All four designs required an applied bias to achieve the maximum photoresponse. The design with the lowest dark current and required the smallest applied bias had a barrier closely lattice match to the GaSb substrate and had a n.i.d. barrier. Though the designs with the n-type doped barrier had very similar dark current performance with better responsivity, giving one of the barrier doped samples the best D*.

The MWIR nBn study looked at the effect of the doping level in the absorption layer. The best performance was achieved with a n.i.d. doped absorber. The dark current density was significantly increased with increasing the n-type doping concentration in the absorber. This was attributed to mis-alignment of the absorber and barrier valence band, forming a well to trap photocarriers and encouraging tunneling and G-R current. To remedy this, the barrier was lightly doped n-type to shift the barrier band structure down. This allowed diffusion limited current to be achieved down to 150K.

The LWIR study investigated the difference in operation between pBn and nBn architectures as well as studied the photoconductive gain in a pBp architecture. The nBn design was found to have a lower dark current and the pBn design but required a large applied bias ($\sim 0.4V$) due to a large valence band offset in the top contact. The pBn, which should operate much like a p-i-n diode still required an external bias as well ($\sim 0.2V$) which was attributed to a valence band offset at the barrier. The pBn also exhibited an interesting temperature dependence, requiring a higher bias ($\sim 0.4V$) at 150K, which was explained by a change in the carrier type of the absorber at 140K. Where as the nBn designs kept a stable temperature dependence. The pBp design was found to have a gain of ~ 0.88. This lower than unity gain

suggests less than ideal photo-carrier extraction efficiency.

7.2 Future Work

As regards the work presented in this dissertation, future work includes investigating the variation in photoresponse of the MWIR InAsSb nBn detectors, Further optimization of the MWIR T2SL nBn detector, adjusting the contact layer parameters of the LWIR nBn and pBn designs, and optimization of the LWIR pBp design. For instance, the InAsSb nBn detectors exhibited different photoresponse behavior between the devices doped with silicon and the devices doped with tellurium. It needs to be understood if the photoresponse of the InAsSb absorber material was altered by the different doping impurities or if other growth conditions caused the variation. For the MWIR T2SL nBn detector, additional doping conditions need to be tested for the barrier to further improve dark current operation. The dark current behavior of the LWIR nBn and pBn detectors are still quite far from other T2SL designs. It is noted that the other designs incorporate a double barrier configuration which appears to be necessary for narrow bandgap LWIR detectors. A future design would include a bottom n-type contact with a wider bandgap which would create a situation similar to the pBiBn detector. Also, optimization of the barrier doping is required to decrease the required externally applied bias. For the pBp design a comparison of the InAs/AlSb barrier with that of the M structure would be beneficial to determine the optimal barrier material. Also the cause for the low activation that was observed in all the T2SL detectors needs to be investigated.

In general T2SL detectors have yet to break through the Rule 07 barrier. With heterostructure engineered devices, however, they have come close. But still, if T2SL detectors were operating as they are predicted, they would easily surpass the performance of HgCdTe detectors. The significant problems that remain, as described

by many scientists in the field, is the limitation of G-R and surface leakage current. To overcome these problems, various barrier detector designs have been created, and novel passivation schemes have been developed but have not achieved the desired performance. Various uncertainties still remain concerning T2SL detector material growth and fabrication. For instance, behavior of different dopant materials, defects and trap energies that lead to SRH G-R, and surface states that develop during processing. Additionally, newer material systems that are showing promise, such as the gallium free InAs/InAsSb superlattice which has been shown to have long carrier lifetimes need to be developed for detector operation.

Appendix

A Detailed Detector Fabrication Instructions

Appendix A

Detector Fabrication

This appendix gives a detailed description of the basic procedures for fabricating detectors in the KIND group.

A.1 Sample prep/cleaning

Samples prior to processing generally are very clean, however, they can accumulate dust from handling X-ray diffraction (XRD) measurements, Photoluminescence, and/or Nomarski microscopy. A general method of clean is as follows

- Rinse in acetone ∼30s - 5min (soaking or spraying)
- Rinse in methanol ∼30s - 5min (soaking or spraying)
- Rinse in isopropanol (IPA) ∼30s - 5min (soaking or spraying)
- Inspect under microscope
- If necessary, use acetone gun

- Re-inspect
- If necessary, use oxygen plasma descum
- Re-inspect
- Other more extreme methods exist but will not be discussed here

Oxygen Plasma Descum Notes

- O_2 plasma descum technique requires the use of the table top reactive ion etcher (RIE) in the base and acid bench bay
- An O_2 plasma asher is also available for such purposes
- The table top RIE is equipped with O_2 and CF_4
- During this step, only O_2 will be used
- Settings for the RIE are:
  - Power = 100W
  - O2 pressure = 100mTorr
  - Time $\sim$ 5 - 10 min
- However, parameter adjustments may be made as needed

Oxygen plasma descum RIE operation procedure

- The table top RIE unit is always on
- Turn off the vacuum by placing the soln switch in the off position
- Turn on the vent by placing the vent switch in the on position

- Open the lid, you may use the window port as a handle, note: the lid is rather heavy
- Place the sample anywhere on the surface, no need to tape down
- Close lid, and turn off vent switch
- Purge cycle: Turn of vacuum, open vent, wait 5sec, close vent, open vacuum and wait for pressure to stabilize
- Turn on Vacuum (soln switch) and wait for the pressure to drop (1min)
- When the pressure has stable (∼-0.01mTorr, the value is negative due to calibration issues) open the O_2 value by flipping the O2 switch, and wait for the pressure to stabilize
- Use O_2 knob to adjust the O_2 flow until the desired pressure is achieved
- Turn on the Plasma by flipping the plasma power switch, quickly adjust the power to the appropriate setting if it is not already
- Use timer to monitor time
- Turn off plasma power when desired time is reached
- Turn off O_2 and wait for pressure to stabilize
- Purge cycle: Turn of vacuum, open vent, wait 5sec, close vent, open vacuum and wait for pressure to stabilize
- Repeat 2 more times
- Close vacuum, open vent, and open lid when completely vented (∼1min)

A.2 Photolithography

Coating sample with photo resist

- Spin coat the sample with HMDS if necessary (experience has shown his not to be necessary for GaSb based samples unless sample is coated with SiN or SiO_2) and bake at 150C for 30sec
- Completely cover sample with Desired photoresist and spin coat at 4000 rpm for 30sec, increase or decrease spin as necessary to tune thickness
- Remove edge bead by carefully cleaning edge of sample with moderately acetone soaked alpha swap (or Q-tip)
- Bake at 90C for 90sec
- Allow sample to cool (∼30sec - 1min)

Mask alignment

- Have mask ready, may need to clean mask ahead of time by rinsing with Acetone/Methonal/IPA
  - For more rigorous cleaning, ask someone about using PIRANHA
- Place mask on the mask holder in the aligner and turn on vacuum to hold mask in place
- Put mask holder in the slot above the sample chuck
- Slide out the sample chuck and carefully place the sample on it (If not processing a whole wafer, I like to put a corner of the sample in the middle of the chuck to use a reference to help with theta alignment)

- Push the sample chuck back in place and carefully raise the chuck into contact position, readjust the z position if necessary (I watch for fringes to appear on the sample just as contact is achieved, this indicates that the sample is making contact)

- Put the aligner into separation mode and position the corner thats located in the middle of the chuck such that it is roughly aligned

- Move the microscope to one of the samples extremes and move only the theta knob to get as closely aligned as possible, then move the scope back to the middle and adjust only the x and y knobs

- Repeat until sample is satisfactorily aligned

- Set the exposure time to the desired setting, put aligner in contact mode, make sure sample did not shift while doing this and expose

Positive resist versus image reversal resist

- If using positive tone photoresist go straight to development

- If using image reversal resist, do the following

  - Let sample sit a few minutes to allow nitrogen to escape (this formed from a chemical reaction during exposure)
  - Bake sample at 112C for 1 min
  - Let sample for cool
  - Flood expose sample for 30sec
  - Now sample is ready for development

Development

- If using positive tone photoresist, make a 1:4 dilution (Water:Developer) of the AZ 400K developer, sometimes there is a bottle of the premixed dilution
- Develop for approximately 50sec - 70sec
- The time varies depending on exposure time, age of developer etc. A calibration development may be desired
- Rinse in the water baths on the bench for ∼30sec - 1 min in each bath and then dry with nitrogen gun
- If using an image reversal resist, make a 1:5 dilution of the developer
- Develop for ∼17 - 35sec
- Rinse in water and dry
- Finally, inspect under microscope, if pattern is as desired, proceed to next step, if not, clean off with solvents and repeat complete photolithography procedure
- If pattern is as desired, photolithography is complete

A.3 Etching

Etching can either be done using dry etching or wet etching. Below are listed some details of the different techniques concerning what gases and chemicals are available at CHTM.

Dry etching

- ICP (inductively Coupled Plasma)

  - Available gases
    * BCl3 (boron trichloride)
    * Cl2 (chlorine)
    * Ar (Argon)
    * N (nitrogen)

- RIE (Reactive Ion Etching)
  - Available gases
    * O (Oxygen)
    * Ar (Argon)
    * CF4 (Tetrafluoromethane)
    * CHF3 (Trifluoromethane)

Wet etching

Wet etching was not used or studied extensively so the list here is rather slim.

- H_3PO_4 based solution (Phosphoric acid)
- HCl based solution (Hydrochloric acid)
- Many others that will not be discussed here

Details of ICP dry etching

- ICP dry etching utilizes the PE01 system in the first bay
- The recipe used for etching InAs/GaSb based superlattices and other antimonide based materials is the InP etching recipe labeled Zia_InP

- The recipe has not been optimized any further, but has worked ok thus far
- ICP recipe details
  - BCl3 flow: 35 sccm
  - Chamber pressure: 2.5 mTorr
  - Temperature: 25 C
  - ICP power: 500 W
  - RIE power: 90 W

ICP dry etching procedure

- Log in to TIP and ICP
- Turn off ion gauge
- Vent the load lock (takes ∼3min)
- While load lock is venting, mount patterned sample on sapphire carrier wafer using mung
  - Various techniques exist for this, I suggest having an experienced user show you
  - Other research groups at other institutions use other substances for mounting samples for dry etching, we havent investigated any
- When load lock is vented, open load lock door and wipe seam with IPA soaked tech wipe
- Load carrier wafer with mounted sample onto ICP arm
- Close load lock, and begin load lock vacuum

- The procedure from here depends if you are using the automatic mode of the manual mode

RIE dry etching details

- RIE etching can be done with either PE02 (third bay with acid and base benches) or PE05 (second bay with the metal evaporators)
- RIE is generally used to do oxygen plasma descum (PE02) or Si_3N_4/SiO_2 etching (PE05)
- The recipe for Si_3N_4 and SiO_2 etching utilizes CF_4
- RIE SiO_2/Si_3N_4 etching recipe details
  - Ar flow: 3%
  - O2 flow: 3%
  - CF4 flow: 72%
  - Power: 150W

Acid and base wet chemical etching

- Advantages over dry etching
  - Possibly shorter process time
  - Superior dark current performance
  - Expensive high vacuum equipment not needed
- Disadvantages over dry etching
  - More care must usually be taken for safety because of the acids and bases involved

  - More careful calibrations must be performed
  - Wet etching tends to produce a lot of undercutting making small devices difficult to create

HCl etching recipe

- Chemical composition: $1:1:2$, $HCl:H_2O_2:H_2O$
- Remember to start with water and add other ingredients to it
- Measure amount of desired water
- Add peroxide to water
- Add acid to peroxide and water mixture
- Etch rates tend to vary due to the age of the constituent materials, temperature, etc., so calibration of etch rates is necessary

H_3PO_4 **etching recipe**

- Chemical composition: $1:2:20$, $H_3PO_4:H_2O_2:H_2O$
- Same instructions for mixing as described for the HCl solution
- Again, etch rates vary so calibration etches are needed
- Typical etch rate $\sim 0.08 \mu m/\text{min}$

A.4 Passivation/Encapsulation

- Passivation: A protective layer that chemically reacts with the device surface to prevent surface leakage current

- Encapsulation: A protective coating that does not necessarily chemically modify or react with the surface
- Passivation or encapsulation is used to protect the surface of the device (primarily the sidewall surface) in order to prevent degradation and surface leakage current
- The most common forms of passivation/encapsulation methods we use include SiN, SiO2, and SU-8
- Other methods of passivation include treatment with various forms of sulfur, but those will not be discussed here

Passivation pretreatment

- Prior to passivating devices, a pretreatment of the detector side walls is recommended
- This is typically done with an acid dip
- Here are 2 common recipes that are used
  - HCl:H2O (1:10) dip for 30 sec
  - $H_3PO_4 : H_2O_2 : H_20$ (1:2:20) dip for 15 sec
- The HCl solution is low risk in that it does not etch or etches the detector material very slowly. It only etches oxides
- The Phosphoric acid solution does a good job of cleaning since it actually etches material; it can remove the outmost layer of the device that was potentially damaged during the dry etch step. However, since it etches, it poses a risk at etching the device too much

Si_3N_4 and SiO_2 deposition

- SiN or SiO2 can be coated using either chemical vapor deposition (CVD), plasma enhanced chemical vapor deposition (PECVD), and electron beam evaporated deposition
- Regular CVD is too hot to be used with our devices (∼800C !) so PECVD and e-beam deposition are the methods of choice for us
- Of these two, PECVD has been used more, this is somewhat arbitrary but it has been the primarily method for various reasons including quality of material and availability of equipment
- PECVD can be done either at the CHTM cleanroom or at the CINT (Center for Integrated NanoTechnologies) cleanroom
- The procedure described here is for the CHTM cleanroom

PECVD Procedure

- Close the vacuum valve
- Turn on the nitrogen purge and wait for the chamber to be vented
- Open the chamber and wipe the sample stage and chamber seam with an IPA soaked tech wipe
- Place a silicon carrier wafer on the stage and place the sample on the carrier wafer as close to the middle of the stage as possible
- Close the chamber lid, close the nitrogen purge and slowly open the vacuum valve

- When the vacuum has stabilized (∼0.080Torr) open the nitrogen purge valve for 30sec and then close it and wait for the vacuum to stabilize
- Repeat this 2 more times
- Turn the RF control panel and the power for the heater
- Set the heater to 190C and wait, this will take 2 hours to warm up and stabilize
- When temperature is settled, open the gas valves and set their flow rates one at a time in the order of nitrogen, ammonia, and finally silane
- The flow rates for the gases for SiN deposition are
  - N_2 20 sccm
  - NH_3 100 sccm
  - SiH_4 20 sccm
- The pressure should be 850–890 mTorr
- The N_2 flow can be adjusted to help maintain this
- The flow rates for the gases for SiO_2 deposition are
  - N_2 40 sccm
  - N_2O 160 sccm
  - SiH_4 20 sccm
- The pressure should be 760–800 mTorr
- Turn on the stage rotation
- Turn on the RF power and run it for 1 min at 50W then ramp it to 70W, when about a minute is left to the deposition slowly ramp the power to 50W

- The deposition rate for Si_3N_4 is 17nm/min
- The deposition rate for SiO_2 is 15nm/min
- When the deposition is completed, turn off the RF power and close the gas valves
- Turn off the stage rotation
- Turn off the heater, the heater control, and the RF control panel
- Allow the chamber to cool to at least 100C or lower
- Repeat the purge cycle 3 times
- Open the nitrogen valve
- Close the vacuum valve and wait for chamber to vent
- Open chamber and remove sample
- Wipe down chamber, close lid and open vacuum valve again

SU-8

- SU-8 is a polymer and a negative tone photoresist that is used for permanent structures
- SU-8 is sometimes applied in the final step of device fabrication to coat the sample sidewalls and create a passivation or encapsulation layer
- Similar materials such as polyimide have been used as an encapsulation material as well

A.4.1 SU-8 Procedure

- Set one hot plat at 65C and another to 95C ahead of time
- Clean sample using previously described cleaning methods
- Treat sample surface using either the HCl or H_3PO_4 recipes, or some other method, described earlier
- Thoroughly rinse sample
- Spin coat sample at 4000 rpm for 30sec with SU-8 using one of the available varieties
  - 2007
  - 2002
  - 2000.5, recommended
- Bake at 65C for one minute and then at 95C for one minute
- Note that this two step process is recommended but I have used just 90C for 2 minutes and the results were satisfactory
- Align and expose CI2 (405nm) for 2.5sec
- Post exposure bake, repeat the pre-exposure bake
- Use non-diluted SU-8 developer
  - Note that the SU-8 developer is re-usable and is not a standard developer stocked in the cleanroom; so save it after you use it. There should be a container of used SU-8 developer sitting on the self in the developer bench, just dip the sample in it and replace the lid when you are done.

A.5 Metal evaporation

Electron beam evaporation

- Metal evaporation is generally used to create electrical contacts on devices
- The typical recipe we use for ohmic contacts for the superlattice detectors is $500\mathring{A}$ of Titanium (Ti) followed by $500\mathring{A}$ of Platinum (Pt) and finally $3000\mathring{A}$ of Gold (Au)
- Ti makes a good electrical and adhesive contact, Pt serves a diffusion barrier to block Au atoms from intermixing with the device, and the Au layer is for making electrical contact with external bonding techniques
- However, many other recipes/combinations exist that are regularly used
  - The QDIP group uses a form of Ge/Au/Ni/Au for GaAs based devices
  - For under bump metalization (UBM) use Ti/Ni/Au ($500\mathring{A}/2000\mathring{A}/500\mathring{A}$)

Electron beam evaporation procedure

- Samples must first be patterned (usually with an image reversal photoresist)
- Next it is recommended that they are dipped in the 1:10 $HCl : H_2O$ solution for 30sec to remove any oxides on the surface
- Log in to the metal evaporator TIP account
- Turn off ion gauge
- The vacuum process is currently set to automatic
  - Switch the vacuum system to standby and wait for Cryo valve to close, you can check this by looking at the valve behind in the chamber

  - Switch the system to vent and wait for door to open, this will take approximately 6 minutes

Thermal evaporation

- Thermal evaporation is generally used in our group for evaporating thick ($\sim 3\mu m$) layers of indium for indium bumps required for hybridization
- Another commonly thermally evaporated metal is aluminum
- The primary difference between thermal and electron beam evaporation is that the means in which the material being evaporated is heated
- In thermal evaporation, the source metal is placed in a tungsten boat or container with wings on either end that get clamped to the electrodes in the vacuum chamber
- electrical current is driven through the electrodes and consequently the boat with the metal heats up when a sufficient amount of current is applied

A.6 Abbreviated Single Pixel Detector Fabrication Procedure

- Clean sample surface
- Pattern using positive tone resist photolithography for mesa etching
- Etch pattern using ICP BCl_3 recipe
- Clean sample again
- Coat with encapsulation method of choice

- If Si_3N_4 or SiO_2 was used, etch with RIE using the CF_4 recipe

- Pattern using image reversal resist photolithography for metal evaporation

- Perform diluted HCl dip to prep sample surface

- Deposit contact metal and perform liftoff

- Sample is complete and ready for testing

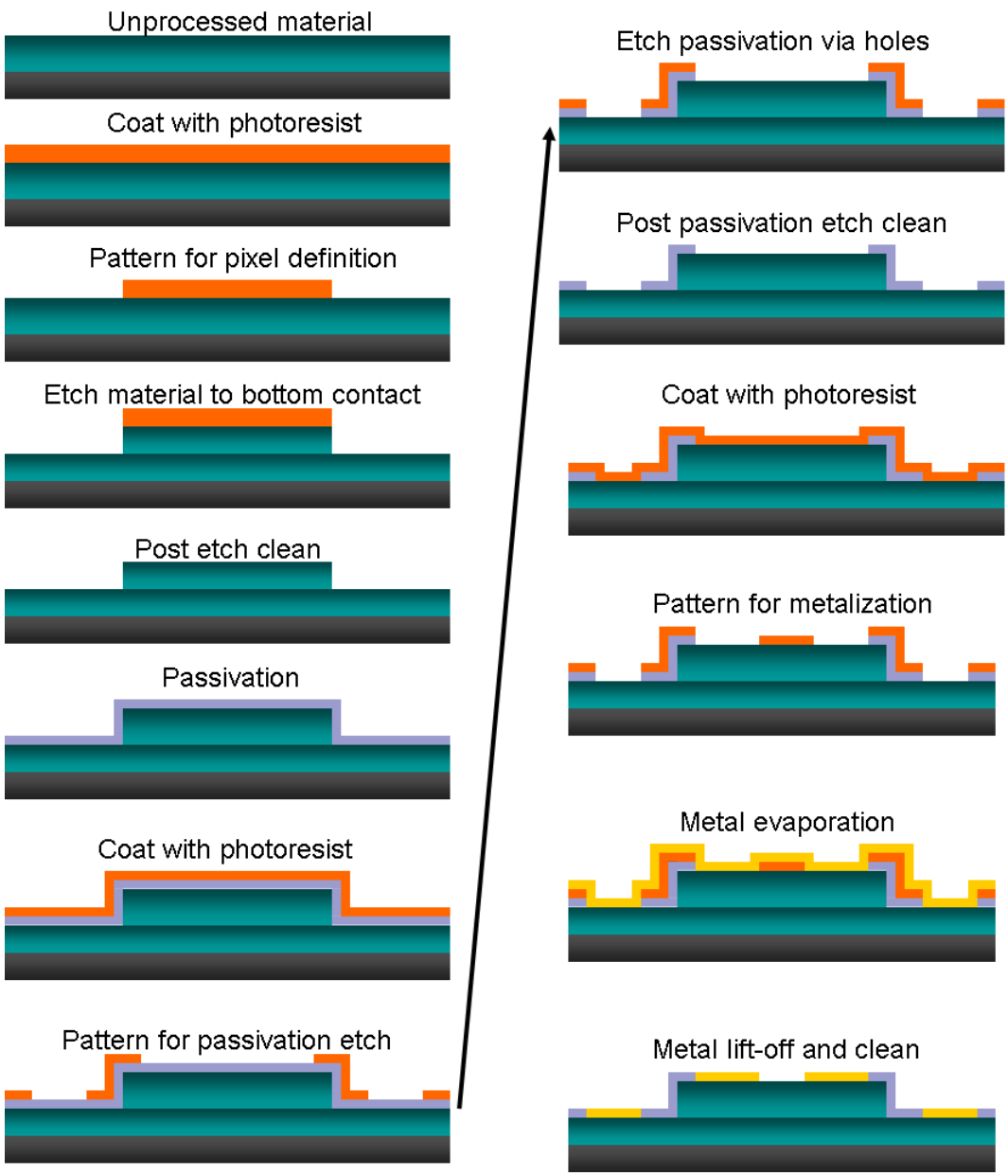

Figure A.1: Single pixel detailed processing recipe

A.7 Abbreviated Focal Plane Array Fabrication Procedure

The simplified steps for fabricating a focal plane array is illustrated in figure A.2.

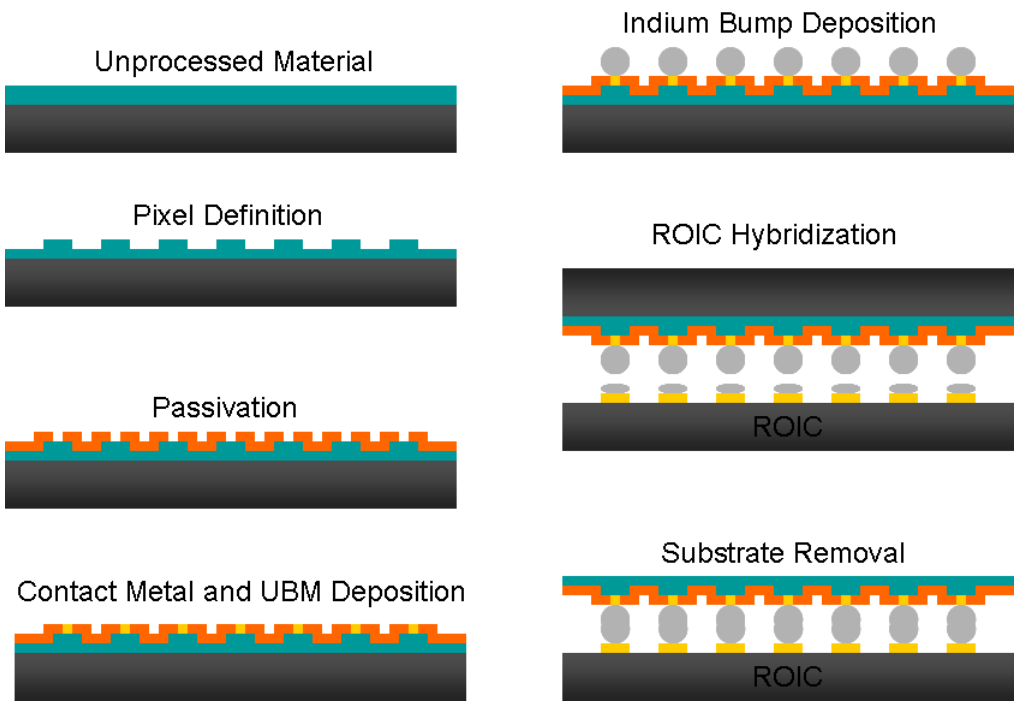

Figure A.2: Focal Plane Array processing recipe diagram

References

[1] Buzug, T. M., Schumann, S., Pfaffmann, L., Reinhold, U., and Ruhlmann, J. In *Conf. Proc. IEEE Eng. Med. Biol. Soc.*, (2006).

[2] Rogalski, A. *Progress in Quantum Electronics* **36**(23), 342 – 473 (2012).

[3] Rogalski, A. *Progress in Quantum Electronics* **27**(23), 59 – 210 (2003).

[4] Tennant, W. E. *Journal of Electronic Materials* **39**(7), 1030–1035 (2010).

[5] Kroemer, H. *Physica E: Low-dimensional Systems and Nanostructures* **20**(3-4), 196–203 (2004).

[6] Maimon, S. and Wicks, G. W. *Applied Physics Letters* **89**(15), 151109 (2006).

[7] Klipstein, P., Klin, O., Grossman, S., Snapi, N., Lukomsky, I., Yassen, M., Aronov, D., Berkowitz, E., Glozman, A., Magen, O., Shtrichman, I., Frenkel, R., and Weiss, E. *Proceedings of SPIE* **8268**, 82680U–82680U–8 (2012).

[8] Nguyen, B. M., Bogdanov, S., Pour, S. A., and Razeghi, M. *Applied Physics Letters* **95**(18), 183502 (2009).

[9] Nguyen, B.-M., Hoffman, D., Delaunay, P.-Y., Huang, E. K.-W., Razeghi, M., and Pellegrino, J. *Applied Physics Letters* **93**(16), 163502 (2008).

[10] Gautam, N., Myers, S., Barve, A., Klein, B., Smith, E., Rhiger, D., Kim, H. S., Tian, Z.-B., and Krishna, S. *Quantum Electronics, IEEE Journal of* **49**(2), 211 –217 feb. (2013).

[11] Ting, D. Z., Hill, C. J., Soibel, A., Nguyen, J., Keo, S. A., Mumolo, J. M., Lee, M. C., Yang, B., and Gunapala, S. D. In *Proceedings of the SPIE The International Society for Optical Engineering*, volume 7419 of *Proc. SPIE - Int. Soc. Opt. Eng. (USA)*, 74190B (12 pp.). SPIE - The International Society for Optical Engineering, (2009).

[12] Myers, S. A., Khoshakhlagh, A., Mailfert, J., Wanninkhof, P., Plis, E., Kutty, M. N., Kim, H. S., Gautam, N., Klein, B., Smith, E. P. G., and Krishna, S. *SPIE proceedings* **7808**, 780805–780805–9 (2010).

[13] Hudson, R. D., J. *Infrared System Engineering*. John Wiley & Sons, Inc., New York, (1969).

[14] Vincent, J. D. *Fundamentals of Infrared Detector Operation and Testing*. John Wiley & Sons, Inc., New York, 1st edition, (1990).

[15] Dereniak, E. L. and Boreman, G. D. *Infrared Detectors and Systems*. John Wiley & Sons, Inc., New York, (1996).

[16] Kim, H. S. *Investigation of InAs/GaSb superlattice based nBn detectors and focal plane arrays*. Doctoral, University of New Mexico, (2010).

[17] Gautam, N. *Unipolar Barrier Strained Layer Superlattice Infrared Photodiodes: Physics and Barrier Engineering*. Doctoral, University of New Mexico, (2012).

[18] Shenoi, R. *Multispectral Plasmon Enhanced Quantum Dots in a Well Infrared Photodetectors*. Doctoral, University of New Mexico, (2010).

[19] Barve, A. *Heterostructure engineering of quantum dots-in-a-well infrared photodetectors*. Doctoral, University of New Mexico, (2012).

[20] Soibel, A., Nguyen, J., Rafol, S. B., Liao, A., Hoeglund, L., Khoshakhlagh, A., Keo, S. A., Mumolo, J. M., Liu, J., Ting, D. Z., and Gunapala, S. D. *Proceedings of the SPIE The International Society for Optical Engineering* **8268**, 82680Y–82680Y–6 (2012).

[21] Sundaram, M., Reisinger, A., Dennis, R., Patnaude, K., Burrows, D., Bundas, J., Beech, K., and Faska, R. *Infrared Physics and Technology* **54**, 243–246 (2011).

[22] Rogalski, A. *Infrared Physics Technology* **43**(3-5), 187–210 (2002).

[23] Doak, R. S. *Galileo: astronomer and physicist*. Enslow Pub Inc., (2005).

[24] Herschel, W. *Philosophical Transactions of the Royal Society of London* **90**, 284–292 (1800).

[25] Wormser, E. M. *Applied Optics* **7**(9), 1667–1672 (1968).

[26] Langley, S. P. *American Metrological Society* (1880).

[27] Morten, F. D. and King, R. E. J. *Appl. Opt.* **4**(6), 659–663 Jun (1965).

[28] Blum, A. N., Mokrovski, N. P., and Regel, A. R. *Zh. Tekhn. Fiz.* **21**(237) (1951).

[29] Welker, H. *Z. Naturforsch* **7a**(744) (1952).

[30] Lawson, W., Nielsen, S., Putley, E., and Young, A. *Journal of Physics and Chemistry of Solids* **9**(34), 325 – 329 (1959).

[31] Long, D. and Schmit, J. L. In *Infrared Detectors,* Willardson, R. and Beer, A. C., editors, volume 5 of *Semiconductors and Semimetals*, 175 – 255. Elsevier (1970).

[32] Jones, R. C. *Nature* **170**, 937–938 (1952).

[33] Jones, R. C. *Review of Scientific Instruments* **24**(11), 1035–1040 (1953).

[34] Jones, R. *Proceedings of the IRE* **47**(9), 1495 –1502 sept. (1959).

[35] Jones, R. C. *Journal of the Optical Society of America* **50**(11), 1058 (1960).

[36] Bronzino, J. D., editor. *Medical Devices and Systems.* CRC Press, (2006).

[37] Rothstein, M. A., Alcalde, . G., Elster, N. R., Majumder, M. A., Palmer, L. I., and Stone, T. H. November (2003).

[38] *Clinical, Cosmetic and Investigational Dermatology* **5**, 195 – 212 (2012).

[39] Krishna, S., Yaesoubi, M., Barve, A., Sharma, M., Sen, P., Krishna, S., Berwick, M., and Padilla, S. Presented as the 2012 Quantum Structure Infrared Photodetector Conference, Cargese, Corsica-France, (2012).

[40] Favro, L., Thomas, R., Han, X., Ouyang, Z., Newaz, G., and Gentile, D. *International Journal of Fatigue* **23, Supplement 1**(0), 471 – 476 (2001).

[41] Parrish, W. J., Blackwell, J. D., Paulson, R. C., and Arnold, H. *Proc. SPIE* **1512**(68) (1991).

[42] Norton, P. *OptoElectronics Review* **10**(3), 159–174 (2002).

[43] Levine, B. F. *Journal of Applied Physics* **74**(8), R1 (1993).

[44] Klipstein, P., Klin, O., Grossman, S., Snapi, N., Yaakobovitz, B., Brumer, M., Lukomsky, I., Aronov, D., Yassen, M., Yofis, B., and Et Al. *Proceedings of SPIE* **7608**, 76081V (2010).

[45] Rogalski, A., Antoszewski, J., and Faraone, L. *Journal of Applied Physics* **105**(9), 091101 (2009).

[46] Krishna, S. In *IEEE Photonics Society, 2010 23rd Annual Meeting of the*, 527, nov. (2010).

[47] Tennant, W. E., Lee, D., Zandian, M., Piquette, E., and Carmody, M. *Journal of Electronic Materials* **37**(9), 1406–1410 (2008).

[48] Tennant, W. E. *Progress in Quantum Electronics* **36**, 273–292 (2012).

[49] Kalchmair, S., Detz, H., Cole, G. D., Andrews, A. M., Klang, P., Nobile, M., Gansch, R., Ostermaier, C., Schrenk, W., and Strasser, G. *Applied Physics Letters* **98**(1), 011105 (2011).

[50] Tidrow, M. Z. *Infrared Physics and Technology* **52**(6), 322 – 325 (2009). Proceedings of the International Conference on Quantum Structure Infrared Photodetectors (QSIP) 2009.

[51] Barve, A., Lee, S., Noh, S., and Krishna, S. *Laser and Photonics Reviews* **4**(6), 738–750 (2010).

[52] Esaki, L. and Tsu, R. *IBM Journal of Research and Development* **14**(1), 61 –65 jan. (1970).

[53] Sai-Halasz, G. A., Tsu, R., and Esaki, L. *Applied Physics Letters* **30**(12), 651 (1977).

[54] Smith, D. L. and Mailhiot, C. *Journal of Applied Physics* **62**(6), 2545 (1987).

[55] Smith, D. L. and Mailhiot, C. *Rev. Mod. Phys.* **62**, 173–234 Jan (1990).

[56] Youngdale, E. R., Meyer, J. R., Hoffman, C. A., Bartoli, F. J., Grein, C. H., Young, P. M., Ehrenreich, H., Miles, R. H., and Chow, D. H. *Applied Physics Letters* **64**(23), 3160–3162 (1994).

[57] Grein, C. H., Young, P. M., Ehrenreich, H., and McGill, T. C. *Journal of Electronic Materials* **22**(8), 1093–1096 AUG (1993).

[58] Mohseni, H., Wojkowski, J. S., Tahraoui, A., Razeghi, M., Brown, G. J., and Mitchel, W. C. , 153–160 (2000).

[59] Rodriguez, J., Plis, E., Lee, S., Dawson, L., and Krishna, S. In *Nanotechnology, 2006. IEEE-NANO 2006. Sixth IEEE Conference on*, volume 1, 100 – 103, june (2006).

[60] Haugan, H. J., Brown, G. J., Pacley, S. D., Grazulis, L., and Fenstermaker, S. T. *Study of strain balance in long wavelength infrared InAs/GaSb superlattice materials*, volume 7808. COPYRIGHT SPIE–The International Society for Optical Engineering. Downloading of the abstract is permitted for personal use only., (2010).

[61] Haugan, H. J., Brown, G. J., Elhamri, S., Mitchel, W. C., Mahalingam, K., Kim, M., Noe, G. T., Ogden, N. E., and Kono, J. *Applied Physics Letters* **101**(17), 171105 (2012).

[62] Haugan, H., Grazulis, L., Brown, G., Mahalingam, K., and Tomich, D. *Journal of Crystal Growth* **261**(4), 471 – 478 (2004).

[63] Gautam, N., Myers, S., Barve, A. V., Klein, B., Smith, E., Rhiger, D., Plis, E., Kutty, M. N., Henry, N., Schuler-Sandy, T., and Krishna, S. *Infrared Physics and Technology* (0), – (2012).

[64] Gautam, N., Myers, S., Barve, A. V., Klein, B., Smith, E. P., Rhiger, D. R., Dawson, L. R., and Krishna, S. *Applied Physics Letters* **101**(2), 021106 (2012).

[65] Schuler-Sandy, T., Myers, S., Klein, B., Gautam, N., Ahirwar, P., Tian, Z.-B., Rotter, T., Balakrishnan, G., Plis, E., and Krishna, S. *Applied Physics Letters* **101**(7), 071111 (2012).

[66] Plis, E., Myers, S., Kutty, M. N., Mailfert, J., Smith, E. P., Johnson, S., and Krishna, S. *Applied Physics Letters* **97**(12), 123503 (2010).

[67] Khoshakhlagh, A., Myers, S., Kim, H., Plis, E., Gautam, N., Lee, S. J., Noh, S. K., Dawson, L. R., and Krishna, S. *IEEE Journal of Quantum Electronics* **46**, 959–964 June (2010).

[68] Plis, E., Kutty, M., Myers, S., Rathi, A., Aifer, E., Vurgaftman, I., and Krishna, S. *Infrared Physics and Technology* **55**(23), 216 – 219 (2012).

[69] Kim, H. S., Plis, E., Gautam, N., Myers, S., Sharma, Y., Dawson, L. R., and Krishna, S. *Applied Physics Letters* **97**(14), 143512 (2010).

[70] Plis, E., Kutty, M., Myers, S., Kim, H., Gautam, N., Dawson, L., and Krishna, S. *Infrared Physics and Technology* **54**(3), 252 – 257 (2011). ¡ce:title¿Proceedings of the International Conference on Quantum Structure Infrared Photodetector (QSIP) 2010¡/ce:title¿.

[71] Gautam, N., Kim, H. S., Kutty, M. N., Plis, E., Dawson, L. R., and Krishna, S. *Applied Physics Letters* **96**(23), 231107 (2010).

[72] Bandara, S., Maloney, P., Baril, N., Pellegrino, J., and Tidrow, M. *Optical Engineering* **50**(6), 061015–061015–5 (2011).

[73] Steenbergen, E. H., Connelly, B. C., Metcalfe, G. D., Shen, H., Wraback, M., Lubyshev, D., Qiu, Y., Fastenau, J. M., Liu, A. W. K., Elhamri, S., Cellek, O. O., and Zhang, Y. H. *Applied Physics Letters* **99**(25), 251110 (2011).

[74] Razeghi, M. and Nguyen, B.-M. *Physics Procedia* **3**(2), 1207–1212 (2010).

[75] Soibel, A., Ting, D. Z. Y., Hill, C. J., Lee, M., Nguyen, J., Keo, S. A., Mumolo, J. M., and Gunapala, S. D. *Applied Physics Letters* **96**(11), 111102 (2010).

[76] Nguyen, B.-M., Abdollahi Pour, S., Bogdanov, S., and Razeghi, M. , 760825–760825–9 (2010).

[77] White, A. M. (1987).

[78] Itsuno, A. M., Phillips, J. D., and Velicu, S. *Applied Physics Letters* **100**(16), 161102 (2012).

[79] Destfanis, G. *Journal of Crystal Growth* **86**(14), 700 – 722 (1990).

[80] Piquette, E., Edwall, D., Lee, D., and Arias, J. *Journal of Electronic Materials* **35**, 1346–1349 (2006).

[81] Pedrazzani, J., Maimon, S., and Wicks, G. *Electronics Letters* **44**(25), 1487 –1488 4 (2008).

[82] Klipstein, P. *Proceedings of SPIE* **6940**, 69402U–69402U–12 (2008).

[83] Klipstein, P., Klin, O., Grossman, S., Snapi, N., Lukomsky, I., Brumer, M., Yassen, M., Aronov, D., Berkowitz, E., Glozman, A., Fishman, T., Magen, O., Shtrichman, I., and Weiss, E. *Proceedings of SPIE* **8012**, 80122R–80122R–9 (2011).

[84] Klipstein, P., Klin, O., Grossman, S., Snapi, N., Lukomsky, I., Aronov, D., Yassen, M., Glozman, A., Fishman, T., Berkowicz, E., Magen, O., Shtrichman, I., and Weiss, E. *Optical Engineering* **50**(6), 061002–061002–10 (2011).

[85] Klipstein, P., Klin, O., Grossman, S., Snapi, N., Yaakobovitz, B., Brumer, M., Lukomsky, I., Aronov, D., Yassen, M., Yofis, B., Glozman, A., Fishman, T., Berkowitz, E., Magen, O., Shtrichman, I., and Weiss, E. *Proceedings of SPIE* **7660**, 76602Y–76602Y–9 (2010).

[86] Klem, J. F., Kim, J. K., Cich, M. J., Hawkins, S. D., Fortune, T. R., and Rienstra, J. L. , 76081P–76081P–12 (2010).

[87] Rodriguez, J. B., Plis, E., Bishop, G., Sharma, Y. D., Kim, H., Dawson, L. R., and Krishna, S. *Applied Physics Letters* **91**, 043514–1,043514–2 (2007).

[88] Umana-Membreno, G. A., Klein, B., Kala, H., Antoszewski, J., Gautam, G., Kutty, M. N., Plis, E., Dell, J. M., Krishna, S., and Faraone, L. In *Proceedings of SPIE,* Andresen, B. F., Fulop, G. F., and Norton, P. R., editors, volume 8012, 80120Y–80120Y–6. SPIE, (2011).

[89] Nguyen, B.-M., Chen, G., Hoang, A. M., Pour, S. A., Bogdanov, S., and Razeghi, M. *Applied Physics Letters* **99**(3), 033501 (2011).

[90] Plis, E., Krishna, S., Gautam, N., Myers, S., and Krishna, S. *Photonics Journal, IEEE* **3**(2), 234–240 (2011).

[91] Ting, D. Z. Y., Hill, C. J., Soibel, A., Keo, S. A., Mumolo, J. M., Nguyen, J., and Gunapala, S. D. *Applied Physics Letters* **95**(2), 023508 (2009).

[92] Aifer, E. H., Tischler, J. G., Warner, J. H., Vurgaftman, I., Bewley, W. W., Meyer, J. R., Kim, J. C., Whitman, L. J., Canedy, C. L., and Jackson, E. M. *Applied Physics Letters* **89**(5), 053519 (2006).

[93] Salihoglu, O., Muti, A., Kutluer, K., Tansel, T., Turan, R., Ergun, Y., and Aydinli, A. *Applied Physics Letters2* **101**, 073505 (2012).

[94] Kim, H. S., Cellek, O. O., Lin, Z.-Y., He, Z.-Y., Zhao, X.-H., Liu, S., Li, H., and Zhang, Y.-H. *Applied Physics Letters* **101**(16), 161114 (2012).

[95] Olson, B. V., Shaner, E. A., Kim, J. K., Klem, J. F., Hawkins, S. D., Murray, L. M., Prineas, J. P., Flatté, M. E., and Boggess, T. F. *Applied Physics Letters* **101**(9), 092109 (2012).

[96] Donetsky, D., Belenky, G., Svensson, S., and Suchalkin, S. *Applied Physics Letters* **97**(5), 052108 (2010).

[97] Plis, E. A., Kutty, M. N., and Krishna, S. *Laser and Photonics Reviews* **7**(1), 45–59 (2013).

[98] Hood, A., Razeghi, M., Aifer, E. H., and Brown, G. J. *Applied Physics Letters* **87**(15), 151113 (2005).

[99] Gin, A., Wei, Y., Hood, A., Bajowala, A., Yazdanpanah, V., Razeghi, M., and Tidrow, M. *Applied Physics Letters* **84**(12), 2037–2039 (2004).

[100] Hoffmann, J., Lehnert, T., Hoffmann, D., and Fouckhardt, H. *Semiconductor Science and Technology* **24**(6), 065008 (2009).

[101] Kim, H. S., Plis, E., Khoshakhlagh, A., Myers, S., Gautam, N., Sharma, Y. D., Dawson, L. R., Krishna, S., Lee, S. J., and Noh, S. K. *Applied Physics Letters* **96**(3), 033502 (2010).

[102] Hood, A., Delaunay, P.-Y., Hoffman, D., Nguyen, B.-M., Wei, Y., Razeghi, M., and Nathan, V. *Applied Physics Letters* **90**(23), 233513 (2007).

[103] Yang, Q., Pfahler, C., Schmitz, J., Pletschen, W., and Fuchs, F. *SPIE Proceedings, Quantum Sensing: Evolution and Revolution from Past to Future* **4999**, 448–456 (2003).

[104] Chih-Tang, S., Noyce, R. N., and Shockley, W. *Proceedings of the IRE* **45**, 1228–1243 (1957).

[105] Lott, J. A., Dawson, L. R., Jones, E. D., and Klem, J. F. *Applied Physics Letters* **56**(13), 1242–1244 (1990).

[106] Adachi, S. *Journal of Applied Physics* **58**(3), R1–R29 (1985).

[107] Vurgaftman, I., Meyer, J. R., and Ram-Mohan, L. R. *Journal of Applied Physics* **89**(11), 5815–5875 (2001).

[108] Moss, T. S. *Proceedings of the Physical Society. Section B* **67**(10) (1954).

[109] Rakovska, A., Berger, V., Marcadet, X., Glastre, G., and Vinter, B. , 537–546 (2000).

[110] Hoffman, D., Nguyen, B.-M., Delaunay, P.-Y., Hood, A., Razeghi, M., and Pellegrino, J. *Applied Physics Letters* **91**(14), 143507 (2007).

[111] Plis, E., Annamalai, S., Posani, K. T., Krishna, S., Rupani, R. A., and Ghosh, S. *Journal of Applied Physics* **100**(1), 014510 (2006).

[112] Tilton, M. L. *Journal of Applied Physics* **86**(3), 1420–1429 (1999).

[113] Baril, N., Billman, C., Maloney, P., Nallon, E., Tidrow, M., Pellegrino, J., and Bandara, S. *Applied Physics Letters* **102**(1), 013509 (2013).

[114] Christol, P., Konczewicz, L., Cuminal, Y., At-Kaci, H., Rodriguez, J. B., and Joulli, A. *physica status solidi (c)* **4**(4), 1494–1498 (2007).

[115] Khoshakhlagh, A., Jaeckel, F., Hains, C., Rodriguez, J. B., Dawson, L. R., Malloy, K., and Krishna, S. *Applied Physics Letters* **97**(5), 051109 (2010).

[116] Guo, X., Ma, W., Huang, J., Zhang, Y., Wei, Y., Cui, K., Cao, Y., and Li, Q. *Semiconductor Science and Technology* **28**(4), 045004 (2013).

[117] Nguyen, B.-M., Hoffman, D., wei Huang, E. K., Delaunay, P.-Y., and Razeghi, M. *Applied Physics Letters* **93**(12), 123502 (2008).

[118] Bhattacharya, P. *Semicondunctor Optoelectronic Devices*. Prentice Hall, (1996).

[119] Liu, J.-m. *Photonic Devices*, volume 33. Cambridge University Press, (2005).

[120] Bhattacharya, P. and Su, X. H. *Quantum dot infrared detectors*, volume 11. Springer US, (2006).